THESE

Présentée par
NGUYỄN Hoàng Hải

le 21 mars 2003
pour obtenir le titre de

DOCTEUR DE L'UNIVERSITE JOSEPH FOURIER–GRENOBLE 1

(Discipline : Physique)

Nanomatériaux magnétiques élaborés par déformation mécanique

Composition du Jury :

Rapporteurs :	E. Brück
	V. Pierron-Bohnes
Examinateurs :	O. Isnard
	N.P. Thùy
Directeurs de thèse :	D. Givord
	N. M. Dempsey

Thèse préparée au Laboratoire Louis Néel
Centre National de la Recherche Scientifique (CNRS) – Grenoble

Nanomagnetic Materials Prepared by Mechanical Deformation

Chế tạo vật liệu từ nano bằng phương pháp biến dạng cơ học

Acknowledgements

This thesis has been realized with input from numerous friends and colleagues. Firstly I would like to thank thesis advisors Dr. Dominique Givord and Dr. Nora Dempsey at Laboratoire Louis Néel (LLN), CNRS Grenoble, who inspired me to the exciting field of magnetism and shared with me their magnetic experiences and many interesting discussions to develop this thesis. I am also deeply indebted to my fellow student Alexandre Giguègre, who helped me a lot at the beginning of the work.

I am grateful to the examiners Prof. Ekkes Brück of University of Amsterdam and Dr. Veronique Pierron-Bohnes of IPCMS-GEMM CNRS-ULP, CNRS Strasbourg, and members of the jury Prof. Olivier Isnard of Université Joseph Fourier and Prof. Nguyen Phu Thuy of Vietnam National University, Hanoi (VNU).

Very special thanks go sincerely to Prof. Nguyen Hoang Luong at VNU who strongly supported me to be in LLN and encouraged me in the last years.

I would like to thank many colleagues at LLN for their continuous helping during 3 years. Especially, I would like to express my thanks to Dr. Laurent Ranno for many general discussions and also for his friendship. Many thanks are extended to Dr. Olivier Fruchart for his suggestions for the calculations in chapter 3. Special thanks are given to fellow students Clarisse Ducruet and Florent Ingwiller for their nice cooperation, to the director of LLN Dr. Claudine Lacroix and secretarial board: Véronique Fauvel and Sabine Domingues, to the technical team: Didier Dufeu, Eric Eyraud, Laurent Del Rey for their help on many occasions.

I would like to express my sincere thanks to Dr. Oliver Gutfleisch and Kirill Khlopkov of IMW Dresden for the SEM images and cooperation. Special thanks are given to Dr. M. Véron and Dr. M. Verdier at LTPCM-INPG for the TEM images and micro hardness measurements.

I am indebted to Dr. Jacque Marcus of LEPES, CNRS – Grenoble for his experimental help. Many thanks are given to colleagues at CRTBT, CNRS – Grenoble for the permission to use their rolling machine for sample preparation.

I would like to thank my Vietnamese colleagues at VNU for their help in many ways: Prof. Nguyen Chau, Prof. Nguyen Huu Duc, Prof. Luu Tuan Tai.

I gratefully acknowledge financial support of the European project on high temperature magnets HITEMAG and the CNRS PICS programme "Nanomateriaux" and the French Embassy in Vietnam.

Lastly, I would like to thank my parents, my parents in law, my wife Do Thi Ngoc Bich, my son Nguyen Hai Toan for their understanding and support of my study in the past years.

Contents

Introduction en Français

L'étude des matériaux nanophasés ou nanostructurés constitue une nouvelle branche de la Science des Matériaux. De nouvelles propriétés émergent dans ces systèmes, du fait que leurs dimensions sont inférieures aux portées caractéristiques des interactions magnétiques. Ces propriétés peuvent être exploitées pour produire des matériaux magnétiques doux [1], des aimants permanents [2] ou des matériaux pour l'enregistrement magnétique [3]. En particulier, dans les matériaux magnétiques doux à base de fer, les moments magnétiques sont couplés sur des distances bien supérieures au diamètre des grains constitutifs. L'anisotropie effective, qui résulte d'une moyenne sur l'ensemble de ces grains orientés de façon aléatoire, est de plusieurs ordres de grandeur inférieure à l'anisotropie magnétocristalline de chaque grain [4]. Des propriétés magnétiques ultra-douces en résultent. Dans les nanomatériaux de type Nd-Fe-B ou Sm-Co, en raison de la très forte anisotropie magnétocristalline des grains constitutifs, l'alignement commun des moments entre grains est restreint aux atomes situés au voisinage de la surface des grains, conduisant au phénomène dit de renforcement de rémanence [5]. Dans les nanocomposites doux/durs, le renversement de la phase douce est empêché par le couplage d'échange avec les grains durs. Le fait que la taille des grains doux soit bien inférieure à la dimension d'équilibre des parois de domaines s'ajoute à ceci et entraîne des comportements dits de « spring-magnet » [6, 7].

Les types variés de nanomatériaux décrits ci-dessus sont préparés en général par trempe rapide sur roue à partir du liquide, ou par une technique similaire. De telles techniques permettent de produire de grandes quantités de matériaux à l'échelle industrielle. Elles n'offrent pas un contrôle aisé de la composition des alliages ni de leur nanostructure. Les techniques de déformation mécanique qui ont été développées à l'origine pour réduire les dimensions macroscopiques de matériaux, peuvent constituer une voie alternative d'élaboration de nanomatériaux. Elles présentent plusieurs avantages tels que le faible coût

des équipements, leur simplicité d'opération et la manipulation aisée des matériaux [8]. Au laboratoire Louis Néel, ces techniques ont été utilisées pour préparer des nanomatériaux par co-déformation d'éléments métalliques sous forme de fils ou plaques. Des réseaux de nanofils de fer dans une matrice de cuivre ont été tout d'abord préparés par extrusion [9]. Dans une seconde étape, l'utilisation de billettes sacrificielles en aluminium, a permis d'extruder des nanomatériaux sous forme de plaquettes, sans dilution progressive au sein de la matrice. Cependant, les efforts pour réduire la taille des éléments constitutifs en dessous de 0.1 μm environ ont été infructueux. Dans son travail de thèse, A. Giguère a alors combiné extrusion et laminage pour préparer des multicouches de Fe/Cu, Fe/Ag and FeNi/Ag. Il a obtenu des magnétorésistances significatives et a réussi à les mesurer en configuration CPP (Current Perpendicular to Plane) [10].

Dans ces études, les éléments métalliques en jeu étaient immiscibles. A chaque étape de déformation, les matériaux deviennent plus durs mécaniquement. Des traitements thermiques de revenu sont requis aux étapes intermédiaires. Les températures de revenu sont suffisamment basses afin que la structure interne (en réseau de fils ou multicouches) ne soit pas détruite. La nanostructure finale des matériaux est intermédiaire entre celles de multicouches élaborés par EJM (épitaxie par jet moléculaire) ou par pulvérisation cathodique et celles de matériaux élaborés par trempe rapide.

L'objectif de cette thèse était d'explorer la possibilité de préparer des nanomatériaux magnétiques par déformation de feuilles de métaux miscibles, d'épaisseurs initiales inférieures au millimètre, sans aucun traitement thermique jusqu'à l'échelle nanométrique, et de n'appliquer qu'à ce stade le traitement de diffusion-réaction entre les éléments constitutifs, requis pour la formation des phases recherchées. Nous avons choisi le système Fe/Pt, avec pour premier objectif l'obtention de la phase équiatomique dure FePt $L1_0$. Il est bien connu que les aimants permanents de haute performance doivent associer une haute aimantation rémanente et une forte coercitivité et que de telles propriétés peuvent dépendre de façon critique de la nanostructure du matériau concerné. Nous avons décidé aussi d'explorer la possibilité de déformer des matériaux associant des éléments de terres rares et de transition et nous nous sommes plus spécialement intéressés au système Sm/Fe auquel A. Giguère avait consacré des travaux préliminaires dans le cadre de sa thèse.

Ce manuscrit est constitué de 5 chapitre. Le chapitre 1 illustre quelques propriétés générales des matériaux nanostructurés. La déformation mécanique est décrite ainsi que des techniques

variées de déformation mécanique, plus particulièrement l'extrusion et le laminage sous gaine. Le procédé que nous avons développé pour la préparation de séries de systèmes Fe/Pt nanostructurés est décrit de façon détaillée. Ces systèmes sont FePt, FePt/Ag (l'introduction d'Ag avait pour but d'augmenter la coercitivité), Fe/Pt riche en fer (le but ici était de produire des matériaux nanocomposites durs/doux $FePt/Fe_3Pt$) et FePt riche en Pt (pour obtenir un mécanisme de type décalage d'échange (exchange-bias) entre FePt et $FePt_3$). Les propriétés structurales et les propriétés magnétiques de ces systèmes variés sont discutées au chapitre 2. Le chapitre 3 n'est pas directement lié aux résultats présentés dans ce travail. Je discute l'influence d'un couplage d'échange à travers l'interface sur les propriétés magnétiques intrinsèques de systèmes nanostructurés hétérogènes. Au chapitre 4, je discute le renversement d'aimantation dans FePt et $FePt/Fe_3Pt$. Je considère les effets des interactions dipolaires sur les propriétés magnétiques de systèmes hétérogènes. Au chapitre 5, je décris la préparation de barreaux magnétostrictifs $SmFe_2$ par co-extrusion de Sm et Fe jusqu'à l'échelle miconique, suivie d'un traitement de recuit à basse température (550°C).

Introduction in English

The study of nanophase and nanostructured materials constitutes a new branch of materials research. New magnetic properties emerge in these systems, because their dimensions are below the characteristic length-scales of magnetic interactions. These may be exploited to produce soft magnetic materials [1], permanent magnets [2], magnetic recording materials [3]. In particular, in Fe-based soft magnetic nanomaterials, the magnetic moments are coupled over distances much larger than the grain diameter. The effective anisotropy, determined by averaging over the randomly-oriented individual particles, is orders of magnitude smaller than the individual grain magnetocrystalline anisotropy [4]. It results that ultra-soft magnetic properties occur. In Nd-Fe-B or Sm-Co nanomaterials, due to the large magnetocrystalline anisotropy of the constitutive grains, the coupling between moments does not extend significantly beyond the grain boundary. Common alignment of the moments in different grains is restricted to the grain surface, leading to the so-called phenomenon of remanence enhancement [5]. In hard/soft nanocomposites, reversal of the soft phase is impeded by exchange coupling with the hard grains. This, combined with the fact that in the soft phase, the grain size is much smaller than the domain wall equilibrium dimensions, leads to the so-called spring-magnet properties [6, 7].

The various types of nanomaterials described above are usually prepared by fast quenching from the melt, using melt-spinning or a similar technique. These techniques allow large quantities of materials to be industrially produced. They do not offer easy control of the alloy composition nor of the alloy nanostructure. Deformation techniques which were originally developed to reduce the macroscopic dimensions of materials can be an alternative route for the preparation of nanomagnetic materials. They present numerous advantages such as low-cost and simple operation of the equipment as well as easy handling of the materials [8]. At Laboratoire Louis Néel, these techniques have been developed to prepare nanomaterials by

cyclic co-deformation of metallic elements in the shape of wires or foils. Arrays of Fe nanowires in a Cu matrix were originally prepared by extrusion [9]. In a second stage, the use of sacrificial aluminium billets allowed materials to be extruded in the shape of platelets, without progressive dilution within the matrix. However, attempts to reduce the size of the constitutive elements below typically 0.1 μm were unsuccessful. In his thesis work, A. Giguère then combined extrusion and rolling to prepare Fe/Cu, Fe/Ag and FeNi/Ag multilayers, he obtained significant GMR signals and was able to directly measure the GMR in the CPP configuration [10].

In these previous studies, the metallic elements involved were immiscible. As the deformation proceeded, the material became progressively harder. Stress-relief heat treatments had to be applied at intermediate stages. The annealing temperatures were low enough so that the internal structure (arrays of wires, multilayer) was not destroyed. The final nanostructure of the materials obtained was intermediate between those of MBE-grown or sputtered multilayers and those of melt-spun materials.

The aim of this thesis was to explore the possibility to prepare magnetic nanomaterials by deforming sub-millimetre thick foils of miscible metals down to the nanometre scale, without applying any heat treatment, and then to produce a given intermetallic phase by applying a final heat treatment of diffusion/reaction between the constitutive elements. We choose the Fe/Pt system, with the main objective of obtaining the hard $L1_0$ FePt equiatomic phase. Indeed, it is well known that high performance permanent magnets require both high remanent magnetisation and high coercive field and that both these properties are strongly dependent on the detailed nanostructure of the concerned material. We decided as well to explore the possibility of deforming systems associating rare-earth and transition metal elements and we focussed on the Sm/Fe system on which preliminary work had been realized by A. Giguère in the framework of his thesis work.

This manuscript consists of five chapters. Chapter 1 outlines some general properties of nanostructured materials. It describes deformation mechanisms and various techniques to produce mechanical deformation. Details of the extrusion and sheath-rolling techniques are in particular presented. The detailed preparation procedure of a series of Fe/Pt nanostructured systems is described. These are: FePt, FePt/Ag (Ag was introduced with the aim of improving coercivity), Fe-rich FePt (with the aim of producing exchange-coupled hard/soft FePt/Fe_3Pt), and Pt-rich FePt (with the aim of producing exchange-bias FePt/$FePt_3$). The structural

properties and the magnetic properties of these various systems are discussed in chapter 2. Chapter 3 is not directly associated with the experimental results presented in this work. It discusses the influence on the intrinsic magnetic properties of exchange-coupling across interfaces in nanostructured heterogeneous systems. Magnetisation reversal in hard FePt and $FePt/Fe_3Pt$ is discussed in chapter 4. In this chapter, we consider the effects of dipolar interactions on the magnetic properties of a heterogeneous system and we discuss the results in the framework of a dipolar-spring concept. In chapter 5, the preparation of magnetostrictive $SmFe_2$ rods by co-extrusion of Sm and Fe down to the micrometer scale followed by low-temperature annealing (550°C) is presented.

References

1. Yoshizawa, Y., S. Oguma, and K. Yamauchi, *New Fe-based soft magnetic alloys composed of ultrafine grain structure.* J. Appl. Phys., **64** (1988) 6044.
2. Hadjipanayis, G.C., *Nanophase Hard Magnets.* J. Magn. Magn. Mater., **200** (1999) 373.
3. Baibich, M.N., J.M. Broto, A. Fert, F. Nguyen Van Dau, F. Petroff, P. Etienne, G. Creuzet, A. Friederich, and J. Chazelas, *Giant Magnetoresistance of (001)Fe/(001)Cr Magnetic Superlattices.* Phys. Rev. Lett., **61** (1988) 2472.
4. Herzer, G., Scripta Metal. Mater., **33** (1995) 1741.
5. McCallum, R.W., A.M. Kadin, G.B. Clemente, and J.E. Keem, *High performance isotropic permanent magnet based on Nd-Fe-B.* J. Appl. Phys., **61** (1987) 3577.
6. Coehoorn, R., D.B. de Mooij, and C. de Waard, *Meltspun Permanent Magnet Materials Containing Fe_3B as the Main Phase.* J. Magn. Magn. Mater., **80** (1989) 101.
7. Kneller, E.F. and R. Hawig, The exchange-spring magnet: a new material principle for permanent magnets. IEEE Trans. Magn., **27** (1991) 3588.
8. Levi, F.P., Nature, **183** (1959) 1251.
9. Wacquant, F., *Elaboration et étude des propriétés de réseaux de fils magnétiques submicroniques, obtenus par multi-extrusions*, Thesis in *Physics* (2000), Université Joseph Fourier - Grenoble 1: Grenoble; Wacquant F., S. Denolly, A. Giguère, J.P. Nozières, D. Givord and V. Mazauric, *Magnetic properties of nanometric Fe wires obtained by multiple extrusions.* IEEE Trans. Magn. 35 (1999) 3484.
10. Giguère, A., Préparation et étude des propriétés magnétiques et de transport de nanomatériaux obtenus par extrusion hydrostatique et laminage, Thesis in Physics (2002), Université Joseph Fourier - Grenoble 1: Grenoble; A. Giguère, N.H. Hai, N.M. Dempsey and D. Givord, J. Magn. Mag. Mater. **242-245** (2002) 581; Giguère A., N.M. Dempsey, M. Verdier, L. Ortega and D.Givord, Giant Magnetoresistance in Bulk Metallic Multilayers Prepared by Cold Deformation. IEEE Trans. Magn. **38** (5) (2002) 2761.

Chapter 1: Mechanical Deformation - A route to the Preparation of Nanostructured Magnetic Materials

Résumé en Français

Chapitre 1: Déformation mécanique, une voie vers la préparation de matériaux nanostructurés

Dans les matériaux usuels, la taille des grains constitutifs est typiquement comprise entre quelques microns et quelques millimètres. Dans les matériaux nanostructurés, les grains contiennent quelques milliers d'atomes et sont de taille nanométrique.

Les propriétés des matériaux nanostructurés diffèrent de celles des matériaux constitués de grains de taille supérieure. Trois raisons fondamentales expliquent ces différences : - la contribution des atomes de surface a une importance relative plus importante – des phénomènes quantiques se révèlent qui résultent du confinement spatial associé aux petites dimensions et – le nombre non infini d'atomes constitutifs des objets se manifeste lorsque l'on considère les propriétés statistiques des systèmes. En magnétisme, nous pouvons citer une série de propriétés particulières telles que : - anisotropie de surface – couplage d'échange entre objets – processus d'aimantation particuliers, tels que ceux de type « exchange-spring » ou décalage d'échange.

Plusieurs procédés ont été développés pour la préparation de matériaux nanostructurés, qui peuvent se répartir en deux grande familles. Les procédés dits de type bottom-up consistent à faire croître progressivement la taille des objets, par dépôt physique ou chimique, ou précipitation au sein d'un milieu. Elle a l'avantage de permettre en général l'obtention de matériau de grandes qualités. Les procédés dits de type top-down consistent à l'opposé à réduire la taille d'objets macrocopiques par des techniques telles que la trempe rapide ou le broyage. Elles permettent de préparer de grandes quantités de matériaux, mais au prix d'une certaine perte de contrôle de la nanostructure.

Diverses méthodes de déformation mécanique de matériaux existent, qui ont déjà été utilisée en vue de préparer des matériaux nanostructurés. Ces techniques sont essentiellement le laminage, l'étirage et l'extrusion. Elles utilisent les propriétés de déformation des matériaux dans le régime de déformation plastique qui met en jeu le phénomène fondamental de

formation et de glissement de dislocations. Du fait de la formation des dislocations, un phénomène se manifeste qui fixe une limite aux déformations ultimes que l'on peut atteindre: le durcissement.

Par chauffage à des températures appropriées, un adoucissement peut être alors obtenu, qui résulte de deux mécanismes possibles, la réorganisation des dislocations en réseau (traitement dit de revenu) et le grossissement de grains (traitement dit de recristallisation).

Les propriétés de déformation des matériaux composites se décrivent d'habitude sur la base d'une simple loi de mélange. Cependant, à l'échelle nanométrique, un durcissement supérieur à celui prévue par de telles lois se manifeste qui illustre la spécificité des propriétés à cette échelle.

Au laboratoire Louis Néel, la déformation mécanique en tant qu'outil de préparation de matériaux nanostructurés a été utilisée dans le cadre de 2 thèses réalisées avant celle-ci. L'extrusion hydrostatique a été utilisée initialement par F. Wacquant. Pour atteindre des dimensions nanométriques, des cycles de déformations successifs doivent être appliqués. Des fils nanométriques de fer dans une matrice de cuivre ont été ainsi obtenus.

A chaque étape, le matériau extrudé est inséré dans une nouvelle matrice. Il en résulte une déformation progressive du matériau. Alexandre Giguère a proposé l'utilisation de matrices sacrificielles en aluminium. Il a préparé ainsi des composites de dimensions micrométriques, mais n'a pu atteindre l'échelle nanométrique du fait du durcissement trop important atteint. En vue de simplifier le procédé de déformation, il a introduit le laminage à la place de l'extrusion et mis en évidence la simplicité bien plus grande de mise en œuvre de cette technique. Pour faciliter encore l'élaboration, il a utilisé une gaine en acier inoxydable pour confiner les échantillons et c'est à cet ensemble que le procédé de déformation est appliqué. Cette approche a permis de préparer une série d'alliages constitués d'assemblages de métaux immiscibles (Fe ou Co avec Cu) et présentant de la magnétorésistance géante.

Chapter 1: Mechanical Deformation - A route to the Preparation of Nanostructured Magnetic Materials

1.1. Nanostructured magnetic materials

1.1.1. What are nanostructured materials?

Materials are composed of grains, which in turn comprise many atoms. Conventional materials have grain sizes ranging from micrometres to several millimetres and contain several billion atoms each. *Nanostructured materials* consist of nanometre sized grains which contain a few to thousands of atoms each. There are several different types of nanostructured materials. These range from zero dimensional atom clusters to three dimensional equiaxed grain structures. Each class has at least one dimension in the nanometre range, as shown in Figure 1.1. Atom clusters and filaments are defined to have *zero modulation dimensionality* (0D) and can have any aspect ratio from 1 to ∞. Any multilayered material with layer thickness in the nanometre range is classified as *uni-dimensionally modulated* (1D). Layers in the nanometre thickness range consisting of ultrafine grains (nanometre range diameter) are *bi-dimensionally modulated* (2D). This class includes coatings, buried layers and thin films. The last class is that consisting of *tri-dimensionally modulated* (3D) microstructures or nanophase materials [1].

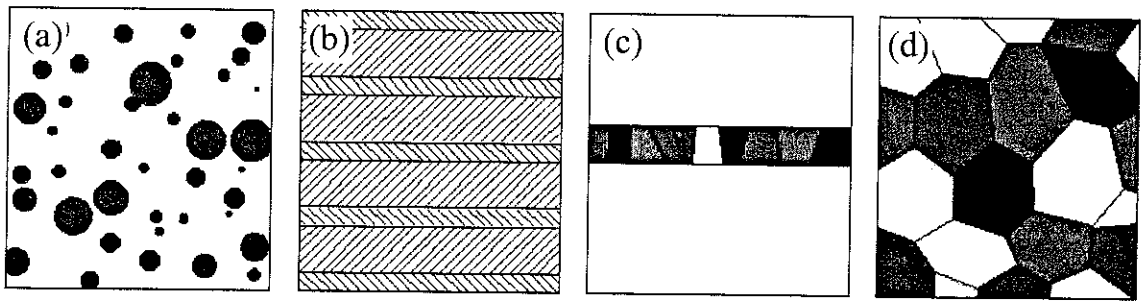

Figure 1.1: Different classes of nanostructured materials: (a) 0D, (b) 1D, (c) 2D, and (d) 3D materials [1].

Phenomena originating from nanometre sized grains have been examined in recent research on magnetic materials (so called *nanostructured magnetic materials* or *nanomagnetic materials* or *magnetic nanomaterials*).

From the composition point of view, one can classify two types of nanostructured materials: 1) nanoscale single phase materials and 2) nanoscale composites or *nanocomposites*.

1.1.2. How and Why do properties of nanomagnetic materials differ from bulk - materials?

Nanomagnetic materials are not only different in terms of dimensions. Certain magnetic properties can be modified at nanometre dimensions. Coercivity can be reduced in exchange coupled soft magnetic nanograins (FeSiB [2]), while it can be increased in decoupled hard magnetic nanograins (NdFeB) [3]. Magnetic remanence can be enhanced in systems of exchange-coupled nanograins, though this is at the expense of coercivity in the case of hard magnetic materials. Both remanence enhancement and ultra low coercivity in soft materials are due to the fact the grain dimensions in nanostructured materials are comparable to the exchange length leading to collective behaviour of an ensemble of grains. Coercivity enhancement in nanoscaled hard materials may be attributed to the isolation of magnetic defects, which act as nucleation sites for magnetisation reversal and/or the high density of grain boundaries, which act to pin domain wall motion. In addition to the enhancement of existing properties, and more importantly, new magnetic properties have been discovered in nanostructured materials – surface anisotropy, oscillatory exchange, giant magneto resistance (GMR) [4], exchange bias [5, 6], exchange spring behaviour [7]... These new properties have at least three origins. Firstly, as the *surface to volume ratio* increases, properties are increasingly dominated by surface and interface effects (a 5 nm cube of bcc Fe contains about 12000 atoms, 2000 of which are on the surface). Secondly, spatial confinement results in *new quantum phenomena* (*spin tunnelling, quantum well states...*). Finally, in many spin systems, *correlation effects* are already an important component of the bulk spin structure, spin-fluctuations [8], and spin transport [4]. Spatial confinement serves to enhance these effects. As an example, in chapter 3, we show that, in a nanomagnetic composite consisting of two different magnetic materials, due to exchange interactions across interfaces, the intrinsic magnetic properties differ from those which would be observed in the absence of exchange interactions.

1.1.3. Preparation of nanostructured materials

Essentially, there are two different approaches to produce nanostructured materials. The first approach is called the *bottom-up* approach, where individual atoms and molecules are placed or are self-assembled precisely where they are needed. Here, molecular or atomic building blocks are designed that fit together to produce nanometre grains. Plasma arcing, chemical or physical vapour deposition, electro deposition and sol-gel synthesis are bottom-up techniques. The second approach is the *top-down* approach of taking a block of material and reducing some characteristic dimensions (external dimension – particle size and/or internal dimension – grain size) to the nanometre scale. Solidification of molten metal, ball milling and forming (drawing, extrusion, rolling) techniques belong to this approach.

Each method has advantages and disadvantages depending on the desired properties or application. The main advantage of the bottom-up approach over the top-down approach is that one can have extremely good control of the sample architecture (layer thickness, layer sequence in multilayers...) and crystallography (structure, texture...) while maintaining very low contamination levels. Artificial structuring processes such as lithography and ion milling afford further control in thin films. Bottom-up approaches such as thin film processing are restricted to the production of very small quantities of material. By contrast, much greater volumes of material can be produced by top-down approaches. Though most top-down approaches (*e.g.* melt spinning, mechanical alloying) do not offer much control of the sample structure (grain shape, element proximity...) artificial structuring can be achieved using mechanical deformation processes.

1.1.4. Preparation of nanomagnetic materials by mechanical deformation

Metallurgical forming techniques (extrusion, drawing, rolling and forging) were developed to reduce one or two of the macroscopic dimensions of metals. The best-established techniques are schematised in figure 1.2. In extrusion and drawing, the sample is deformed by forcing (pushing and pulling, respectively) through a die with a bore of smaller cross section. In the most common case, samples of circular cross section are deformed through dies with circular bores, thus the sample cross sectional form is conserved. Rolling and forging lead to a change in the ratio of the sample's cross-sectional dimensions.

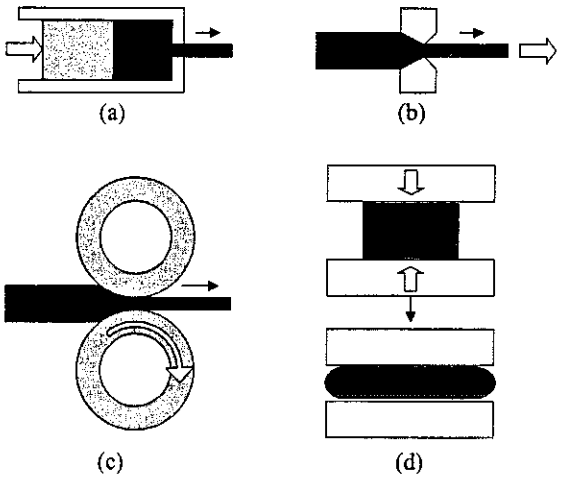

Figure 1.2: Some common mechanical deformation techniques: (a) extrusion, (b) drawing, (c) rolling, and (d) forging.

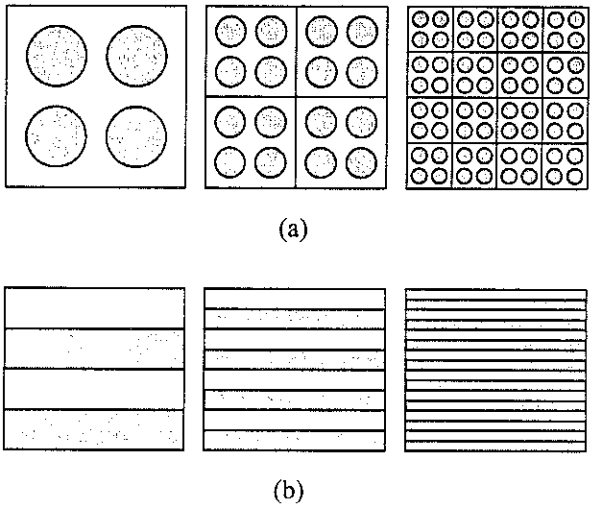

Figure 1.3: Schematic diagram of the sample cross section at consecutive stages of cyclic deformation: (a) wire matrix deformed by extrusion/drawing (b) multilayer deformed by rolling.

These simple techniques can also be used to prepare nanostructured magnetic materials. The basic idea is that firstly the sample structure (array of wires in a matrix, multilayer stack) is defined at the mm scale (*i.e.*, external sample dimensions of a few mm squared containing wires of sub-mm diameter or foils with individual thickness of the order of 100 μm). Certain dimensions of the sample (external and internal) are then gradually reduced by a given forming technique. Thus certain forming techniques are suited to certain sample geometries – drawing/extrusion for wire arrays, rolling for 1D (unidirectional) deformation of multilayers

or drawing/extrusion for 2D (radial) deformation of multilayers. As extensive deformation is required to reduce the internal dimensions to the nm scale, the sample is periodically cut and reassembled to maintain bulk external dimensions required for sample manipulation. A schematic diagram of the sample cross section at various stages of cyclic deformation is shown in figure 1.3. Mechanical deformation was used to make excellent swords for the samurai hundreds of years ago. One of the first reports on the use of the technique to produce nanocomposite magnetic materials was by F. P. Levi, who used drawing to prepare an array of Fe wires ($\phi \approx 10$ nm) in a Cu matrix [9]. These nanocomposites had coercivity of the order of 50 mT, owing to the very small diameters and anisotropic shape of the Fe components [10].

A combined extrusion/drawing process was developed by F. Dupouy et al. [11, 12] to prepare high strength nanostructured multi-filamentary Nb/Cu conductors for pulse magnet field coils. A combined hot-pressing/rolling technique was developed by Yasuna et. al. [13, 14] to produce bulk nanostructured Fe/Ag multilayers with GMR properties. In both processes the first step/technique (extrusion and hot-pressing, respectively) were primarily used to compact the sample while the greatest amount of deformation was achieved with the second step/technique.

One of the main aims of this thesis was to prepare functional magnetic materials (permanent magnets and magnetostrictive materials) by mechanical deformation. This work is the follow-on of two previous theses concerned with the development of mechanical deformation processing at Laboratoire Louis Néel [15, 16]. Before giving details of these studies, some relevant issues in the mechanical deformation of metals will now be addressed.

1.2. Mechanical deformation of metals

1.2.1. Regimes of deformation

The process by which a piece of metal changes its dimensions under an external force is called deformation. Nominal stress, σ, is the force on the object divided by the original area, nominal strain, ε, is the change in dimension divided by the original dimension. The evolution of the strain with the stress is illustrated in figure 1.4. Two distinct regimes exist, the elastic regime at low stress and the plastic regime at higher stress. Deformation is reversible in the elastic regime, *i.e.* when the stress is removed, the dimensions of the piece of metal return to

their original values. The stress-strain relation during elastic deformation follows the Hooke's law [17]:

$$\sigma = E\varepsilon \qquad \text{(Equation 1. 1)}$$

where E is Young's modulus.

Deformation is non-reversible in the plastic regime as the dimensions of the piece of metal after deformation do not return to their original values. In this case, there is no equation to relate the stress to plastic strain. When the stress reaches a certain value, the specimen will rupture.

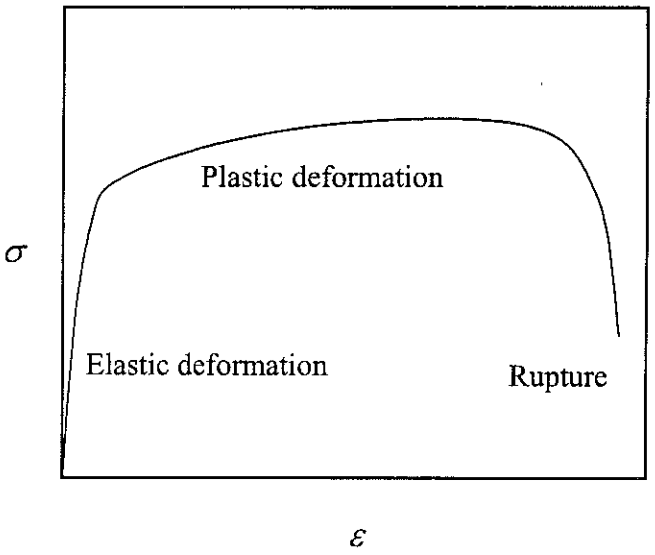

Figure 1.4: Typical stress (σ)-strain (ε) curve of a metal.

1.2.2. Mechanisms of plastic deformation

In a perfect single crystalline metal, the mechanism of plastic deformation involves sliding layers of atoms over each other. This is a shearing process and occurs as close as possible to the plane of maximum shear stress. The more closely packed together the atoms are, the easier the layers of atoms will slide relative to each other. Hence, shearing takes place in the closed-packed plane and along the closed-packed directions that are nearest to the location of maximum shear stress. Figure 1.5 shows typical slip systems in closed-packed hexagonal, face-centred cubic (fcc), and body-centred cubic (bcc) structures [17]. The number of slip systems is greater in high symmetry systems than in low symmetry systems. In the fcc

structure for example, there are four <110> close packed directions in each of the three close packed (111) planes. Thus there is a total of twelve possible slip systems. In contrast, there are only three close packed <-1-120> directions in the basal plane of a hexagonal structure.

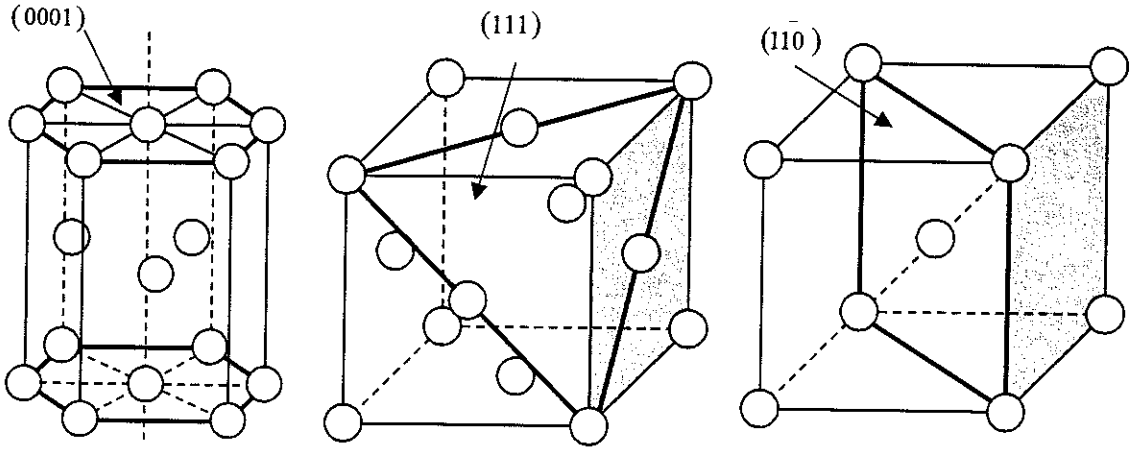

Figure 1.5: Typical slip systems in (a) closed-packed hexagonal, (b) face-centred cubic (fcc) and (c) body-centred cubic (bcc) structures [17].

In reality, where metals are not perfectly single crystalline, imperfections, especially dislocations, play a very important role. Dislocations are imperfections localised in the alignment of the layers of atoms in the lattice. These can consist of (a) layers being twisted with respect to each other, the result looks like a screw thread and so these are called *screw dislocations*; (b) an extra half plane of atoms which is an *edge dislocation* or (c) a combination of these two. An illustration of dislocations is given in figure 1.6 [18]. Dislocations can serve as a means of producing the shearing involved in plastic deformation. The key point is that dislocations can be moved through the material with only localised making and breaking of bonds, thus reducing the yield stress to a manageable level. Think about how a caterpillar moves. A caterpillar will lift a few legs at a time and pass motion along their body, rather than lifting all

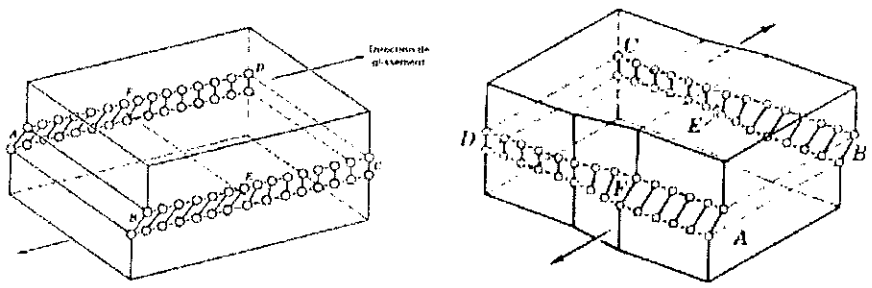

Figure 1.6: Schematic illustration of (a) edge and (b) screw dislocation [17]

of their legs at once and jumping, since the former motion requires much less motive power.

1.2.3. Work hardening and annealing

Metals and alloys undergo *work hardening* (*strain hardening*) during plastic deformation. This phenomenon is associated with the formation of new dislocations. Some dislocations are present, as random growth defects, in undeformed metals and alloys. During plastic deformation, however, many new dislocations are formed. The more dislocations that are trying to move at once, the greater possibility of dislocations becoming entangled. The result is dislocation pile-up that makes further plastic deformation more difficult. Hence, the stress required to produce further deformation is increased and work hardening occurs [18].

Unlike deformation itself, strain hardening is reversible. By heating to a sufficiently high temperature the dislocations are able to reorient themselves into networks, in a process called *recovery*. Further heating actually allows the growth of new grains with a low dislocation density. This is called *recrystallisation*. Both recovery and especially recrystallisation remove dislocation pile-ups and hence reduce the hardness of the material. The driving force is that, just as an interface (basically a defect that covers an area) has an associated energy, so does a dislocation (a line defect). Hence, removing dislocations (via a thermally activated process) reduces the energy of the material.

Materials deformed at high temperatures (*hot-worked*) will recrystallise dynamically during working, so that strain hardening is continually removed. Thus, hot working is used to reduce to manageable levels the loads required to form large components. On the contrary, strain hardening is used to strengthen metallic materials (at the price of reduced ductility) by using a forming treatment (*e.g.*, rolling) at temperatures that are too low for recovery occur. These types of treatments are known as *cold working* or *cold deformation*.

1.2.4. Deformation of composites

Composites are materials which contain more than one phase. The deformation behaviour of a composite material depends very much on the nature of the composite – volume fraction of each phase, microstructure (grain size and distribution of each phase...). Metallurgists have developed a class of composite materials, which are characterised by their very high strength. In these materials the role of the secondary phase is to limit the displacement of *dislocations* in the primary phase. The morphology of the two components is completely different - the

secondary phase is typically distributed as small precipitates throughout the primary phase. These precipitates act as obstacles to dislocation motion. The yield stress of these composite materials is mainly controlled by direct dislocation-obstacle interactions. *Macrocomposites* are another class of composite materials in which the contribution of the interfaces is neglected and the different components are of comparable volume and have similar coarse-grained morphologies. In this case, the *rule of mixture* describes rather well the behaviour of the yield stress [19]:

$$\sigma = \sum_i \%vol \cdot \sigma_i \qquad \text{(Equation 1. 2)}$$

where σ_i is the strain of component i with a given percentage of total volume. However, when mechanical deformation of macrocomposites is accompanied by a significant reduction of the internal dimensions of the involved phases, the rule of mixture is not followed (see below).

1.2.5. Deformation of nanostructured metals

Grain size is very important in plastic deformation, because there is an inverse relationship between grain size (d) and yield stress (σ), which is called the Hall-Petch relationship [20, 21]:

$$\sigma = \sigma_0 + kd^{-1/2} \qquad \text{(Equation 1. 3)}$$

where σ_0 is a friction stress, k is a constant associated with the propagation of the deformation across the boundaries. For a coarse-grained material d is large and so $\sigma \approx \sigma_0$. As grain sizes are reduced to the nanometre scale and the percentage of grain boundary atoms increases correspondingly, the traditional view of dislocation-driven plasticity in polycrystalline metals needs to be reconsidered. One of the specific features of the deformation process in nanocrystalline materials manifests itself in deviations from the Hall-Petch relationship (equation 1.5) and in some particular cases, softening of a nanocrystalline material with reduction of the mean grain size d was observed [22, 23].

1.3. Mechanical deformation at Laboratoire Louis Néel

1.3.1. Previous work on the mechanical deformation

The preparation of nanostructured magnetic materials by mechanical deformation has been studied at Laboratoire Louis Néel since 1995. During his thesis work, F. Wacquant adapted a high pressure oil chamber to use as a hydrostatic extrusion press [15, 24]. The hydrostatic extrusion press is shown in figure 1.9. The sample to be extruded is sealed inside a sample holder, known as a billet, which is placed inside a high pressure oil chamber. The oil pressure is regulated with a piston, which is connected to a hydraulic pumping circuit. When the oil is pressurised, it exerts a hydrostatic force on the billet. The pressure needed to extrude the billet through the die depends on a number of factors including the mechanical hardness of the sample/billet, the ratio of billet cross section to die bore and the geometric details of both the billet and die. Details of the billet and die design were given by F. Wacquant in reference [15]. A maximum oil pressure of 10 kbar can be reached in the press at Laboratoire Louis Néel and typical pressures of 3 – 8 kbar were required to extrude under the conditions used. Frictional forces, which are significant in conventional extrusion, are minimised in hydrostatic extrusion as direct metal-metal contact is restricted to the billet-die contact point.

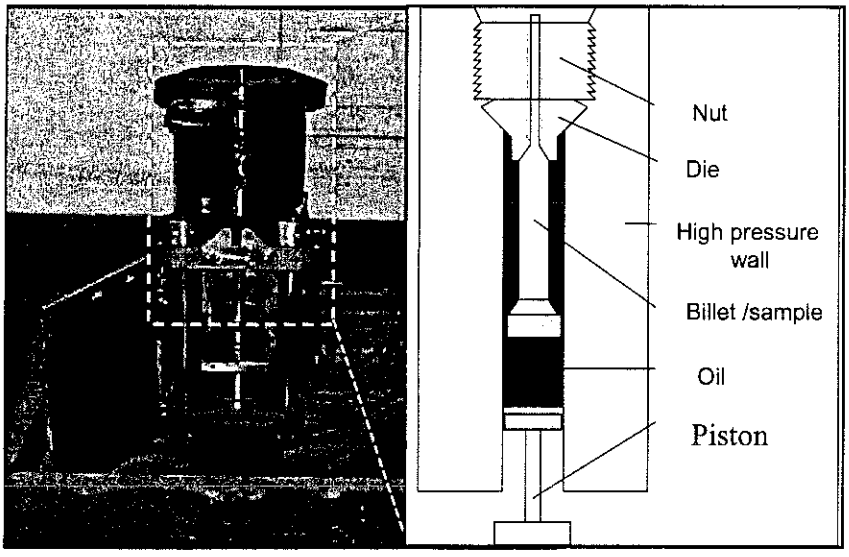

Figure 1.9: The hydrostatic extrusion press at Laboratoire Louis Néel.

Wacquant studied the hydrostatic extrusion of Fe/Cu composites. The starting sample consisted of an array of Fe wires of sub-mm diameter inserted in the holes of a circular Cu matrix. The sample was inserted in a Cu billet (outer diameter 14 mm) and extruded through a

series of three dies (bore diameters = 8.5, 6.5 and 4.6 mm). The sample/billet had to be annealed after each extrusion to relieve work-hardening (typical annealing treatment: 450°C/1 h). At the end of a given cycle, the billet diameter had been reduced by a factor three (ϕ_{init}/ϕ_{final} = 3) and thus its length had been increased by a factor nine. The extruded sample/billet was then cut into nine pieces of equal length and reassembled for insertion in a new Cu billet. It is to be noted that the reassembled sample is not compact owing to the circular cross-section of the sample pieces. In addition, as the billet becomes an integral part of the sample during extrusion, the relative quantity of Cu increased for each new cycle. Using this process, Waquant succeeded in reducing the Fe wire diameter from 200 μm to 100 nm. When attempts were made to further deform such samples, fracture occurred. The evolution in the magnetic hysteresis properties (loop shape, coercivity...) were studied as a function of the extent of deformation. Coercivities of up to 50 mT were developed [15].

In a follow-on study, A. Giguère [16] adapted details of the process to maintain the relative volume of the different components of the sample and to allow compact sample reassembly at the end of each extrusion cycle. These changes were made possible by the use of sacrificial billets which can be removed after the final extrusion step and before the reassembly step. An aluminium based alloy was chosen as the billet material as it can be easily dissolved by chemical attack (HCl or NaOH). A schematic diagram of this adapted process is shown in figure 1.10.

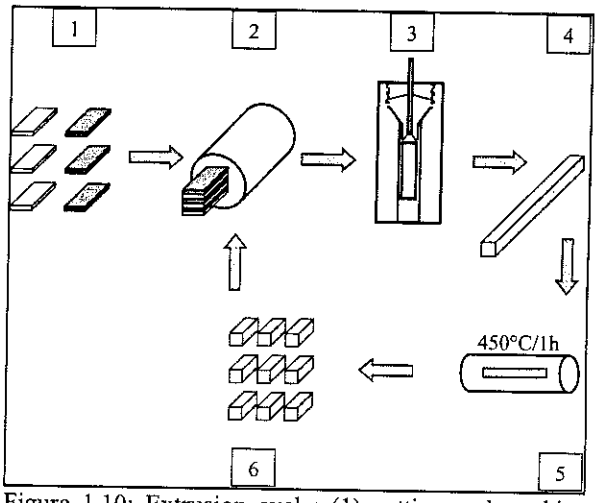

Figure 1.10: Extrusion cycle: (1) cutting and stacking of starting foils; (2) inserting into the Al billet; (3) Extrusion; (4) Taking off Al billet by chemical attack with NaOH; (5) Annealing at 450°C/1h; (6) Cutting and reassembling for next extrusion cycle.

The cross-sectional shape of the billet bore was changed from circular to square. This allowed compact reassembly as well as the possibility of extruding multilayer samples. Using this process, Giguère studied the hydrostatic extrusion of multifilamentary (Fe/Cu) and multilayer (e.g. Fe/Ag) composites with the aim to producing bulk GMR samples. It was found that for the parameters used, the final internal dimensions of the composites (wire diameter, layer thickness) were limited to some hundreds of nanometres. Further deformations lead to sample

fracture. To reach the internal dimensions needed for GMR behaviour, *i.e.* wire diameters and layer thicknesses of the order of some tens of nanometers, Giguère combined hydrostatic extrusion with rolling. This process is comparable to the combined hot-pressing/rolling process developed by Yatsuna et al. [13]. In both cases the greatest extent of deformation is achieved during the rolling stage. Giguère reduced the individual layer thicknesses in his multilayer samples from 100 μm to 10 nm in four extrusion/rolling cycles. Strong crystallographic texture, characteristic of rolling, was developed during the deformation process. In the case of Fe/Ag, an epitaxial-like relation is developed between the Fe and Ag layers, resulting in Ag texture which is non-characteristic of rolled fcc metal [25].

1.3.2. Extrusion vs rolling at Laboratoire Louis Néel

The ability to deform a material depends upon both the mechanical hardness of the material being deformed and the extent to which you deform the material in a given deformation operation – i.e. the change in sample dimensions during one extrusion step or one rolling pass. The extent of deformation during extrusion is determined by the ratio of the billet diameter and the diameter of the bore of the die through which the sample is extruded. With the extrusion set-up used at Laboratoire Louis Néel, a series of three dies of different bore diameter are available. The extent of deformation during a given operation results in significant work hardening, and thus samples must be annealed after each extrusion step. In rolling, the extent of deformation per pass is controlled by the spacing between each roll, and the amount of deformation per pass can be minimised by reducing the spacing rather gradually. Under the described conditions used, rolling is a "gentler" process than extrusion, which may explain the fact that nanometre dimensions could be reached when rolling was applied. Besides, owing to the more gradual deformation, it is not necessary to anneal the sample between each rolling pass. This is a very significant fact when considering the total time and effort of sample processing.

1.3.3. Co-deformation of miscible metals

In the experiments mentioned above, deformation of composite systems containing immiscible components (e.g. Fe and Cu; Fe and Ag) was studied. One of the principle aims of this thesis was to study the preparation of intermetallic phases by co-deformation followed by annealing of miscible metals. The first system to be studied contained Sm and Fe and the aim was to prepare magnetostrictive $SmFe_2$. Only limited deformation was possible, primarily

owing to the complicated rhombohedral crystal structure of Sm. This study was carried out in overlap with A. Giguère and preliminary results were already given in his thesis. Extrusion alone was used for this system, and details of this study are given in chapter 5.

The other system studied contained Fe and Pt and the aim was to prepare materials based on the hard magnetic FePt phase. This study was motivated by reports of the preparation of high energy product FePt thin films by annealing of Fe/Pt multilayers with individual layer thicknesses of the order of a few nanometres [26]. Thus in this case the aim was to co-deform Fe/Pt to the nanometre scale. The extrusion/rolling process developed by Giguère was found to be unsuitable as the heat-treatment required to relieve work-hardening produced during the extrusion step lead to the formation of FePt alloys at the Fe-Pt interfaces. The formation of the intermetallic phases rendered the sample brittle and thus it could not be further deformed.

1.3.4. Sheath-rolling

As explained above, heat-treatment may be avoided during rolling if the extent of deformation per pass is minimised. Thus, a deformation process involving rolling alone was established in this thesis for the preparation of Fe/Pt. The "sheath-rolling" process is schematised in figure 1.11 and pictures of various stages of the process are shown in figures 1.12.a–g.

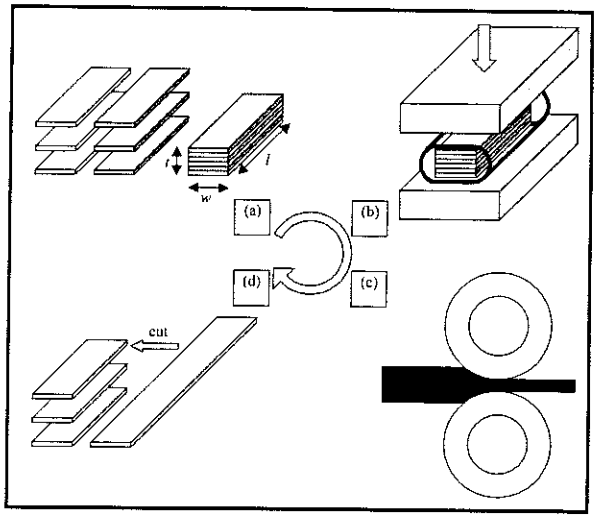

Figure 1.11: Sheath rolling process: (a) cutting and stacking of starting foils, (b) stack insertion in stainless steel tube followed by compaction in a press, (c) rolling, (d) cutting of deformed stack for re-assembly.

Starting metal sheets with thickness of the order of 100 μm were cut into small pieces (foils). The precise choice of thickness depends on the alloy composition sought. The foils were then annealed at high temperature. The foils were piled up to make a stack with dimension $t \times w \times l$ (experimentally, $l \geq 3w$, $w \geq 3t$). The stack was inserted in a stainless tube and the ensemble was compacted under a uniaxial force by pressing it in a uniaxial press (5 tons/cm^2) under ambient conditions. Stainless steel tubes of wall thickness 1mm and with diameters in the range 4 – 6 mm were used. The tube diameter was selected so that the multilayer stack just fits inside the tube. A tube length of roughly three times the sample length was used – if the tube is shorter the sample may exit during rolling while longer lengths are of no particular benefit. At the end of a given rolling cycle, the stainless steel tube edges were cut off, the top steel layer removed and the sample simply lifted off the bottom steel layer (figures 1.12.f). A given rolling cycle consisted of roughly 100 passes and the sample thickness was typically reduced by a factor ten ($t_{init} / t_{final} \approx 10$ with t_{final} of the order of 100 μm). Thus 4 – 5 such rolling cycles were required to reduce the individual layer thickness from 100 μm to 10 nm. There was no intermediate heat treatment after each such rolling cycle.

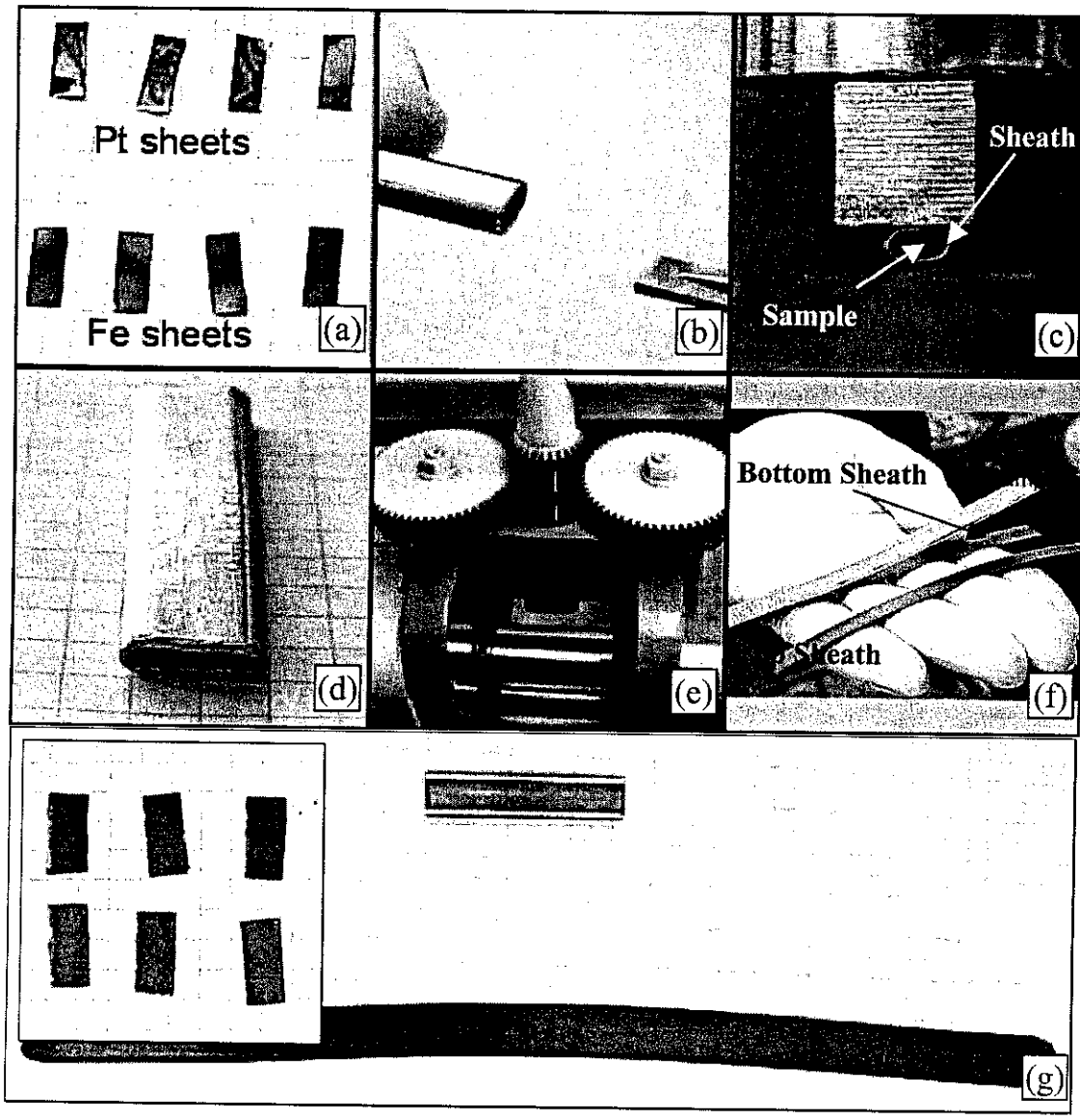

Figure 1.12: Images taken at various stages of a multi-pass cycle of the sheath-rolling process for the preparation of nanostructured multilayer Fe/Pt. (a) The starting Fe and Pt sheets; (b) stacking of Fe and Pt sheets and stack insertion in stainless steel tube (c) compaction in a press at ambient condition, (d) sample/sheath after pressing (e) rolling machine (f) removal of sample from the sheath (g) sample/sheath before and after rolling, (inset of g - deformed stack after cutting of for re-assembly).

References

1. Siegel, R.W., *Nanophase Materials*, in *Encyclopedia of Applied Physics*, E.H. Immergut, Editor **11**. (1998), John Wiley and Sons. p. 173.
2. Yoshizawa, Y., S. Oguma, and K. Yamauchi, *New Fe-based soft magnetic alloys composed of ultrafine grain structure.* J. Appl. Phys., **64** (1988) 6044.
3. Coey, J.M.D., *Rare-earth iron permanent magnets.* (1996), Oxford: Clarendon Press.
4. Baibich, M.N., J.M. Broto, A. Fert, F. Nguyen Van Dau, F. Petroff, P. Etienne, G. Creuzet, A. Friederich, and J. Chazelas, *Giant Magnetoresistance of (001)Fe/(001)Cr Magnetic Superlattices.* Phys. Rev. Lett., **61** (1988) 2472.
5. Meiklejohn, W.H. and C.P. Bean, *New Magnetic Anisotropy.* Phys. Rev., **102** (1956) 1413.
6. Meiklejohn, W.H. and C.P. Bean, *New Magnetic Anisotropy.* Phys. Rev., **105** (1957) 904.
7. Coehoorn, R., D.B. de Mooij, J.P.W.B. Duchateau, and K.H.J. Buschow, J. de Phys., **49** (1988) C8 669.
8. Moriya, T., *Spin Fluctuation in Itinerant Electron Magnetism*, in *Springer Series in Solid State Sciences* **56**. (1985), Springer: Berlin.
9. Levi, F.P., Nature, **183** (1959) 1251.
10. Levi, F.P., J. Appl. Phys., **31** (1960) 1469.
11. Dupouy, F., S.F. Askenazy, J.-P. Peyrade, and D. Legat, Physica B, **211** (1995) 43.
12. Dupouy, F., Thesis (1995), Institut National des Sciences Appliquées de Toulouse: Toulouse.
13. Yasuna, K., M. Terauchi, A. Otsuki, K.N. Ishihara, and P.H. Shingu, *Bulk metallic multilayers produced by repeated press-rolling and their perpendicular magnetoresistance.* J. Appl. Phys., **82** (1997) 2435.
14. Yasuna, K., *Nanoscale multilayer produced by mechanical processing*, Thesis (1997), Kyoto University: Kyoto.
15. Wacquant, F., *Elaboration et étude des propriétés de réseaux de fils magnétiques submicroniques, obtenus par multi-extrusions*, Thesis in *Physics* (2000), Université Joseph Fourier - Grenoble 1: Grenoble.
16. Giguère, A., *Préparation et étude des propriétés magnétiques et de transport de nanomatériaux obtenus par extrusion hydrostatique et laminage*, Thesis in *Physics* (2002), Université Joseph Fourier - Grenoble 1: Grenoble.
17. Honeycombe, R.W.K., *The Plastic Deformation of Metals.* (1968): Edward Ltd. p. 325.
18. Cottrell, A.H., *An introduction to Metallurgy.* (1967), Edward Arnold: London. p. 386.
19. Taya, M. and R.J. Arsenault, *Metal Matrix Composites.* (1989), New York: Pergamon. 23.
20. Hall, E.O., *The deformation of mild steel: III Discussion of Results.* Proccedings of Physical Society of London, **B 64** (1951) 474.

21. Petch, N.J., *The cleavage strength of polycrystals.* Journal of Iron Steel Instruments, **174** (1953) 25.

22. Gutkin, M.Y., I.A.Ovid'ko, and C.S.Pande, *Theoretical Models of Plastic Deformation Processes in Nanocrystalline Materials.* Review on Advance Materials Science, (2001).

23. Lasalmonie, A. and J.L. Strudel, *Review Influence of grain size on the mechanical behaviour of some high strength materials.* Journal of materials Science, **21** (1986) 1837.

24. Wacquant, F., S. Denolly, A. Giguère, J.P. Nozières, D. Givord, and V. Mazauric, *Magnetic properties of nanometric Fe wires obtained by multiple extrusions.* IEEE Trans. Magn., **35** (1999) 3484.

25. Giguère, A., N.M. Dempsey, M. Verdier, L. Ortega, and D. Givord, *Giant Magnetoresistance in Bulk Metallic Multilayers Prepared by Cold Deformation.* IEEE Trans. Magn., **38** (2002) 2761.

26. Liu, J.P., C.P. Luo, Y. Liu, and D.J. Sellmyer, *High energy products in rapidly annealed nanoscale Fe/Pt multilayers.* Appl. Phys. Lett., **72** (1998) 483.

Chapter 2: Hard magnetic FePt foils prepared by mechanical deformation

Résumé en Français

Chapitre 2: Feuilles magnétiques dures FePt préparées par déformation mécanique

Le système fer-platine est de grand intérêt pour les études de magnétisme du fait de la diversité des états magnétiques qui peuvent y être observées : ferromagnétisme (doux ou dur), antiferromagnétisme ou paramagnétisme. Les paramètres physiques caractérisant chacun de ces états sont la composition chimique, le degré d'ordre chimique et la température. La forte anisotropie de la phase $L1_0$ du système équiatomique FePt a attiré une attention toute particulière, en raison des applications possibles en enregistrement magnétique ou pour la fabrication d'aimants permanents. Au cours de cette thèse, un procédé original d'élaboration a été développé, utilisant le laminage sous gaine, pour la préparation de feuilles magnétiques dures de FePt. Dans ce chapitre, nous présentons les différentes phases du système Fe-Pt et leurs propriétés magnétiques. Nous expliquons ensuite quelles sont les diverses méthodes de préparation de matériaux durs FePt, présentées en détail dans une revue récente de A. Cebollada et al. [3]. Dans le cœur de ce chapitre nous décrivons la préparation et la caractérisation structurale de FePt par déformation sévère de feuilles de fer et platine, puis recuit. Les propriétés magnétiques de ces matériaux sont ensuite discutées en référence à chaque microstructure particulière obtenue.

Une coercitivité relativement forte a été obtenue dans les matériaux préparés. Nous attribuons ce résultat au degré d'ordre important des atomes Fe et Pt au sein de la phase $L1_0$, atteint par le procédé de déformation mécanique utilisé pour la préparation du matériau ainsi qu'à la microstructure particulière caractéristique du procédé. Nous avons réussi à augmenter encore la coercitivité grâce à l'introduction d'un certain pourcentage d'argent dans les alliages. Nous pensons que cette augmentation de coercitivité résulte de la combinaison de deux mécanismes. D'une part, l'argent est source d'une augmentation de la ductilité du matériau, qui peut donc être déformé jusqu'à un degré supérieur ; d'autre part, l'argent, précipité aux joints de degré, contribue au découplage d'échange entre grains magnétiques durs. Il en

résulte que la coercitivité augmente progressivement avec le pourcentage d'argent introduit. Bien sûr cette augmentation de coercitivité se fait au prix d'une réduction de l'aimantation du matériau, du fait d'une relative dilution de la phase magnétique.

Nos efforts pour préparer des matériaux FePt/Fe_3Pt, de type « spring-magnet », ont été infructueux. Les processus d'aimantation que nous avons observés sont les mêmes que pour des phases dure et douce non couplées. Nous pensons que ce comportement doit être attribué à la taille trop importante des grains doux Fe_3Pt. Cependant les processus d'aimantation ont révélé des particularités qui sont décrites au chapitre 4 par la prise en compte des interactions dipolaires entre grains. Les efforts pour préparer des systèmes FePt/$FePt_3$, présentant le phénomène de décalage d'échange ont été infructueux également. Dans ce cas, la phase $FePt_3$ ne présentait pas la structure magnétique de type antiferromagnétique espérée, mais elle était ferromagnétique.

Les travaux décrits dans ce chapitre établissent la possibilité de préparer des matériaux composites formés de phases intermétalliques en utilisant une méthode de déformation mécanique puis recuit. Cependant, cette méthode prendrait une autre dimension si une voie était trouvée pour réduire la dimension des éléments constitutifs plus loin dans les dimensions nanométriques.

Chapter 2: Hard magnetic FePt foils prepared by mechanical deformation

The iron-platinum system is of great interest in magnetism owing to the range of magnetic states – ferromagnetic (soft or hard), antiferromagnetic, paramagnetic – which it possesses. The magnetic state of a given Fe-Pt alloy is determined by its composition and degree of chemical order as well as its temperature. The high anisotropy $L1_0$ FePt alloy has attracted much attention due to its potential use in magnetic recording [1] and permanent magnet applications [2]. In the course of this thesis a novel processing route, namely *sheath-rolling*, was developed to prepare hard magnetic FePt-based foils. In this chapter we firstly describe the Fe-Pt system and then briefly review the state-of-the-art in the preparation of the hard magnetic $L1_0$ phase. For more details, the reader is referred to an excellent recent review by A. Cebollada *et. al.* [3]. Following this we describe the preparation and characterisation of the material by severe co-deformation of Fe and Pt foils followed by annealing. The magnetic properties obtained are discussed in reference to the particular micro-structures obtained.

2.1. The Fe-Pt system

2.1.1. Crystal structures of the Fe-Pt system

The Fe-Pt system has a continuous range of solid solutions at high temperature and 3 stoichiometric alloys Fe_3Pt, FePt and $FePt_3$ at lower temperatures (figure 2.1 [4]). These stoichiometric phases can exist in a *disordered* state in which the statistical distribution of the Fe and Pt atoms is substitutionally random, or in a partially or completely *ordered* state in which the Fe and Pt atoms occupy specific sites (figure 2.2). A fully ordered alloy is known as a *superlattice* or *superstructure*. All three stoichiometric phases have a face-centered-cubic (fcc) structure in the disordered state. In the ordered state, the $FePt_3$ and Fe_3Pt have an fcc structure of the $L1_2$ ($AuCu_3$ type). In contrast, ordered FePt has a face-centered tetragonal (fct) structure of the $L1_0$ (AuCu type). Values of the lattice parameters of these phases in the ordered and disordered states are given in the table 2.1 and the ordered state structures are shown in figure 2.3. In the $L1_2$ ordered Fe_3Pt ($FePt_3$) phase, the Pt (Fe) atoms occupy the 000

site and the Fe (Pt) atoms occupy ½½0, 0½½, ½0½ sites. In the $L1_0$ ordered FePt phase, the Fe (000, ½½0) and Pt (½0½, 0½½) atoms form alternate layers along the *c*-axis, resulting in a tetragonal distortion with respect to the disordered cubic phase.

Table 2.1: Crystal structure parameters of the Fe_3Pt, FePt, $FePt_3$ phases in the ordered and disordered states [3].

	Disordered		Ordered		
	Structure	Lattice parameter (Å)	Structure	Lattice parameter (Å)	c/a
Fe_3Pt	Face-centered cubic	3.72	Face-centered cubic	3.73	-
FePt	Face-centered cubic	3.80	Face-centered tetragonal	3.86	0.96
$FePt_3$	Face-centered cubic	3.86	Face-centered cubic	3.87	-

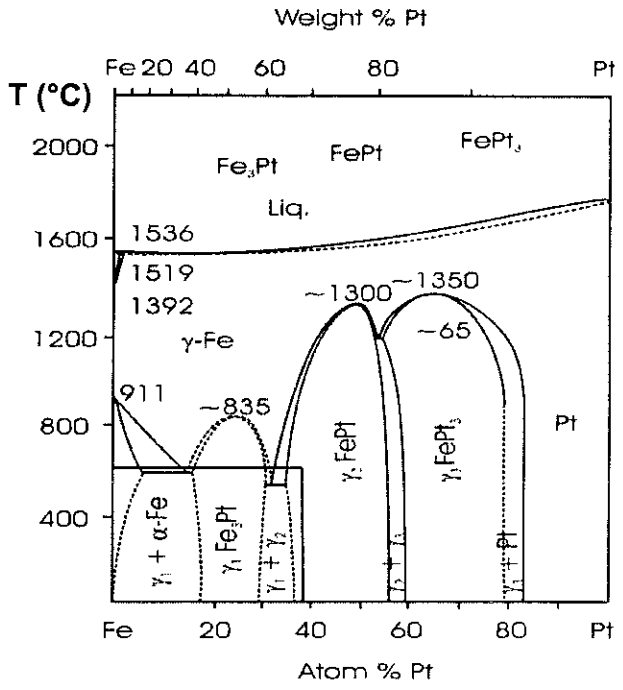

Figure 2.1: The Fe-Pt phase diagram [4].

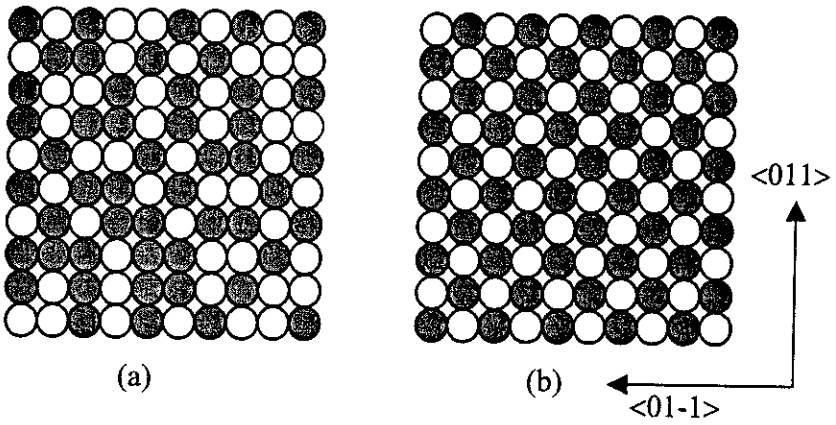

Figure 2.2: Schematic models of (a) disordered and (b) ordered phase of FePt alloy. The open and solid circles represent for Fe and Pt atoms, respectively.

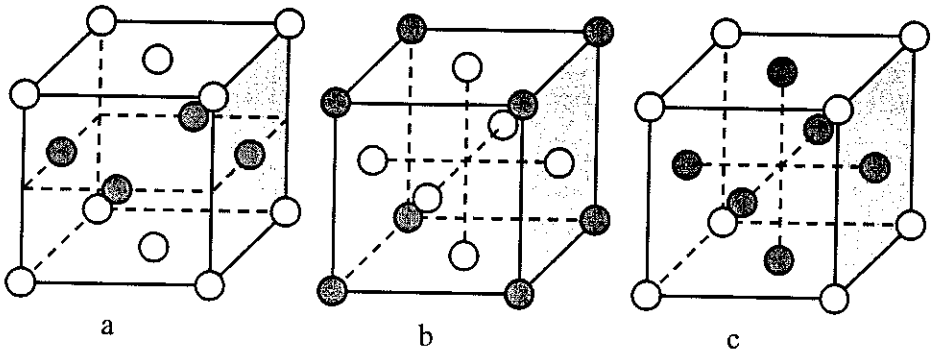

Figure 2.3: Ordered structures (a) $L1_0$ FePt, (b) $L1_2$ Fe_3Pt, (c) $L1_2$ $FePt_3$. The open and solid circles represent for Fe and Pt atoms, respectively.

Order-disorder transformation

On the basis of thermodynamics, it can be shown that an ordered arrangement of atoms in an alloy may produce a lower internal energy compared to a disordered arrangement, resulting in the formation of a superstructure at low temperatures [5]. At higher temperatures, thermal agitation gives rise to atom mobility, which acts to reduce the order of the superstructure. The change in structure from the ordered to the disordered states and vice versa is called the *order-disorder transformation*. The temperature above which no order remains is called the *critical temperature*. The FePt alloy has a critical temperature of 1300°C [4]. The order-disorder transformation in FePt is a first-order transformation [5]. Though the ordered phase is the thermodynamically stable phase below the critical temperature of 1300 °C, the disordered phase may be stabilized below this temperature (*e.g.* by quenching bulk samples from high temperature or depositing thin film samples at room temperature, see section 2.1.2). In this case the disordered phase is transformed to the ordered phase by annealing at

temperatures below the critical temperature. The annealing has to be controlled so that the atoms have enough thermal energy to move to their correct.

Degree of order

The degree of long-range order (S), is determined by the arrangement of atoms over the entire crystal and may be define as [6]:

$$S = \frac{r_{Fe} - x_{Fe}}{y_{Pt}} = \frac{r_{Pt} - x_{Pt}}{y_{Fe}} \qquad \text{(Equation 1. 4)}$$

Where $r_{Fe(Pt)}$ is the fraction of Fe(Pt) sites in the lattice occupied by the right atoms, $x_{Fe(Pt)}$ the atomic fraction of Fe(Pt) in sample, $y_{Fe(Pt)}$ the fraction of Fe(Pt) sites. The parameter S is zero for a completely random arrangement, and S reaches unity for a perfectly ordered arrangement. In reality, S is usually less than 1 because of the presence of various imperfections, grain boundaries, antiphase domains, and variation in composition away from the stoichiometric composition. Quantification of order in FePt using X-ray diffraction data is detailed in annexe B.

2.1.2. Magnetic properties of the Fe-Pt system

Magnetism can only exist in systems which contain unfilled electron shells. In metals, ferromagnetism results from exchange interactions, which induce band splitting so that the population of the majority up spin band and of the minority down spin band are different. As there is competition between exchange energy and kinetic energy, this is only observed in the narrow 3d band of Fe, Co, and Ni.

A number of other itinerant electron systems, such as Pd, Rh, and Pt are almost magnetic. When such elements are alloyed with one of the 3d ferromagnetic elements, hybridisation induces a moment, which can amount to a significant fraction of a Bohr magneton. As a result, in systems such as the Fe-Pt, the magnetic properties result from the combination of the specific properties of 3d and 5d electrons. In particular, Pt is a heavy metal and large spin-orbit coupling favours an asymmetric electron distribution. In an alloy with uniaxial crystal structure, large magnetocrystalline anisotropy is expected. This is the case of the $L1_0$ phase. Intrinsic magnetic properties of the various phases of the Fe-Pt system are given in table 2.2.

Table 2.2: Magnetic properties of the Fe_3Pt, FePt, $FePt_3$ phases in the ordered and disordered states [3].

	Disordered	Ordered
Fe_3Pt	Ferromagnetic, T_c = 260 K	Ferromagnetic, T_c = 450 K $\mu_0 M_s$ = 1.8 T
FePt	Ferromagnetic	Ferromagnetic, T_c = 750 K $\mu_0 M_s$ = 1.4 T, $K_2 = 7\times10^6$ J/m^3
$FePt_3$	Ferromagnetic	Two antiferromagnetic states, T_{N1} = 100 K, T_{N2} = 160 K

Table 2.3: Intrinsic properties of the FePt in comparison with other candidates for permanent magnets and recording media.

	Material	K_2 (10^6 J/m^3)	$\mu_0 M_s$ (T)	T_c (K)
Permanent magnets	AlNiCo			1130
	Ferrite			<520
	$SmCo_5$	11 – 20	1.14	1000
	$Nd_2Fe_{14}B$	4.6	1.60	590
	FePt	**6.6 – 10**	**1.43**	**750**
Recording media	FePd	1.8	1.39	800
	CoPt	4.9	1.00	825
	MnAl	1.7	0.7	
	CoCrPtX	0.2	0.25 – 0.38	
	Co	0.45	1.76	
	Hex Co_3Pt	2.0	1.39	750

Hard magnetic FePt

As mentioned in the introduction, the equiatomic ordered $L1_0$ FePt phase has been extensively studied because its intrinsic hard magnetic properties make it a potential candidate for magnetic recording and permanent magnet applications. These properties are compared with those of other high anisotropy magnet materials (*i.e.*, its competitors) in table 2.3. It can be seen that its intrinsic magnetic properties are comparable to those of the RE-TM alloys which form the basis of today's high performance magnets. Admittedly, the price of Pt renders the

material non-competitive for conventional bulk applications. However, niche markets may soon exist for sub-micron sized magnets for micro-system applications [7]. For use in these applications and in thin film form for magnetic recording media (i.e. high value added products), material costs should be less critical.

2.1.3. Preparation of hard magnetic FePt – state of the art

Bulk processing

In the classical bulk route [8-11], Fe and Pt were melted together in an arc-melting chamber or induction furnace under vacuum or inert atmosphere. These alloys were then homogenized at high temperature (≥1200 °C). At the end of the homogenisation treatment, the samples were quenched to produce disordered alloys. Ordering was achieved by annealing at temperatures in the range 600 – 800 °C. Maximum coercivities of about 0.5 T were reported for this preparation technique. Samples thus prepared were crystallographically isotropic, owing to the three variants for tetragonal distortion of the cubic disordered precursor. More recently, nanocomposite bulk samples containing exchange-coupled hard and soft grains have been prepared by controlled annealing of homogenised alloys [10].

Thin film processing

Thin film deposition techniques such as sputtering [2, 12-14], molecular beam epitaxy (MBE) [12] and pulsed laser deposition (PLD) [15] have been used to produce thin film FePt samples. The ordered phase can be prepared directly by 1) sequential monolayer deposition (elemental targets/sources) or 2) co-deposition onto heated substrates (elemental or alloy targets/sources). Alternatively it can be achieved by 1) annealing of disordered films deposited at room temperature or 2) annealing of Fe/Pt multilayers. Under certain conditions, crystallographic texture may be obtained in thin films owing to the preferential crystallization along the materials most dense crystallographic directions (fibber texture) on polycrystalline substrates [16] or epitaxial growth on single crystalline substrates [13, 17]. Room temperature coercivity values of typically 1-2 T are obtained for thin film samples. There has been a recent report of coercivities as high as 4 T for a thin film consisting of isolated epitaxial nanosized grains [18]. High coercivities have also been reported for nanocomposite materials combining FePt with nonmagnetic phase [19].

Chemical processing

Chemical techniques such as electro-deposition [20] or solution phase synthesis [21] have also been applied to produce hard magnetic FePt. In the first technique, FePt nanowires embedded inside an array of empty holes in anodised aluminium disks are produced. Coercivity of the order of 0.5 T was reported. In the latter technique, nanosized particles (3-10 nm in diameter) of FePt are produced by reduction of Pt acetylacetonate and decomposition of Fe pentacarbonyl [21]. The as-formed nanoparticles are disordered and may be ordered by annealing in the temperature range 500 – 600 °C. Samples thus produced are crystallographically isotropic. Two-phase materials combining the hard magnetic $L1_0$ FePt phase with the soft magnetic Fe_3Pt phase have also been produced by this technique. Coercivity of 2 T and energy product of 160 kJ/m^3 were reported [22].

2.2. Preparation of hard magnetic FePt-based foils by sheath-rolling

The above mentioned reports on the preparation of FePt in thin film formed by annealing of Fe/Pt multilayers [2] motivated us to explore the possibility of preparing the alloy by co-deformation followed by annealing of Fe and Pt foils. Co-deformation to the nm-scale (*i.e.* individual layer thicknesses on the nanometre scale) was aimed for so as to (1) minimise the length scale over which the atoms must diffuse to form the desired phase (*i.e.* minimise reaction temperatures and times) and (2) minimise the grain size of the intermetallic grains formed during annealing. The deformation of intermetallic phases is very difficult and thus it was necessary to avoid heat treating the Fe/Pt sample before the final deformation to prevent the formation of Fe-Pt phases at the interfaces. It was for this reason that the"sheath-rolling" technique described in section 1.3.4 was developed.

In the first case the aim was to prepare single-phase FePt samples. Following this, the possibility of preparing composite systems mixing FePt with a secondary phase (non-magnetic Ag, soft magnetic Fe_3Pt or antiferromagnetic $FePt_3$) was explored. The desired role of the second phase was very different in each case. The intended role of the Ag was to increase the sample coercivity by magnetically isolating FePt grains from each other (*c.f.* - use of non-magnetic phases in composite thin film samples [19]). That of the Fe_3Pt was to increase the remanence of the system [2, 23], while the role of $FePt_3$ was to create an exchange bias [24].

Commercial foils of Fe (99.5 %), Pt (99.9 %) and Ag (99.9 %) were used. Some physical properties of these metals, taken from literature, are given in table 2.4. All foils were annealed to relieve work hardening developed during their preparation (700 °C/1h for Fe and Pt, 500 °C /1h for Ag, followed by cooling at a rate of 500 °C/1 h).

Table 2.4. Some physical properties of Fe, Pt and Ag.

Element	Structure	Lattice (A°)	Density (g/cm^3)	Melting point (°C)	Vickers hardness (MN/m^2)
Fe	Bcc	2.87	7.87	1538	608
Pt	Fcc	3.92	21.09	1768	549
Ag	Fcc	4.09	10.49	961	251

Table 2.5: Details of the various FePt-based samples prepared.

Starting sample (μm)	Sample name (as-rolled)	Predicted Fe-Pt composition	Vol % of the 2nd phase	Number of rolling cycles	Sample name (post-annealed)
Fe/Pt: 75/100	Fe/Pt	FePt		4	FePt
Fe/Ag/Fe/Pt: 50/20/25/100	Fe/Pt/Ag20	FePt	7 %	5 – 6	FePt/Ag20
Fe/Ag/Fe/Pt: 50/100/25/100	Fe/Pt/Ag100	FePt	36 %	5 – 6	FePt/Ag100
Fe/Pt: 120/100	Fe-rich Fe/Pt	FePt + Fe_3Pt	35 %	4	Fe-rich FePt
Fe/Pt: 100/100	Pt-rich Fe/Pt	FePt + $FePt_3$	33 %	4	Pt-rich FePt

Details of the various samples prepared are given in table 2.5. The relative thicknesses of the Fe and Pt foils were chosen according to the final intermetallic(s) sought for: single phase FePt: 50 at% Fe + 50 at% Pt; two-phase FePt/Ag: 50 at% Fe + 50 at %Pt + Ag (7 and 36 vol %); two-phase FePt/Fe_3Pt: 66 at% Fe + 34 at %Pt; two-phase FePt/$FePt_3$: 56 at% Fe + 44 at %Pt; the expected volume content of the secondary phases are given in table 2.5. As mentioned above, the intended aim for the Ag was to isolate FePt grains formed during the post-deformation annealing treatment. In fact Ag is known to alloy with Pt above 700°C. Thus to prevent the formation of Ag-Pt alloys, which would reduce the amount of Pt available to alloy with Fe, the Ag foils were interleaved between Fe foils to avoid direct contact between the Ag and Pt foils.

Typical starting multilayer stack dimensions of 2×6×15 mm^3 were used. The "sheath rolling" technique described in section 1.3.4 was applied. While the number of rolling cycles for the

Fe/Pt samples was limited to 4 (the samples were too brittle to deform further), the Ag containing samples could be submitted to up to 6 cycles. The greater deformability of these samples may be attributed to the presence of Ag, which is a relatively soft and thus easily deformed (table 2.4).

From now on, unless otherwise stated, the term "as-rolled" sample is understood to mean the sample after the final deformation cycle. The final multilayer foils had a typical total thickness of about 100 μm. Pieces of these foils were then sealed under vacuum (10^{-5} mbar) in quartz tubes and annealed in a muffle furnace at temperatures in the range 300 °C – 700 °C for time in the range 30 seconds – 48 hours.

2.3. Structural characterisation of the deformed multilayers

Representative SEM images of deformed samples taken at different stages of deformation are shown in figure 2.4. The overall multilayer structure is seen to be quite well preserved right down to the last deformation cycle. A distribution in layer thickness is observed, but the average layer thickness is in agreement with the bulk reduction factor (starting foil thickness/final foil thickness, typically $t_{init}/t_{final} \approx 10$ for one cycle).

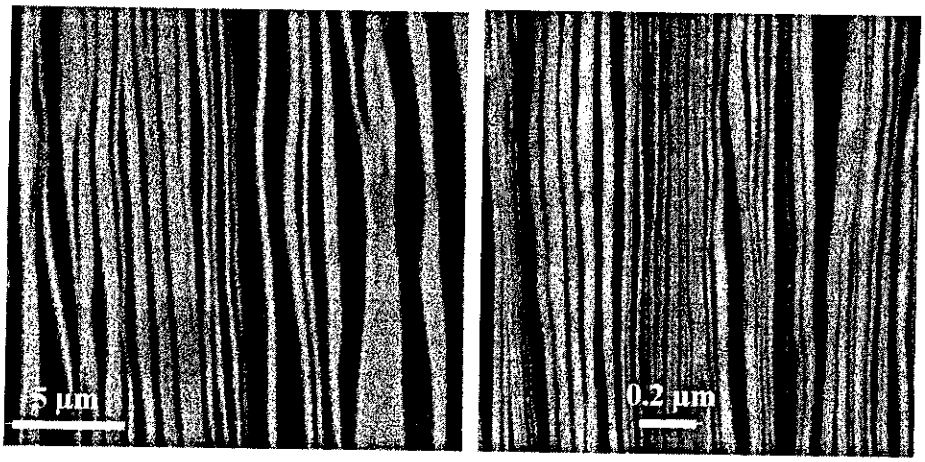

(a) (b)

Figure 2.4: SEM images of the Fe/Pt sample after (a) 2 and (b) 4 rolling cycles.

2.3.1. XRD patterns of the as-rolled samples

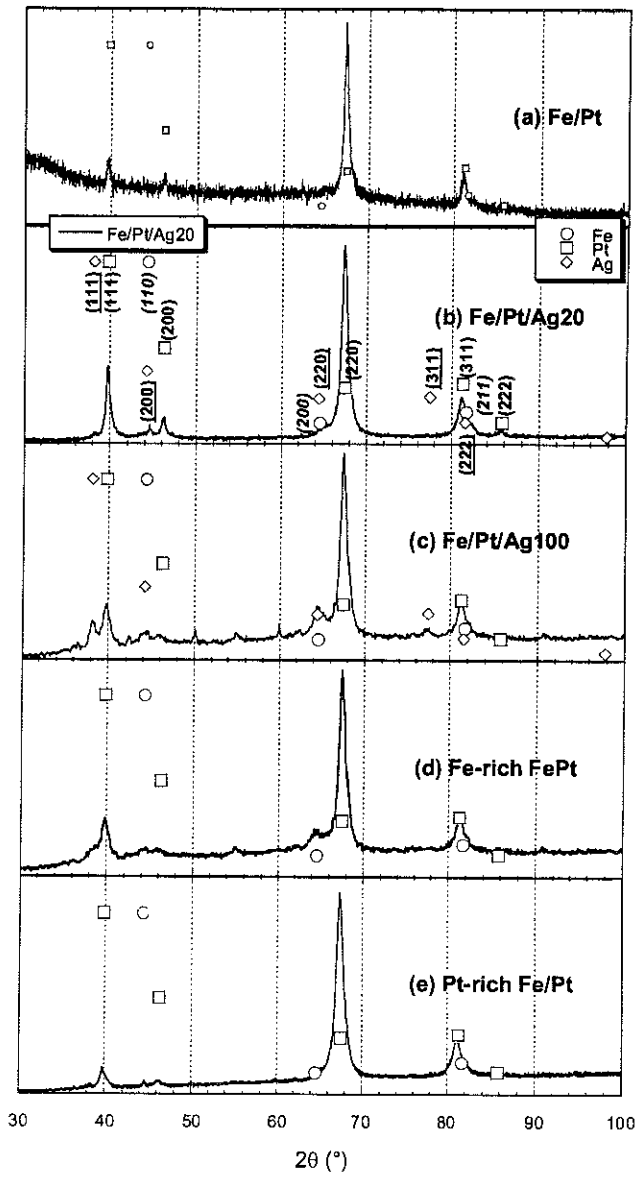

Figure 2.5: XRD patterns of the as-rolled (a) Fe/Pt, (b) Fe/Pt/Ag20, (c) Fe/Pt/Ag100, (d) Fe-rich Fe/Pt and (e) Pt-rich Fe/Pt multilayers. The pdf file is also present.

XRD patterns (θ–2θ geometry) of the as-rolled samples and the pdf patterns of Fe, Pt and Ag are given in figure 2.5. It can be seen that the relative intensity of the (220) diffraction peak of Pt is much higher than that of the isotropic powder Pt pattern, which indicates that the Pt layers are (220) in-plane textured, as expected for rolled fcc metals [25].

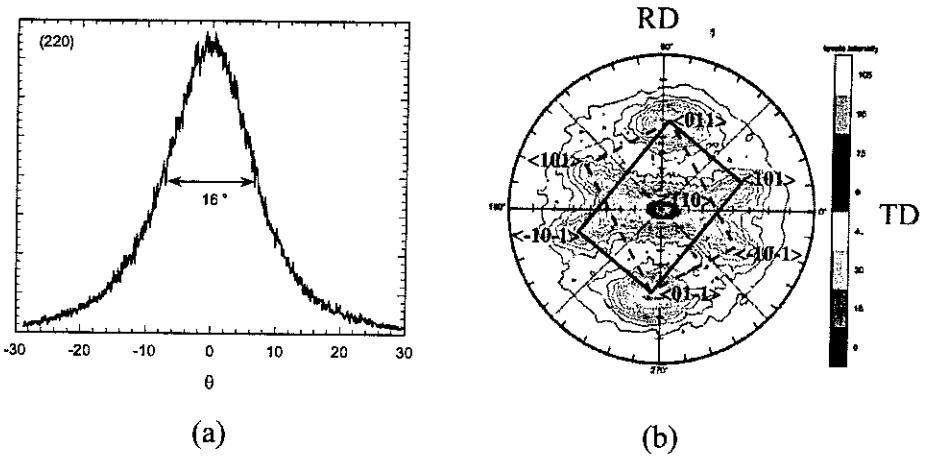

Figure 2.6: Rocking curve about Pt(220) peak and (b) pole figure of the as-rolled Fe/Pt (RD: Rolling Direction, TD: Transverse Direction).

The texture of the Pt layers in the deformed multilayer is confirmed from the rocking curves (figure 2.6.a) and the pole figures (figure 2.6.b) of the sample after the final deformation cycle. The full width at half maximum (FWHM) of the rocking curve of the (220) peak, which can be considered as the average angle of the <220> axis around the normal direction to the rolling plane, is about 16°. The (111)<112> twinning system, typical of rolled fcc metals, was identified. The intensity of the Fe peaks are much lower than those of the Pt peaks owing to the lower atomic mass of Fe relative to Pt, nevertheless, the (200) texture expected for bcc metals is discernible (figure 2.5). In the Ag containing samples, the Ag is also observed to have (220) texture (this in inferred from the pattern of the sample Fe/Pt/Ag100, in which the Ag peaks are most clearly resolved).

2.3.2. Structural evolution as a function of annealing conditions

The FePt series

It had been reported that hard FePt could be formed by annealing multilayer Fe/Pt films at temperatures in the range 400 °C – 500 °C [2]. Based on these results, we fixed our annealing temperature (T_a) to be 500 °C and varied the annealing time (t_a) from 30 seconds to 20 hours. The XRD spectra of these samples are given in figure 2.7. When the annealing time is too short – 30 seconds, the XRD patterns are comparable to that of the as-rolled sample in which Pt reflections are dominant. However, reflections of the $L1_0$ FePt phase, including superstructure reflections, dominate the spectra for $t_a \geq 2$ minutes. The strong (220) reflection

of Pt has been suppressed after just 2 minutes and some low intensity peaks are attributed to $FePt_3$. The diffraction peak widths become narrower as the annealing time increases, which may be attributed to grain growth.

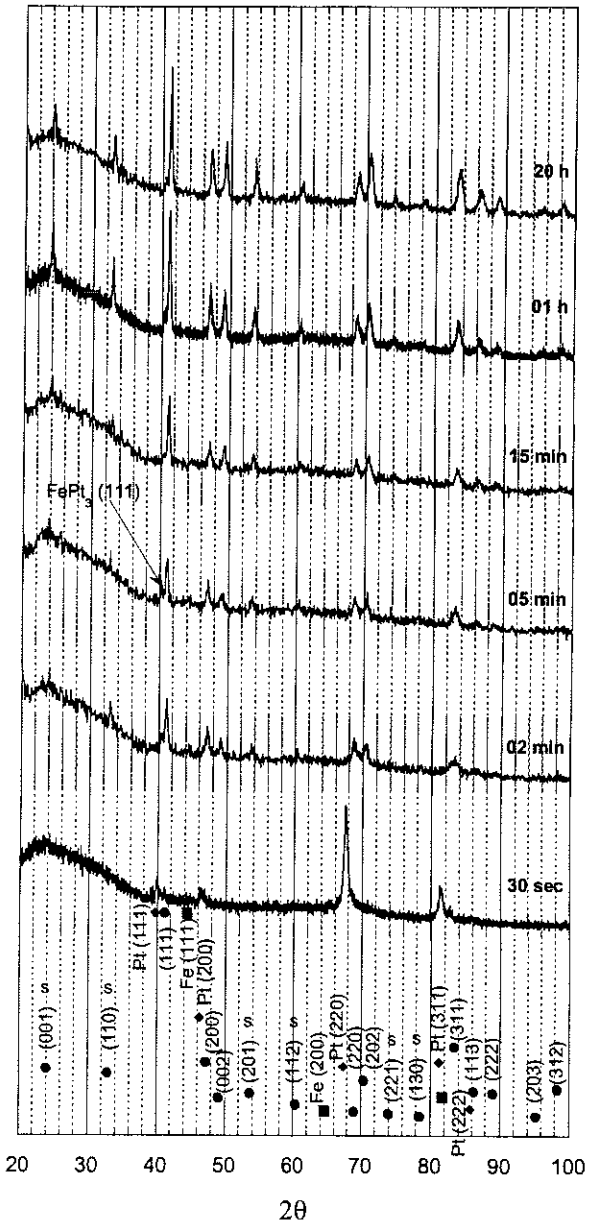

Figure 2.7: XRD patterns of the FePt sample annealed at 500 °C for 30 seconds – 20 hours. Power diffraction intensities for $L1_0$ FePt alloy represented by •. Superstructure reflections are denoted by the letter "s".

The appearance of superstructure reflections for annealing times as short as 2 minutes indicates the presence of ordered FePt. Detailed XRD patterns were collected for samples annealed at the slightly lower temperature of 450°C for times of 5 minutes, 15 minutes and 48

hours. The high angle section of these spectra, presented in figure 2.8, show only trace quantities of ordered fcc $FePt_3$ for annealing times of 5 and 15 minutes and none for the extended annealing time of 48 hours. There is no peak of the disordered fcc phase. This suggests that for the FePt and $FePt_3$ phases, ordering occurs almost immediately. The presence of Fe_3Pt phases is not ruled out. The order parameter S for the FePt phase of these annealed samples was estimated to be 0.86, 0.94 and 0.98, respectively (see annexe B). Lattice parameters $a \approx 3.86$ Å and $c/a \approx 0.96$ were estimated for all three samples, in agreement with literature values [3].

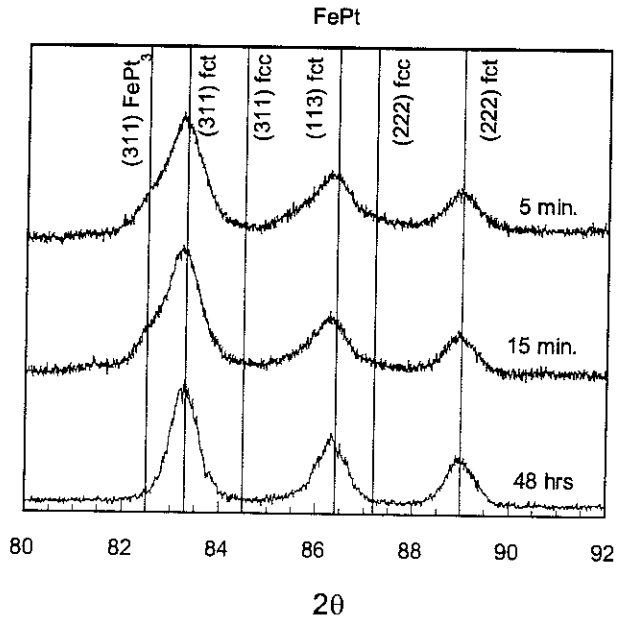

Figure 2.8: High angle section of the XRD spectra of the FePt foils (annealed at 450 °C). The vertical lines represent the 2θ positions of peaks belonging to the disordered fcc structure, taken from PDF file 29-0717, and those of the ordered fct FePt and $FePt_3$ structure.

The FePt/Ag series

XRD patterns of the FePt/Ag20 sample annealed at 450 °C for times of 2 min – 48 h is shown in figure 2.9. As for the Fe/Pt system, ordered FePt was formed for annealing times as short as 2 minutes. In addition, reflections of Ag and $FePt_3$ are also present. The relative intensities of the $FePt_3$ peaks ((001) and (111)) are stronger than for the Fe/Pt sample, indicating that diffusion/ordering to form FePt was slower in the Ag containing sample. The relative

intensity of these peaks reduces when t_a increases and disappears when t_a > 60 minutes. All diffraction peak widths become narrower as the annealing time increases.

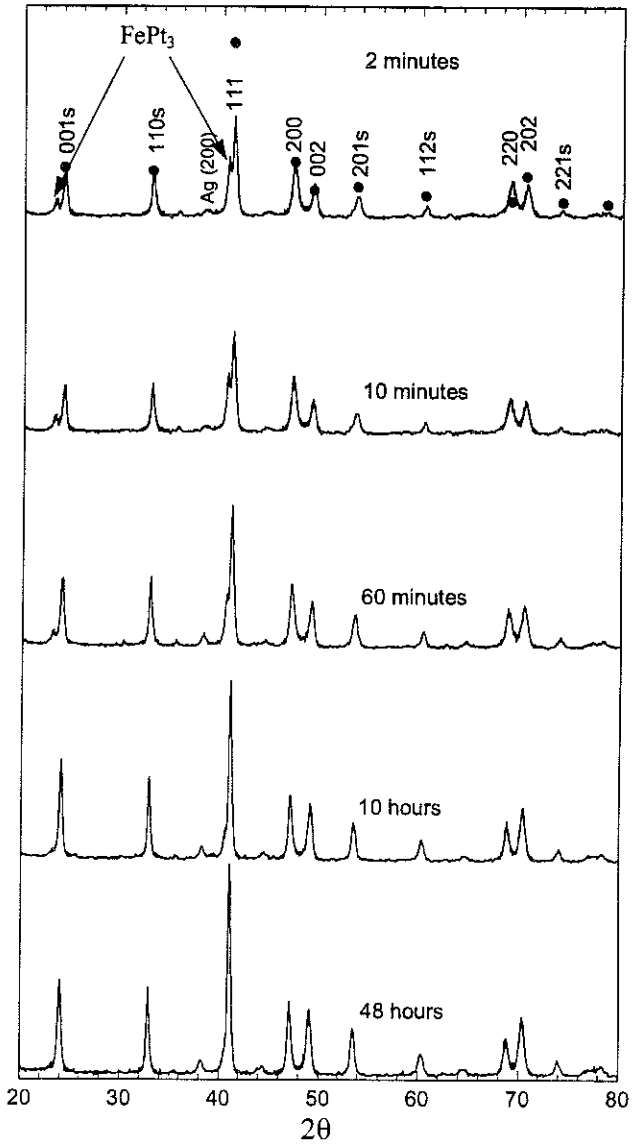

Figure 2.9: XRD patterns of the FePt/Ag sample annealed at 450 °C for 2 minutes – 48 hours. Power diffraction intensities for $L1_0$ FePt alloy represented by •, superstructure reflections are denoted by the letter "s".

The Fe-rich Fe/Pt and Pt-rich Fe/Pt series

Annealing conditions for the Fe-rich and Pt-rich samples were not as extensively varied as those for the Fe/Pt and Fe/Pt/Ag systems. Nevertheless, sections of the XRD spectra of representative samples of these systems, containing reflections of the secondary phase (Fe_3Pt

and $FePt_3$, respectively), are shown in figure 2.10. The presence of the (001) superstructure reflection of $FePt_3$ suggests that this phase is also ordered.

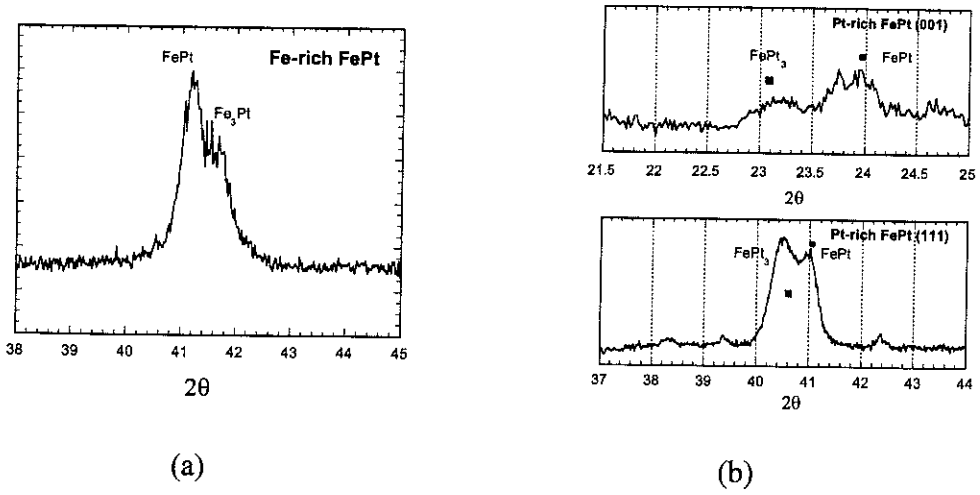

Figure 2.10: XRD patterns of (a) the fundamental (111) peaks of the FePt and Fe_3Pt phases in the Fe-rich FePt and (b) the superlattice (001) and fundamental (111) of the FePt and $FePt_3$ phases in the Pt-rich FePt.

Partial texture in annealed samples

XRD patterns of annealed samples of the five systems studied are shown in figure 2.11. All samples, except the Fe-rich Fe/Pt sample, were annealed at 450°C for 48h. In contrast, the Fe-rich Fe/Pt sample was annealed 450°C for just 1h (in this case annealing times were minimised to avoid grain-growth). Powder diffraction pattern intensities of $L1_0$ FePt (PDF file 43-1359) are included on all spectra. The relative intensities of the FePt peaks of all samples differ from those of the isotropic PDF intensities. This suggests that the samples have partial crystallographic texture. The relative intensities of the (001) and (002) peaks are significantly higher in the FePt and FePt/Ag systems, suggesting partial (001) out-of-foil texture in these systems. However, the texture was not strong enough to be clearly identified in rocking curves. The silver component of the FePt/Ag100 system remains (220) textured after annealing. <220> reflections of the Fe-rich and Pt-rich systems were stronger than expected for isotropic materials (namely the (202) and (220) reflections, respectively).

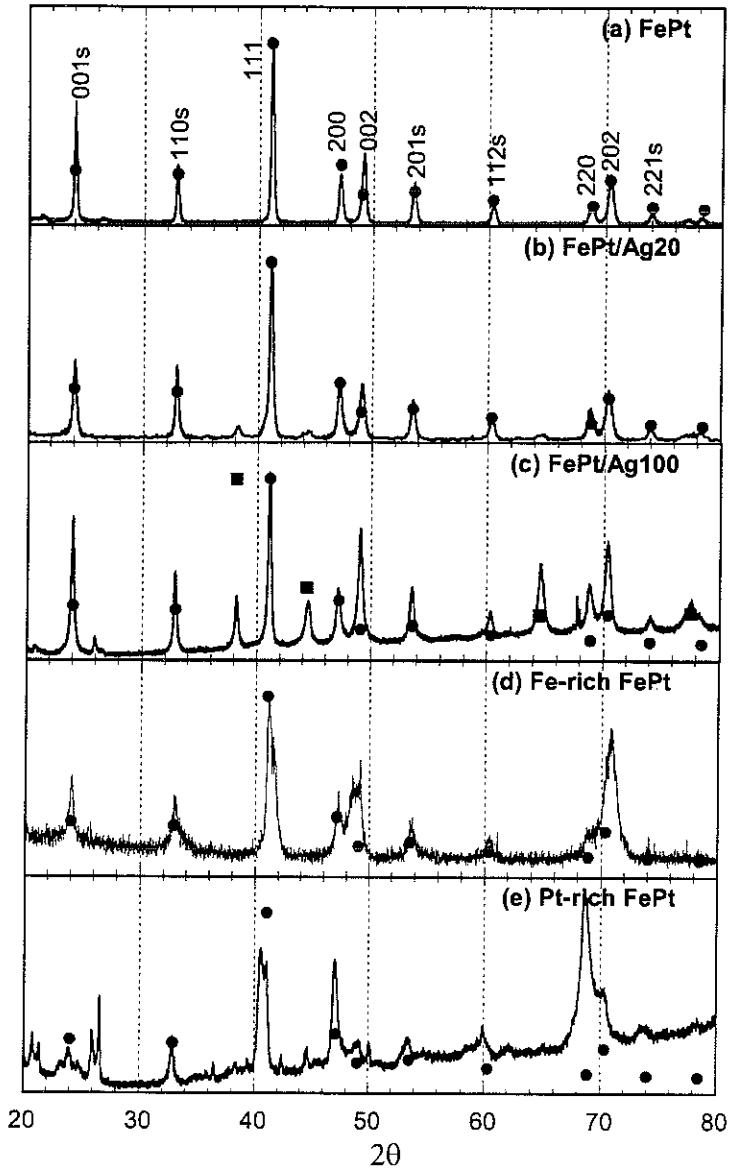

Figure 2.11: XRD pattern of (a) FePt foil produced by annealing Fe/Pt multilayer at 450 °C/48 h, the superstructure reflections of the $L1_0$ phase are denoted by the letter "s"; (b) FePt/Ag20 and (c) FePt/Ag100 foils produced by annealing Fe/Pt/Ag20 and Fe/Pt/Ag100 multilayer at 450 °C/48 h; (d) Fe-rich FePt foil produced by annealing Fe-rich Fe/Pt multilayer at 450 °C/1 h; (e) Pt-rich FePt foil produced by annealing Pt-rich Fe/Pt multilayer at 450 °C/48 h; (pdf intensities for $L1_0$ FePt and Ag represented by the solid circles and solid squares, respectively).

2.3.3. Electron microscopy imaging of annealed samples

A study of the microstructure of annealed samples is presently underway (in collaboration with IFW Dresden). Some preliminary but informative results are presented here. Images of the Fe/Pt sample annealed at 450°C for 15 minutes and 48 hours are shown in figure 2.12. The microstructure of the sample annealed for only 15 minutes is very inhomogeneous, with distinct composition modulation on the length scale of 1 μm. This suggests that diffusion is not complete after this annealing time. The longer annealed sample is also somewhat inhomogeneous with Pt rich and Fe rich phases present.

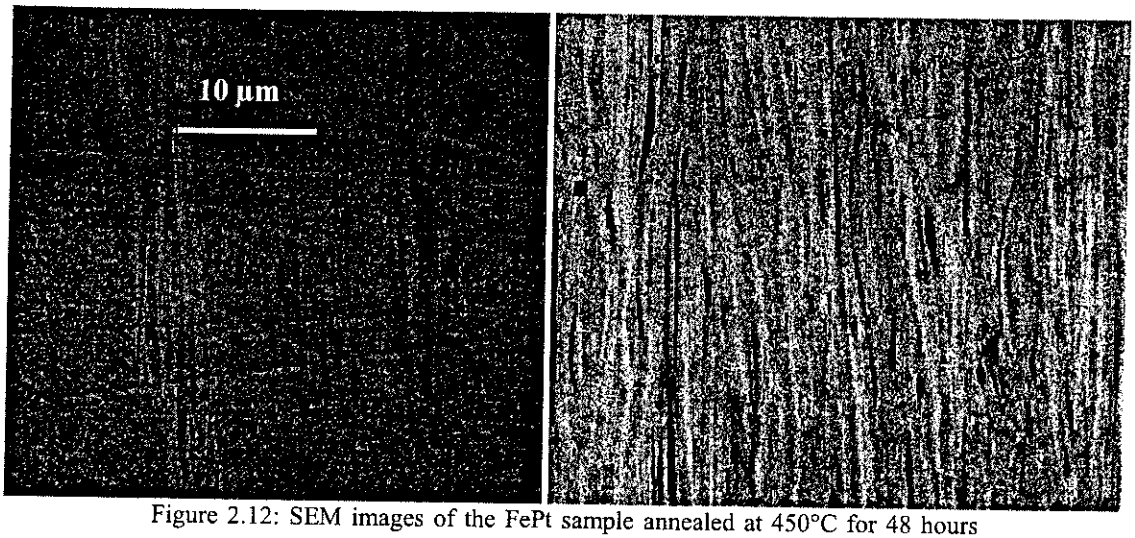

Figure 2.12: SEM images of the FePt sample annealed at 450°C for 48 hours and 15 minutes.

Some TEM analysis of the Fe/Pt sample annealed 450°C/48h, which showed optimum magnetic properties (see below) was carried out by M. Veron and M. Verdier of LTPCM, Grenoble. So far only plane-view TEM imaging has been possible. The TEM image revealed many interesting microstructural features. The in-plane dimensions of the FePt grains vary from tens of nm to some hundreds of nm (figure 2.13.a). The inset of figure 2.13 is the diffraction pattern of a larger area. Diffraction patterns taken on individual grains reveal superstructure reflections, confirming that the FePt is ordered (figure 2.13.b). A band-like structure, with bandwidths of the order of 10 nm, is observed in many grains. Diffraction analysis of an area of a large grain containing these bands (inset figure 2.13.b) reveals that the area had single crystalline structure, *i.e.* these bands are not twins, and that the bands are roughly perpendicular to a <220> direction. (111)<112> twinning is observed in the diffraction pattern of another area of this grain, in which the orientation of the bands changes

along linear fronts (figure 2.13b). This band structure is not well understood and may simply be due to heavy faulting. However, the fact that the bands are perpendicular to a <220> direction, a direction along which Fe and Pt atoms form alternate layers in the ordered fct FePt structure, may suggest that the bands are related to an anti-phase-domain structure. Moiré patterning and boundary traces due to the superposition of grains are also clearly visible (cross-sectional).

Sample preparation for cross-sectional TEM imaging was unsuccessful. However a cross-sectional SEM image was obtained at IMF, Dresden, Germany, and it is present in figure 2.13.c. The grains dimensions are of order of some of hundreds of nm which are comparable to those revealed from the in-plan TEM image. This suggests that the grain dimensions are equiaxial in in-plan and out-of-plan view. But there is a visible trace of layer structure which produce an structure anisotropy in the side-view direction.

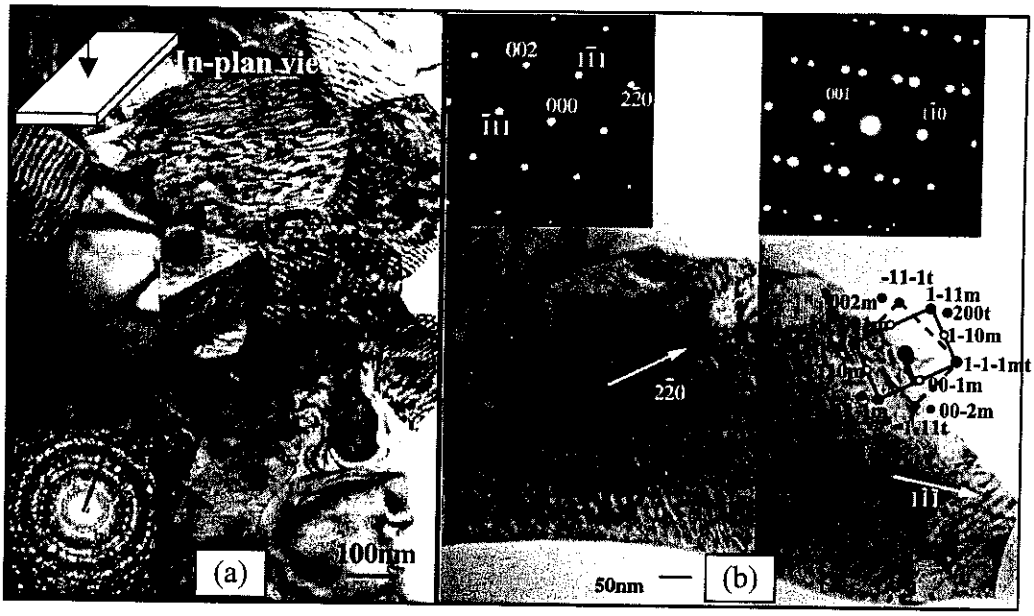

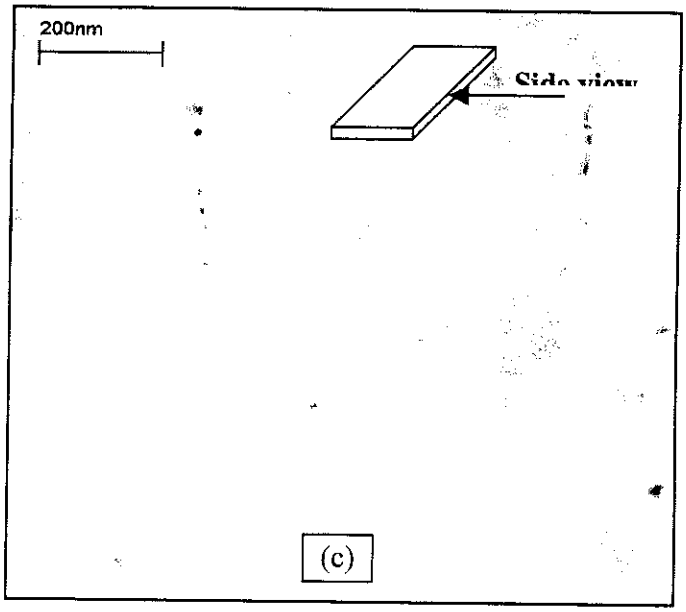

Figure 2.13: (a) Plane-view TEM image and diffraction pattern of a section of an FePt foil (optimally annealed - 450°C/48h), containing a number of grains with in-plane dimensions in the range 100-300 nm. (b) one large grain of an FePt foil, displaying a band structure. The diffraction pattern of the left-hand-side of the grain is characteristic of a single crystalline structure (top left inset) while that of the right-hand-side is characteristic of a twinned structure (top right inset). The sketch of this twin (t) and matrix diffraction (m) is shown in this image. (c) Side-view SEM image of the same sample. The grain size is of order of some hundreds of nm. A trace of layer structure is visible.

2.4. Magnetic characterisation of annealed samples

2.4.1. The FePt series

As discussed in section 2.3.1, the multilayer Fe/Pt sample was annealed at 500 °C for annealing time 30 sec – 20 h (XRD patterns were given in figure 2.7). Some representative demagnetisation curves from this series are shown in figure 2.14.a. The hysteresis loop of the sample annealed for t_a = 30 seconds is comparable to that of the as-rolled sample. The two-phase loop behaviour observed for t_a = 2 and 15 minutes shows the co-existence of magnetically hard and soft phases, indicating that diffusion and/or ordering is incomplete.

Annealing temperature dependence, in the range 300-700°C, was then studied for a fixed annealing time of 60 minutes (figure 2.14.b). For T_a = 300 °C, the loop is comparable to the as-rolled sample, indicating that this temperature is too low to allow any significant diffusion. Two-phase loop behaviour was observed for t_a = 350 °C, indicating that diffusion has begun but diffusion or ordering is incomplete. When t_a > 350 °C, M(H) curve show single phase behaviour with coercivity values in the range 0.7 – 0.8 T.

The influence of both temperature and time on the coercivity achieved in FePt samples is given in figure 2.15. Once the temperature (time) is high (long) enough to allow diffusion, typical coercivities of 0.7 – 0.8 T are achieved. Slight increases in the value of coercivity were achieved by extending the annealing time. The highest value of coercivity was measured on a sample annealed at 450°C for 48h.

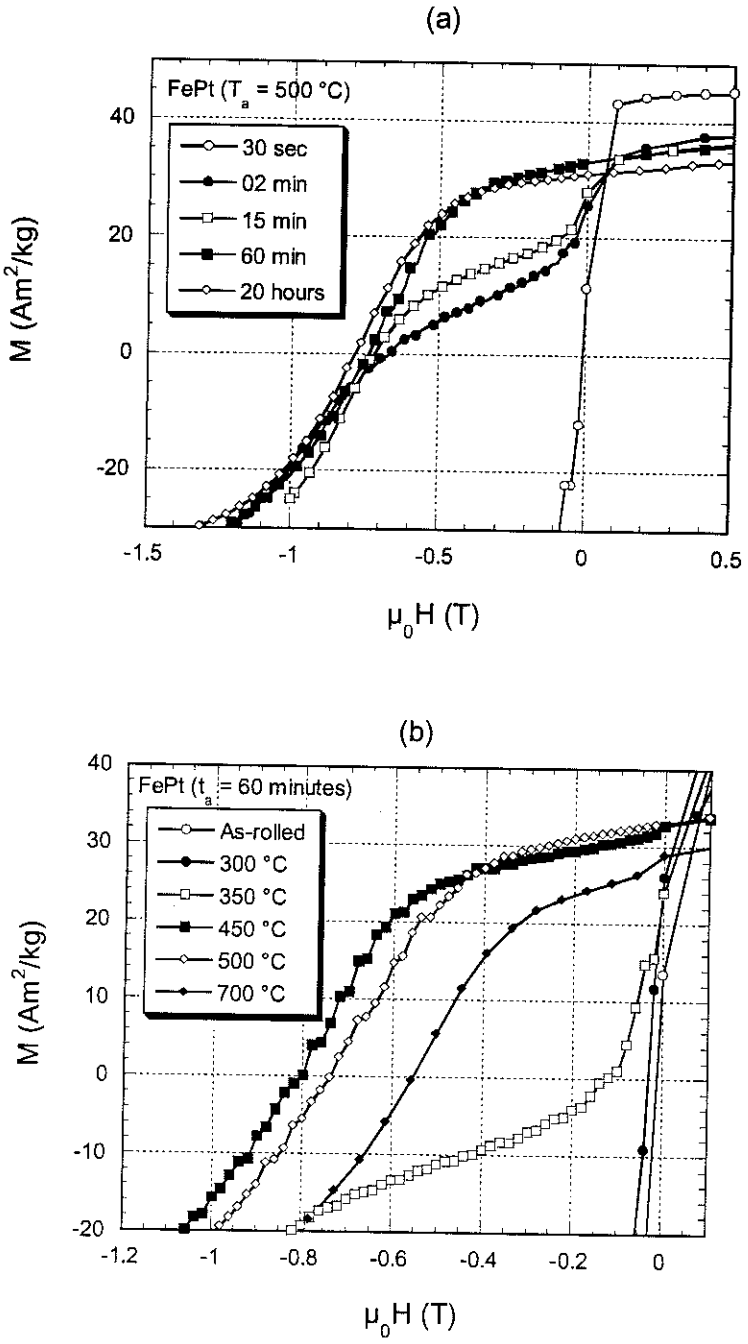

Figure 2.14: Some representative demagnetisation curves of the FePt sample (a) annealed at 500 °C for different times and (b) annealed for 1 hour at different temperatures.

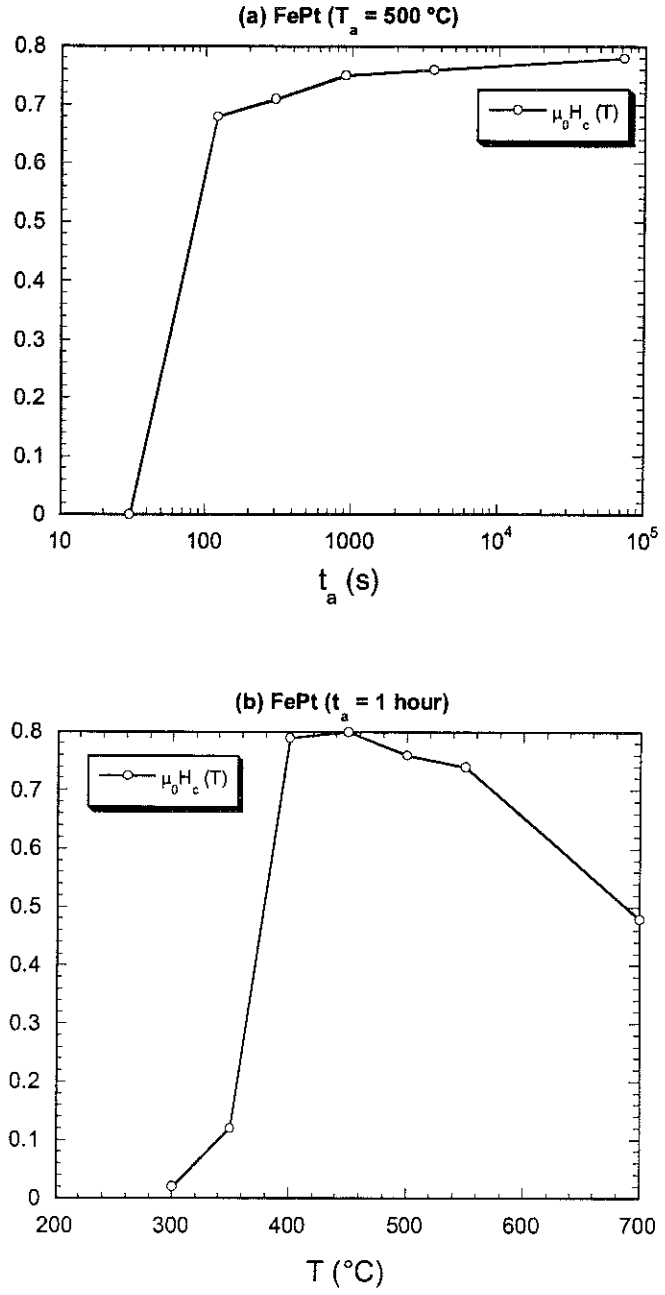

Figure 2.15: The influence of (a) the annealing time and (b) the annealing temperature on the coercivity achieved in FePt samples.

Optimally annealed FePt

All magnetisation measurements presented so far were made in-plane (IP), *i.e.*, the applied field H was parallel to the rolling plane. Room temperature hysteresis loops of the optimally annealed FePt foil (450°C/48h), measured in three orthogonal directions in an extraction magnetometer, are shown in figure 2.16. Sample dimensions are typically of order of 0.1×3×3 mm. The loops measured in the foil plane (IP) are identical to each other but quite different to the perpendicular-to-plane (PP) loop. The coercivity of the IP loop ($\mu_0 H_c^{IP}$ = 0.76 T) is higher, by 12%, than that of the PP loop ($\mu_0 H_c^{PP}$ = 0.66 T). The corrected PP loop, assuming a demagnetising correction factor $N = 1$ (chosen because of the foil shape), is also shown. The appropriateness of this value is discussed in chapter 4. The PP remanence is about 15 % higher than the IP remanence. This may be attributed to partial (001) out of plane texture in these foils – as already suggested by XRD data (figure 2.11.a).

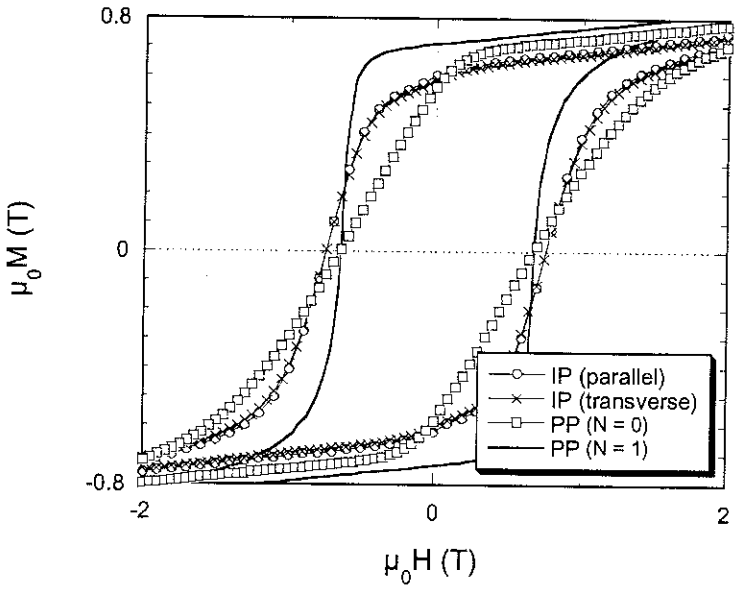

Figure 2.16: Room temperature magnetization loops of FePt foil when the applied field is in-plane IP parallel to rolling direction (open circles), IP transverse to rolling direction (x), perpendicular-to-plane PP (open squares) and corrected PP (demagnetising correction $N = 1$).

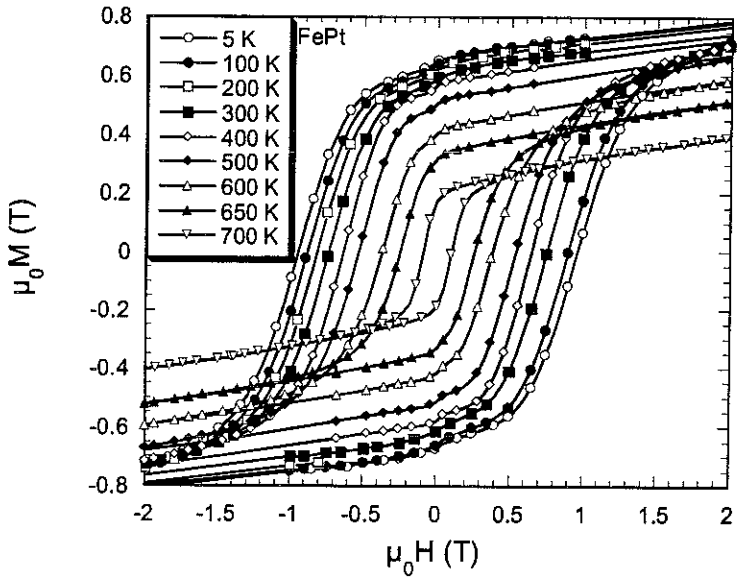

Figure 2.17: In-plane hysteresis curves of optimally annealed FePt (450°C/48h) measured at different temperatures. The maximum applied field for the low temperature measurements ($T \leq 300$ K) and high temperature measurements (300 K $< T \leq 700$ K) are 10 T and 7 T, respectively.

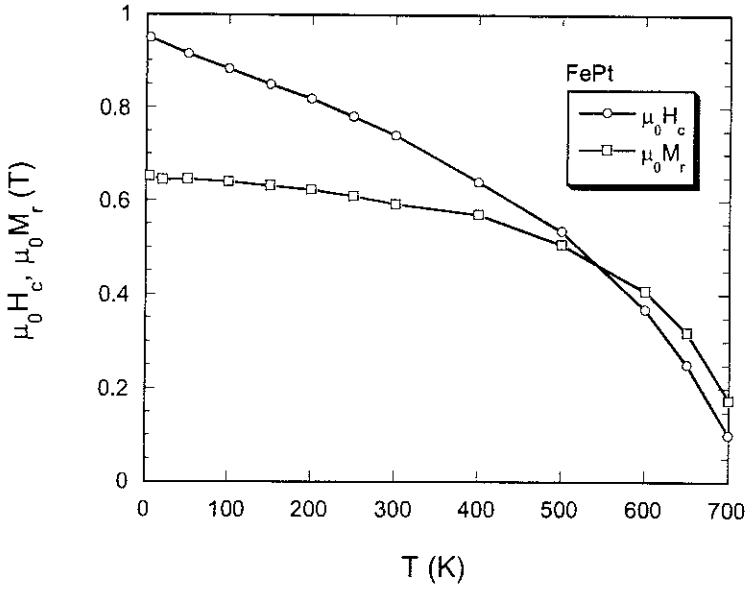

Figure 2.18: Temperature dependence of the in-plane coercive field and remanence of the optimally heat treated (450 °C/48 hours) FePt.

Figure 2.17 shows the in-plane hysteresis loops of the optimally annealed (450°C/48h) FePt sample in the temperature range 4 – 700 K, measured in an extraction magnetometer. The maximum applied field for the low temperature measurements ($T \leq 300$ K) and high temperature measurements (300 K < $T \leq 700$ K) are 10 T and 7 T, respectively. A very slight low-field dip is observed for T < 500 K. Magnetisation is not saturated in even the highest applied field, which may be attributed to the high anisotropy of this alloy [26]. The necessary field for saturation of the FePt sample is estimated to be about 12 – 15 T. The temperature dependence of the coercive field and remanent magnetisation is plotted in figure 2.18. A monotonous decrease with increasing temperature is observed in both curves. The decrease with temperature of the coercivity is relatively faster than that of the remanence. At room temperature, the remanent magnetization is 0.58 T and the coercivity is 0.74 T. At 600 K these values are 0.42 T and 0.37 T, respectively. The estimated value of the energy product decreased from 100 kJm^{-3} at room temperature to 25 kJm^{-3} at 600 K. No decrease in room temperature coercivity was detected following repeated high temperature measurements up to 700 K. This indicates that the microstructure is stable up to this temperature, which is very important if these foils are to be used in high temperature applications.

2.4.2. The FePt/Ag series

The influence of the temperature of annealing on the magnetic properties of the FePt/Ag20 sample (figure 2.19) was found to be very similar to that of the Fe/Pt system (figure 2.15.b). In figure 2.20, we show the temperature dependence of the in-plane coercive field of the optimally heat treated (450 °C/48 hours) FePt, FePt/Ag20 and FePt/Ag100 samples. It is seen that the addition of Ag had the desired effect of increasing the coercivity, though at the expense of magnetisation owing to dilution. The highest coercivity values of 1.08 T and 1.35 T were obtained for the FePt/Ag100 sample at 300 and 4 K, respectively.

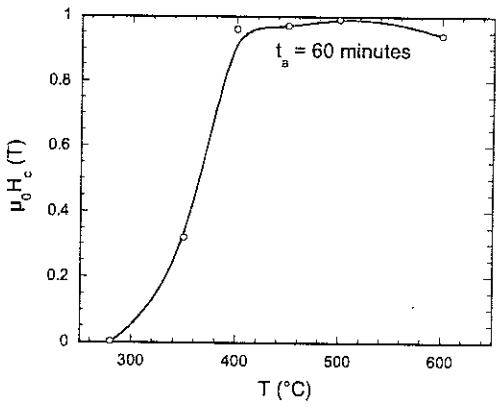

Figure 2.19: Influence of the annealing temperature on the coercivity achieved in the FePt/Ag20 samples.

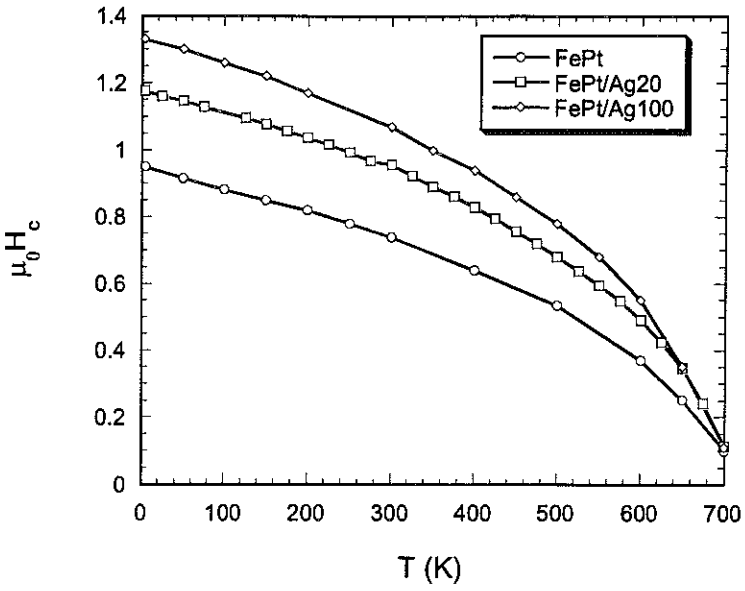

Figure 2.20: Temperature dependence of the in-plane coercive field of the optimally heat treated (450 °C/48 hours) FePt, FePt/Ag20 and FePt/Ag100 samples.

2.4.3. The Fe-rich FePt series

Figure 2.21.a shows room temperature in-plane hysteresis loops of the Fe-rich FePt sample annealed at temperatures in the range 300 °C – 700 °C for 1 hour. The expected fraction of the FePt and Fe_3Pt phases in this foil is 65 vol % and 35 vol %, respectively. Two-phase loop behaviour (hard/soft) is observed for all samples annealed at or above 400°C (below this temperature the loop is comparable to as-rolled foils), indicating the absence of exchange coupling between the hard and soft phases. The coercivity of the hard phase can be deduced from the derivative of magnetisation, when it is defined by $H_c = dM/dH\big|_{max}$ [27]. This definition of coercivity is particularly relevant to such a two-phase system. Figure 2.21.b gives the temperature dependence of the coercive field of the hard phase. The highest coercivity is of the order of $\mu_0 H_c \approx 0.6$ T (T_a = 400, 450 °C). Out of plane magnetisation measurements carried out on the sample will be discussed in chapter 4.

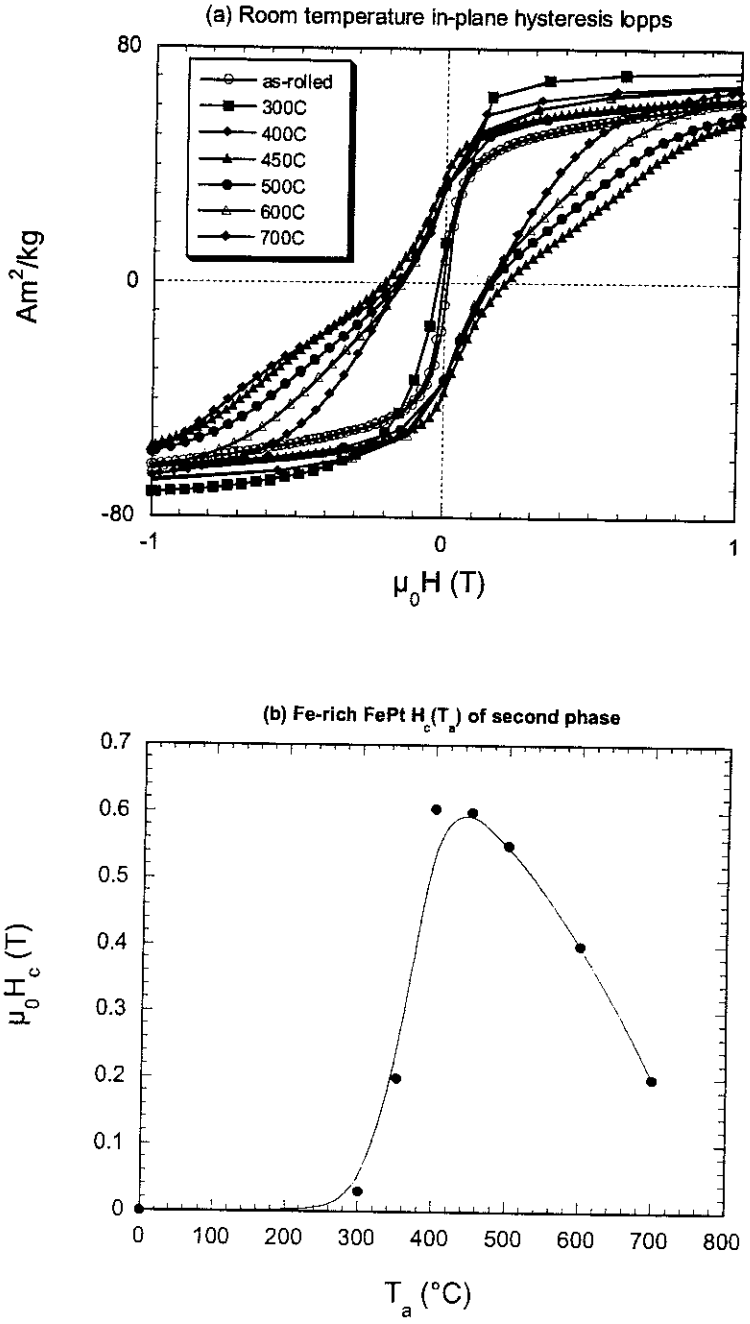

Figure 2.21: (a) Room temperature in-plane hysteresis loops of the Fe-rich FePt sample annealed at temperatures in the range 300 °C – 700 °C for 1 hour; (b) Influence of the annealing temperature on the coercivity of the hard phase taken from the maximum of the derivative curves (see chapter 4).

2.4.4. The Pt-rich FePt series

Figure 2.22.a shows the hysteresis loops of the Pt-rich FePt sample, annealed 450°C/48 h and measured in the range 4 K – 300 K. The expected fraction for the $FePt_3$ and FePt in this foil is 33 vol % and 67 vol %, respectively. No significant field axis shift (exchange bias) is observed on any of the hysteresis loops. The 300 K loop shows single phase behaviour while two-phase behaviour is observed at lower temperatures. This indicates that the $FePt_3$ formed is ferromagnetic almost up to room temperature. This result was also revealed for the composition around $FePt_3$ [11]. The shape of the two-phase loops is significantly different than that of the Fe_3Pt/FePt system - there is no low field dip in the $FePt_3$/FePt loops, suggesting that the secondary phase is also somewhat coercive. This is confirmed by re-coil curves, which probe reversibility in magnetisation processes in low fields (figure 2.22.b).

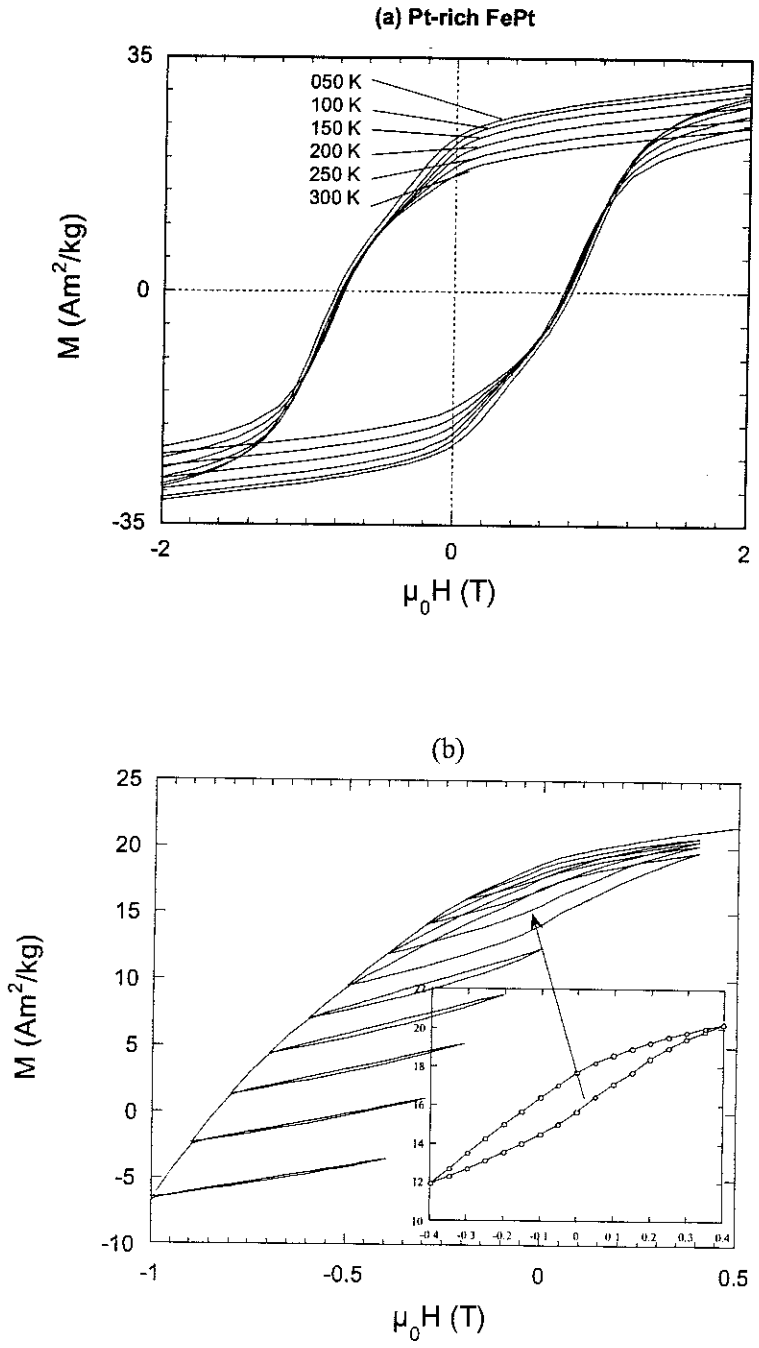

Figure 2.22: (a) Hysteresis loops of the Pt-rich FePt sample, annealed 450°C/48 h and measured in the range 4 K – 300 K, (b) Recoil loops at 50 K indicate that the second ferromagnetic phase is coercive.

2.5. Discussion

Magnetisation reversal and thus coercivity in polycrystalline samples should be determined by both intrinsic properties (for example H_A), which depend on the phase composition and its degree of long range order, as well as extrinsic microstructural parameters such as *grain size*, *grain morphology*, *antiphase boundary density* and *twin structure*. Unfortunately we do not have enough microstructural data on our foils to elucidate the influence of the details of our particular microstructure on magnetisation reversal in the foils. Nevertheless, we can make some tentative suggestions to explain our results.

Firstly it should be noted that the values of coercivity achieved in our FePt foils are significantly higher than the values reported for bulk samples ($\mu_0 H_c < 0.5$ T) and comparable to the typical values reported for thin film samples ($\mu_0 H_c \approx 1$ T). In a general way, the higher value of coercivity in thin films compared to bulk samples may be attributed to a better control of the microstructure, particularly the grain size, in the former. Why are our samples more coercive than the classically processed bulk samples? A significant factor to consider is the annealing temperature at which the $L1_0$ phase is formed. In the classical bulk route, the $L1_0$ phase is formed by annealing a homogenised disordered precursor (fcc FePt). In our case, the high anisotropy phase is formed by annealing a multilayer precursor (Fe/Pt). Whereas annealing temperatures of 600°C and higher are needed to form the ordered phase in bulk samples, we can form the phase at temperatures as low as 400°C. In the former case, the atoms only have to re-arrange themselves, no long-range diffusion is required, while in the latter case atoms have to diffuse over distances of up to tens of nanometers. However, concentration gradients, which are the driving force for diffusion, are very different in each case. Thus the strong concentration gradient in the multilayer samples accounts for the onset of diffusion at lower temperatures than in the homogenised samples. What is more, XRD data clearly show that ordering into the fct $L1_0$ phase occurs almost immediately (section 2.3.2). How should this influence the coercivity? The degree of order in the $L1_0$ phase should depend on the processing temperature, and indeed the lower the temperature, the higher the expected order (the ordered phase is the low temperature phase while the disordered phase is the high temperature phase). The anisotropy of the phase is related to the degree of order, the higher the order the higher the anisotropy, and thus the higher the coercivity. The estimated values of the order parameter in our foils are very high ($S > 0.8$), comparable to values reported for high quality thin film samples [3]. Of course the processing temperature should also affect the

grain size and the direction of the concentration modulation (c-axis) of the FePt phase, and this in turn can affect the coercivity. Nevertheless, the above argument may qualitatively explain the higher value of coercivity compared with classically prepared bulk samples. The additional role of the grain morphology (in our case assumed to be platelet-like) in influencing the coercivity is analysed in chapter 4. Microstructural features can play a significant role in magnetisation reversal by pinning the domain walls. A virgin magnetisation curve at 4K of the optimally heat treated FePt sample is shown in figure 2.23. The curve is not characteristic of either classical nucleation (very high initial susceptibility) or classical pinning (very low initial susceptibility) systems. Detailed microstructural analysis is required to identify the actual coercivity mechanism at play. The temperature dependence of coercivity in this sample is analysed within the framework of the micro-magnetic and global models in Chapter 4.

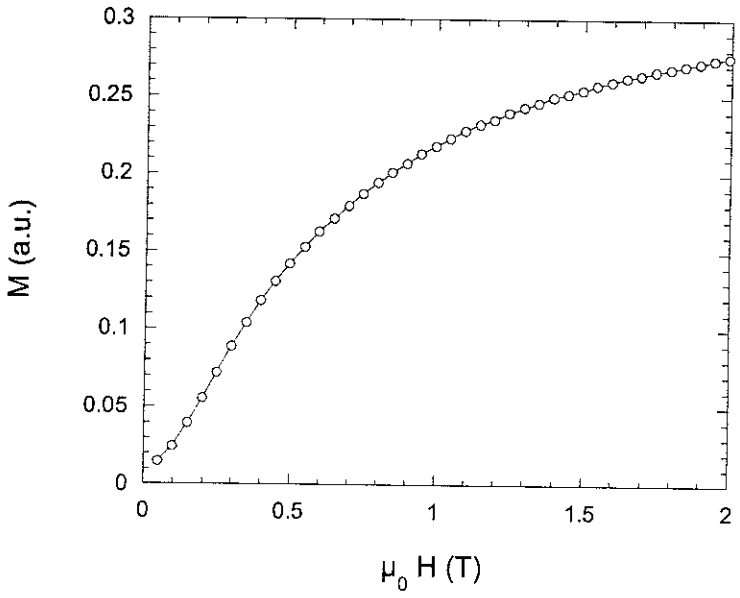

Figure 2.23: Virgin magnetisation curve of the FePt sample at 4K.

2.6. Conclusions

Hard magnetic foils of FePt have been prepared by severe deformation followed by annealing of bulk Fe/Pt multilayers. The relatively high coercivity values achieved are attributed to the high degree of order of the $L1_0$ phase formed and to the particular microstructure produced by this novel route. The coercivity was further increased by introducing a non-magnetic (Ag) component. This increase is believed to have two origins, firstly, the presence of Ag aids the deformation of the multilayer and the sample can be deformed to a greater extent; secondly, the Ag acts to magnetically isolate the coercive FePt grains. The higher the Ag content, the greater both effects. Of course the increase in coercivity comes at the expense of volume magnetisation due to a dilution of the magnetic phase. Attempts to prepare FePt/Fe_3Pt "spring magnets" were unsuccessful as the hard and soft phases produced were not exchange-coupled (presumably the soft grains are too large). However, interesting features in the magnetic behaviour of these samples are discussed in terms of "dipolar- coupling" in Chapter 4. Attempts to prepare FePt/$FePt_3$ "exchange biased" systems were also unsuccessful. In this case the Pt-rich phase formed was not anti-ferromagnetic as hoped for, but ferromagnetic. Nevertheless, the possibility to prepare composite materials comprised of intermetallic phases by deformation/annealing has been demonstrated. For this technique to be of interest for these types of systems the dimensions of the different phases must be reduced to the nanometer scale.

References

1. Coffey, K.R., M.A. Parker, and J.K. Howard, *High anisotropy $L1_0$ thin films for longitudial recording.* IEEE Trans. Magn., **31** (1995) 2737.
2. Liu, J.P., C.P. Luo, Y. Liu, and D.J. Sellmyer, *High energy products in rapidly annealed nanoscale Fe/Pt multilayers.* Appl. Phys. Lett., **72** (1998) 483.
3. Cebollada, A., R.F.C. Farrow, and M.F. Toney, *Structure and Magnetic Properties of Chemically Ordered Magnetic Binary Alloys in Thin Film Form,* in *Magnetic Nanostructure*, H.S. Nalwa, Editor. (2002), American Scientific Publishers. p. 93.
4. Kubaschewski, O., *Fe-Pt binary phase diagram,* in *Iron-binary phase diagrams.* (1982), Springer-Verlag. p. 91.
5. Krivoglaz, M.A. and A. Smirnov, *The theory of order-disorder in alloys.* (1964), London: Macdonald.
6. Warren, B.E., *X-ray diffraction.* 1 ed. (1969), Massachusetts: Addison-Wesley Publishing Company. 381.
7. Cugat, O. in *Proceedings of INTERMAG.* (2003). (to appear).
8. Watanabe, K., *Crystal structures and permanent magnet properties in Fe-Pt alloys.* J. Japan Inst. Metals, **51** (1987) 91.
9. Watanabe, K. and H. Masumoto, *The effect of various elements on properties of Fe-Pt permanent magnets having high energy product.* J. Japan Inst. Metals, **48** (1984) 930.
10. Xiao, Q.I., P.D. Thang, E. Brück, F.R. de Boer, and K.H.J. Buschow, *Effect of phase transformation on remanence enhancement in bulk Fe–Pt magnets.* Appl. Phys. Lett., **78** (2001) 3672.
11. Bacon, G.E. and J. Grangle, *Chemical and magnetic order in platinum-rich Pt+Fe alloys.* Procedding of Royal Society of London, **A 272** (1963) 387.
12. Farrow, R.F.C., D. Weller, R.F. Marks, M.F. Toney, S. Hom, G.R. Harp, and A. Cebollada, *Growth temperature dependence of long-range alloy order and magnetic properties of epitaxial Fe_xPt_{1-x} (x~0.5) films.* Appl. Phys. Lett., **69** (1996) 1166.
13. Bian, B., K. Sato, Y. Hirotsu, and A. Makino, *Ordering of island-like FePt crystallites with orientations.* Appl. Phys. Lett., **75** (1999) 3686.
14. Cebollada, A., D. Weller, J. Sticht, G.R. Harp, R.F.C. Farrow, R.F. Marks, R. Savoy, and J.C. Scott, *Enhanced magneto-optical Kerr effect in spontaneously ordered FePt alloys: Quantitative agreement between theory and experiment.* Phys. Rev. B, **50** (1994) 3419.
15. Yang, T., E. Ahmad, and T. Suzuki, *FePt–Ag nanocomposite film with perpendicular magnetic anisotropy.* J. Appl. Phys., **91** (2002) 6860.
16. Liu, J.P., Y. Liu, C.P. Luo, Z.S. Shan, and D.J. Sellmyer, *Magnetic hardening in FePt nanostructured films.* J. Appl. Phys., **81** (1997) 5644.
17. Farrow, R.F.C., D. Weller, R.F. Marks, M.F. Toney, A. Cebollada, and G.R. Harp, *Control of the axis of chemical ordering and magnetic anisotropy in epitaxial FePt films.* J. Appl. Phys., **79** (1996) 5967.

18. Shima, T., K. Takanashi, Y.K. Takahashi, and K. Hono, *Preparation and magnetic properties of highly coercive FePt films.* Appl. Phys. Lett., **81** (2002) 1050.

19. Christodoulides, J.A., Y. Huang, Y. Zhang, G.C. Hadjipanayis, I. Panagiotopoulos, and D. Niarchos, *CoPt and FePt thin films for high density recording media.* J. Appl. Phys., **87** (2000) 6938.

20. Huang, Y.H., H. Okumura, G.C. Hadjipanayis, and D. Weller, *CoPt and FePt nanowires by electrodeposition.* J. Appl. Phys., **91** (2002) 6869.

21. Sun, S., C.B. Murray, D. Weller, L. Folks, and A. Moser, *Monodisperse FePt nanoparticles and ferromagnetic FePt nanocrystal superlattices.* Science, **287** (2000) 1989.

22. Zeng, H., J. Li, J.P. Liu, Z.L. Wang, and S. Sun, *Exchange-coupled nanocomposite magnets by nanoparticle self-assembly.* Nature, **420** (2002) 395.

23. Kneller, E.F. and R. Hawig, *The exchange-spring magnet: a new material principle for permanent magnets.* IEEE Trans. Magn., **27** (1991) 3588.

24. Meiklejohn, W.H. and C.P. Bean, *New Magnetic Anisotropy.* Phys. Rev., **102** (1956) 1413.

25. Honeycombe, R.W.K., *The Plastic Deformation of Metals.* (1968): Edward Ltd. p. 325.

26. Daalderop, G.H.O., P.J. Kelly, and M.F.H. Schuurmans, *Magnetocrystalline anisotropy and orbital moments in transition-metal compounds.* Phys. Rev. B, **44** (1991) 12054.

27. Givord, D. and M.F. Rossignol, *Coercivity*, in *Rare-earth ion permanent magnets*, J.M.D. Coey, Editor. (1996), Clarendon Press: Oxford. p. 218.

Chapter 3: Exchange interactions in nanocomposite systems

Résumé en Français

Chapitre 3 : Interactions d'échange dans les systèmes nanocomposites

Nous nous intéressons dans ce chapitre à la modélisation théorique des interactions d'échange à travers une interface et leur effet sur les propriétés magnétiques intrinsèques (aimantation et anisotropie), à température finie, de matériaux ferromagnétiques ou ferrimagnétiques.

Notre intérêt étant de préparer des nanomatériaux ferromagnétiques par déformation à froid, nous avons décidé d'étudier les propriétés attendues de tels systèmes dans une approche de type champ moléculaire. Nous avons examiné les propriétés de deux matériaux ferromagnétiques présentant des aimantations et températures de Curie différentes, couplés à travers leurs interfaces. Un modèle simple a d'abord été développé dans une approche à une dimension (1D), il a ensuite été extrapolé à trois dimensions (3D). Nous avons calculé plus spécifiquement les variations thermiques de l'aimantation et de l'anisotropie de systèmes de moments localisés. Nous avons étendu cette analyse aux systèmes de type terres rares (R) – métaux de transition (T), dans lesquels de fortes interactions d'échange lient entre eux les moments T ainsi qu'avec les moments R, et de très fortes anisotropies résultent du couplage des moments R avec le réseau. Cette analyse nous a permis d'élaborer un modèle de comportement des matériaux nanocomposites doux/durs.

Les résultats de nos analyses montrent que les propriétés magnétiques intrinsèques des phases constitutives de systèmes nanostructurés diffèrent de celles observées à l'état massif et que cet effet résulte du couplage d'échange à travers les interfaces. De façon générale, la valeur de l'aimantation est relativement plus affectée que celle de l'anisotropie. A l'interface entre deux matériaux ferromagnétiques dont les températures de Curie sont dans le rapport de 1 : 2 (ceci correspond par exemple au cas du système $Y_2Fe_{14}B/Fe$), une aimantation induite, qui peut atteindre jusqu'à 50 % de la valeur de l'aimantation à saturation absolue, est calculée à une température égale à la température de Curie du matériau de plus bas, T_c. Dans les composés R-T, l'aimantation et l'anisotropie induites sur le site T sont supérieures à celles induites sur

le site R. Pour des systèmes connus ($SmCo_5$, $Nd_2Fe_{14}B$), l'aimantation d'interface induite sur les atomes R ne dépasse jamais 10% de la valeur maximale à 0K et l'anisotropie induite ne dépasse pas 1% de cette valeur maximale.

On peut penser que la modification des propriétés magnétiques intrinsèques pourrait en retour influer sur les processus d'aimantation observés dans ces systèmes. De tels effets sont les plus importants lorsque l'épaisseur des domaines magnétiques, qui définit le volume dit d'activation au sein duquel le renversement d'aimantation est initié, atteint quelques distances interatomiques et correspond donc aux valeurs typiques des épaisseurs sur lesquelles les propriétés magnétiques intrinsèques sont affectées par le couplage interfacial. De telles épaisseurs de domaines sont caractéristiques des composés R-T riches en métal T. Or, dans ces systèmes, l'aimantation et l'anisotropie, à température ambiante, ne sont pas significativement affectées par le couplage. A plus haute température, lorsque la valeur de l'aimantation induite devient significative, l'anisotropie est très faible de toute façon. Ainsi, la modification des propriétés magnétiques intrinsèques, résultant du couplage d'échange à travers les interfaces, ne doit pas modifier profondément les processus de renversement d'aimantation.

Notons que les propriétés de matériaux nanocomposites discutées dans ce chapitre sont celles attendues des matériaux terres rares – métaux de transition. Nous n'avons pas abordé l'analyse expérimentale de ces systèmes. En effet, nous avons montré que leur préparation par déformation mécanique soulève de grandes difficultés techniques. C'est pourquoi, nous nous sommes tournés vers le système Fe-Pt. Nous nous sommes heurtés pour ceux-ci à d'autres difficultés et nous n'avons pas réussi à préparer de véritables nanocomposites. C'est pourquoi, en fin de compte, les analyses présentées dans ce chapitre n'ont pu être appliquées à des systèmes réels.

Chapter 3: Exchange interactions in nanocomposite systems

In this chapter, we study theoretically the effect of exchange interactions across interfaces on finite temperature intrinsic magnetic properties such as magnetisation and anisotropy in nanocomposites.

3.1. Introduction

The magnetic properties of a homogeneous material can essentially be described with the help of four main parameters: the 0 K magnetisation, the magnetocrystalline anisotropy, the molecular field coefficient and the Curie temperature.

In systems formed by mixing magnetic particles with different magnetic properties, the rule of mixing should apply to the extent that the interactions between the components can be neglected. It is very rare that this is the case since long-range dipolar interactions are present, which affect magnetisation processes. However, from the point of view of exchange and anisotropy, particles can be considered as decoupled as long as their dimensions are larger than about 100 nm. This is because exchange and anisotropy are short-range interactions. Their influence is manifest over distances of the order of the exchange length or of the domain wall width. Neither exceeds around 20 nm, which is very much smaller than typical particle sizes (obviously, this argument does not apply to assembly of nanoparticles). In an alloy of composition $Nd_4Fe_{78}B_{18}$, Coehoorn et. al. discovered in 1988 that magnetisation reversal occurred through a more or less homogeneous process within the entire sample, although the material was heterogeneously formed $Nd_2Fe_{14}B/Fe_3B$ [1]. This was explained by E. F. Kneller and R. Hawig and attributed to the exchange coupling between the constituent grains [2]. To schematically described reversal, let us assume initially that hard and soft grains magnetisation is saturated. Under applied field of opposite direction to the initial magnetisation direction, reversal of the soft grains requires the formation of a domain wall at the interface with the hard grain. Due to the very small size of the soft grain, such a domain wall necessarily has a much smaller thickness than its equilibrium value. It has thus higher

energy. The creation of such a domain wall requires an applied field whose strength is a significant fraction of the hard phase anisotropy field H_A. Above the applied field at which soft phase reversal begins and before the hard phase reversal, the magnetisation variation varies reversibly with the applied magnetic field, hence the expression exchange spring to designate these materials. In such nanocomposites, it is intuitive that exchange interaction at the interface should also affect intrinsic magnetic properties such as magnetisation or anisotropy. This effect, however, have almost not been considered in the literature. To our knowledge, only the coupling of two different anti-ferromagnetic materials in superlattice has been examined by A. S. Carrico and R.E. Camley [3]. The temperature dependence of the magnetisation was found to depend strongly on the layer individual thickness and on the strength of the interface exchange coupling. Similarly, R. W. Wang and D. L. Mills examined an Ising anti-ferromagnetic superlattice in which they found similar type of behaviour [4].

Since our interest was to prepare ferromagnetic nanocomposites by cold deformation, we decided to study the expected properties of such materials within a simple molecular field approach. In the calculation presented below, we have examined properties of two ferromagnetic materials possessing different magnetisation and Curie temperature, which are exchange coupled through their interface. A simple 1D model is presented and the extrapolation to 3D is described. Temperature dependence of magnetisation and anisotropy in systems of local moments is calculated. An extension to rare earth (R) – transition metal (T) alloys, in which large 3D interactions due to the T moments and large anisotropy due to the R moments coexist, is presented. In the last section of this chapter, an explanation to RT system is presented. This constitutes a model for the best hard-soft nanocomposite associating high anisotropy of the – element with large exchange interaction of the T – one.

3.2. 1D modelling of a coupling between nanograins

3.2.1. Molecular field modelling of a heterogeneous system

The static properties of a magnetic system in the ordered state can be well described within the molecular field approach. The molecular field B_i acting on atom i is expressed as:

$$B_i = \sum_j n_{ij} \langle \mu_j \rangle_T \qquad \text{(Equation 3.1)}$$

where n_{ij} is the molecular field coefficient, $\langle \mu_j \rangle_T$ is the thermal average of μ_i, at temperature T, and the summation extends over all other atoms, j. Assuming that interactions exist between first neighbours only, relation (3.1) becomes :

$$B_i = \sum_{j=1}^{Z} n_{ij} \langle \mu_j \rangle_T \qquad \text{(Equation 3.2)}$$

Where the summation is restricted to the Z first nearest neighbours of atom i.

In this section where a 1D model is developed, atoms are assumed to form a stacking of $2N + 1$ planes, the overall structure being symmetric about a central plane denoted by 0 (figure 3.1.a). Atoms in plane i have z_0 neighbours in their own plane, z_- neighbours in plane $i - 1$ and z_+ neighbours in plane $i + 1$ ($z_0 + z_- + z_+ = Z$, the total number of nearest neighbour atoms). To model the heterogeneous nature of matter, which is our precise interest, atoms from $i = 1$ to I are assumed to belong to material (I), while atoms from $i = I + 1$ to N ($N - I$ is defined as J) are assumed to belong to material (II). In addition, it is assumed that, within a given material, interactions with all neighbours are identical, *i.e.*, $n_{ij} = n_{(I)}$ within (I) and $n_{ij} = n_{(II)}$ within (II). Within (I), the molecular field is expressed as:

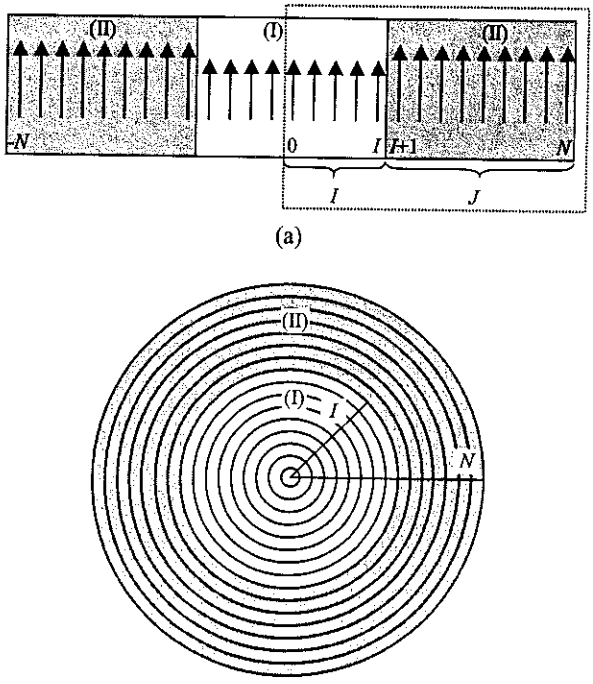

Figure 3.1 : Schematic diagram of the model nanocomposite systems comprising two distinct materials, (I) and (II), considered for (a) 1D calculations and (b) 3D calculations. The relative sizes of the components are characterized by the number of atomic planes, I and J for material (I) and (II), respectively.

$$B_i^{(I)} = n_{(I)} z_- \langle \mu_{i-1} \rangle_T + n_{(I)} z_0 \langle \mu_i \rangle_T + n_{(I)} z_+ \langle \mu_{i+1} \rangle_T \qquad \text{(Equation 3.3.a)}$$

and within (II), it is expressed as:

$$B_i^{(\mathrm{II})} = n_{(\mathrm{II})} z_- \langle \mu_{i-1} \rangle_T + n_{(\mathrm{II})} z_0 \langle \mu_i \rangle_T + n_{(\mathrm{II})} z_+ \langle \mu_{i+1} \rangle_T \qquad \text{(Equation 3.3.b)}$$

The molecular field in plane I at the interface is:

$$B_I^{(\mathrm{int})} = n_{(\mathrm{I})} z_- \langle \mu_{I-1} \rangle_T + n_{(\mathrm{I})} z_0 \langle \mu_I \rangle_T + n_{(\mathrm{int})} z_+ \langle \mu_{I+1} \rangle_T \qquad \text{(Equation 3.3.c)}$$

Where $n_{(\mathrm{int})}$ is the molecular field coefficient between nearest neighbour atoms located on opposite sides of the interface. Similarly, in plane $I + 1$, the molecular field is:

$$B_{I+1}^{(\mathrm{int})} = n_{(\mathrm{int})} z_- \langle \mu_I \rangle_T + n_{(\mathrm{II})} z_0 \langle \mu_{I+1} \rangle_T + n_{(\mathrm{II})} z_+ \langle \mu_{I+2} \rangle_T \qquad \text{(Equation 3.3.d)}$$

Finally, we take the entire sample to consist of a repeat stacking of identical bilayers of material (I) and (II) so that plane N may be assumed to be next to plane $-N$.

To this set of $2N + 1$ equations, which expresses the molecular field as a function of the magnetic moments, another set of equations is associated which expresses the moments as a function of the molecular field. Assuming classical moments, this is:

$$\langle \mu_i \rangle_T = L(x_i) = \coth(x_i) - \frac{1}{x_i} \qquad \text{(Equation 3.4)}$$

where $L(x_i)$ is the Langevin function, $x_i = \dfrac{\mu_i(0) B_i}{k_B T}$ and i runs from $-N$ to N.

3.2.2. Magnetisation

The $\langle \mu_i \rangle_T$'s and B_i's can be calculated self-consistently from the above 2 sets of equations, thus allowing the moment configuration to be deduced. For numerical calculations, the $\langle \mu_i \rangle_T$'s were expressed in terms of the zero temperature moment $\mu(0)$ which was assumed to be the same in both materials (I) and (II). The Curie temperature in (I), $T_c^{(\mathrm{I})}$, was taken as a reference ($n_{(\mathrm{I})}$ is related to $T_c^{(\mathrm{I})}$ through $Z n_{(\mathrm{I})} \mu_0^2(0) = 3 k_B T_c^{(\mathrm{I})}$, this equation is held for $n_{(\mathrm{II})}$, where the effective moment, μ_{eff}, is identical to $\mu(0)$ for a system of classical moments). $z_0 = 2z_- = 2z_+$ was assumed (for an fcc system, along <111>, $z_0 = 6$, $z_- = z_+ = 3$). Calculations were performed for various values of the four parameters: $T_c^{(\mathrm{I})}$, I, $n_{(\mathrm{int})}$ and T (five layers of the high T_c phase are considered, *i.e.*, $J = 5$). Initially, all moments were

assumed to be equal and saturated. This provides initial values for the B_i's (equation 3.3) from which the $\langle \mu_i \rangle_T$'s are extracted (equation 3.4). The molecular field in each plane was then recalculated and the procedure was repeated until $\Delta\mu_i / \mu_i < 10^{-8}$ where $\Delta\mu_i$ is the difference between two consecutive values of μ_i.

The magnetisation profile at $T = T_c^{(I)}$ is shown in figure 3.2.a, for a system characterized by $T_c^{(II)} = 2T_c^{(I)}$, $I = 5$ and $n_{(int)} = (n_{(I)} + n_{(II)})/2$ (*i.e.*, $n_{(int)}$ is simply taken as the average of $n_{(I)}$ and $n_{(II)}$). The moment configuration is compared to the configuration which would be obtained in the absence of coupling between (I) and (II) when $n_{(int)} = 0$ (note that the moments in (II) next to the interface have reduced values with respect to the bulk value due to the lower number of neighbouring moments). The additional interactions resulting from coupling across the interface lead to a significant induced magnetisation in (I) and a small increase in the magnetisation in (II). The latter observation justifies the fact that we consider just five layers in the high T_c material. The induced magnetisation in (I) occurs up to the centre even though coupling only exists between first nearest neighbours. For $I = 20$ (figure 3.2.b), the polarization is still significant at the centre of (I), but the higher the value of I, the lower the polarization at the centre. Actually, comparison of Figures 3.2.a and 3.2.b shows that it is more significant to consider the distance of a given plane from the interface. The polarization decreases with distance from the interface, amounting to about 0.2 M_s at the fifth plane.

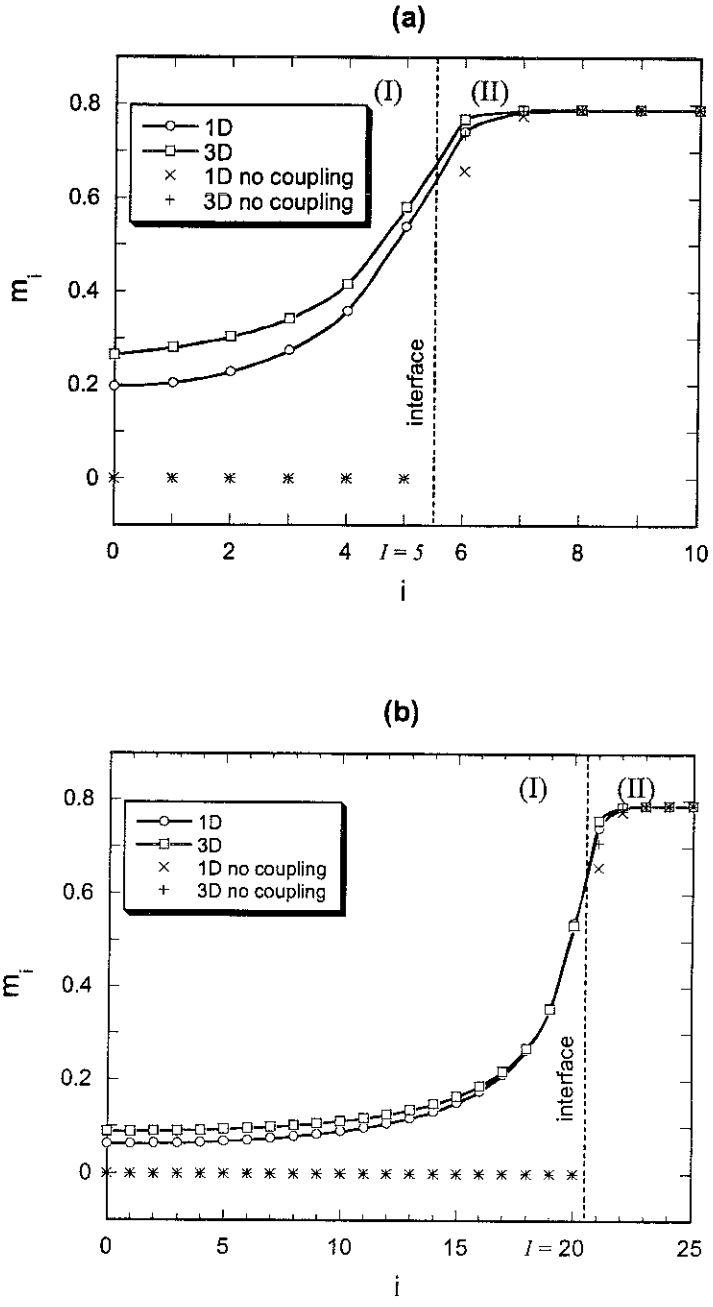

Figure 3.2: Magnetisation profiles at the interface between material (I) and material (II) at temperature $T = T_c^{(\mathrm{I})} = \frac{1}{2} T_c^{(\mathrm{II})}$ for (a) I = 5 and (b) I = 20 (the number of planes in (I) is $2I + 1$). Symbols: ×: $n_{(\mathrm{int})} = 0$ (no coupling), 1D calculation; +: $n_{(\mathrm{int})} = 0$, 3D calculation; ○: $n_{(\mathrm{int})} = (n_{(\mathrm{I})} + n_{(\mathrm{II})})/2$, 1D calculation; □: $n_{(\mathrm{int})} = (n_{(\mathrm{I})} + n_{(\mathrm{II})})/2$, 3D calculation.

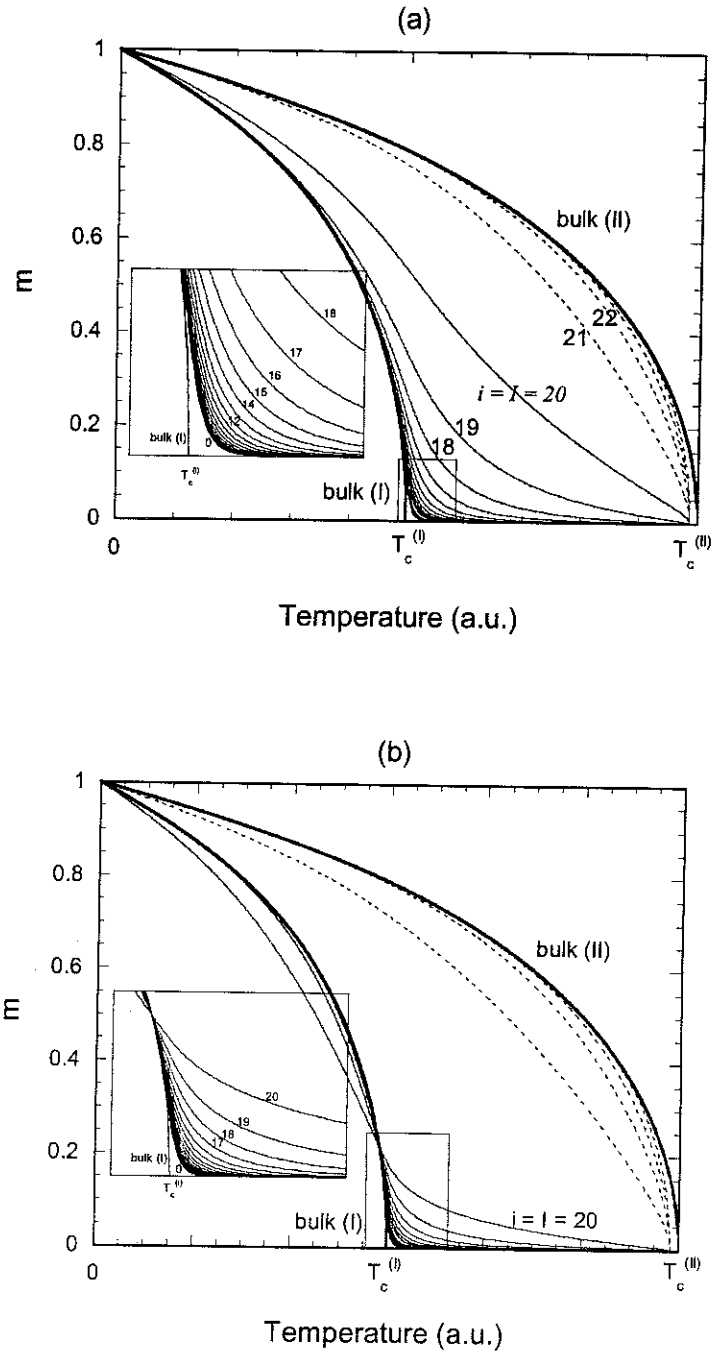

Figure 3.3: Temperature dependence of the reduced magnetisation $m_i = \mu_i(T)/\mu_i(0)$ in different planes within (I) – thin solid lines and (II) – broken lines compared to the temperature dependence of the reduced magnetisation in the bulk – thick solid lines (a) $I = 20$, $n_{(\mathrm{int})} = (n_{(\mathrm{I})} + n_{(\mathrm{II})})/2$ and (b) $I = 20$, $n_{(\mathrm{int})} = (n_{(\mathrm{I})} + n_{(\mathrm{II})})/10$. The planes are labeled $i \leq 20$ in the low-T_c material.

The temperature dependence of the reduced magnetisation $m_i(T) = \mu_i(T)/\mu_i(0)$ in different planes i, within (I) and (II) is compared in Figure 3.3.a to the temperature dependence of the bulk reduced magnetisation $m_b(T)$ (assumed to be described by the Langevin function $L(x_i)$ with $\mu_i(0) = \mu(0)$ and $B_i = 3k_B T_c^{(I)}/\mu(0)$ in phase (I) and $B_i = 3k_B T_c^{(II)}/\mu(0)$ in phase (II)) in both materials for $I = 20$ and $n_{(int)} = (n_{(I)} + n_{(II)})/2$. The difference compared to bulk behaviour becomes progressively more significant as temperature is increased, the effect being greater for planes close to the interface. This behaviour is a consequence of the fact that the temperature dependence of the magnetisation is directly related to the strength of exchange interactions while the 0 K magnetisation itself does not depend on the strength of the interactions (see equation (3.3)). The temperature dependence was also evaluated for a lower assumed value of interface coupling $n_{(int)} = (n_{(I)} + n_{(II)})/10$ (Fig. 3.3.b). Close to the interface, the magnetisation at relatively low temperature is reduced with respect to the bulk value due to the reduction in exchange coupling. Inversely, an induced magnetisation persists in (I) (although 2 – 3 times less than for $n_{(int)} = (n_{(I)} + n_{(II)})/2$) at $T > T_c^{(I)}$ due to coupling with (II). As a result of the qualitatively different behaviours at low and high temperatures respectively, the temperature dependence of the magnetisation in any given plane of (I) crosses that of the bulk at a certain temperature below $T_c^{(I)}$. For $n_{(int)} = (n_{(I)} + n_{(II)})/10$, this temperature is about $0.95\,T_c^{(I)}$. As $n_{(int)}$ increases up to $n_{(I)}$ the crossing temperature decreases down to 0 K. For $n_{(int)} = n_{(I)}$, there is no crossing since the magnetisation in all planes of (I) is higher than in the bulk. This is the case for $n_{(int)} = (n_{(I)} + n_{(II)})/2$, in Figure 3.3.a.

3.2.3. Anisotropy

The magnetocrystalline anisotropy is defined in terms of the dependence of the free energy on the direction of the magnetisation. In systems of classical moments, the decrease of anisotropy with temperature is only determined by thermally activated fluctuations of the moment orientations. For a cubic ferromagnet, the free energy is usually expanded in a power series in the direction cosines α_1, α_2, α_3, of the magnetisation direction relative to the crystallographic axes. Symmetry dictates that this power series takes the form:

$$F = K_0 + K_2(T)(\alpha_1^2\alpha_2^2 + \alpha_2^2\nu_3^2 + \alpha_3^2\alpha_1^2) + K_4(T)\alpha_1^2\alpha_2^2\alpha_3^2 + \ldots \qquad \text{(Equation 3.5)}$$

Akulov studied the classical treatment of single-spin anisotropy [5]. In his model, it is assumed that each spin has an intrinsic direction dependent energy, arising from interaction with the crystal field. Free energy is given by perturbation theory, to the first order in the interaction constant $K_2(0)$, as

$$F = F_0 + K_2(0)\left\langle \nu_1^2\nu_2^2 + \nu_2^2\nu_3^2 + \nu_3^2\nu_1^2 \right\rangle + \ldots \qquad \text{(Equation 3.6)}$$

where ν_1, ν_2, ν_3 are the direction cosines of the spin considered. The averages are to be calculated in the isotropic or undisturbed distribution function. This free energy is then to be compared with the phenomenological equation (3.5), which defines the temperature dependent anisotropy constant $K_2(T)$. He considered the free energy along directions <100> and <110>. The anisotropy constant can be deduced from the difference in free energy of these directions. Using a simple classic argument, Akulov showed that:

$$K_2(T)/K_2(0) \approx [m(T)]^{10} \qquad \text{(Equation 3.7)}$$

where $m(T) = M(T)/M(0)$. Akulov compared the theoretical result with data of iron, and concluded that the law was quite accurately obeyed up to $T \sim 0.65T_c$.

Zener generalized the Akulov 10th power law to the $l(l+1)/2$ power law [6]. Zener showed that if the angular dependent factor in equation (3.5) are regrouped in terms of spherical harmonics $Y_l^m(\alpha)$, and if $\kappa_l(T)$ is the coefficient of the terms of given l ($\kappa_l(T)$ being a linear combination of the $K_l(T)$), then:

$$\kappa_l(T)/\kappa_l(0) \approx [m(T)]^{l(l+1)/2} \qquad \text{(Equation 3.8)}$$

For various insulating magnetic materials, which obey the law of localised magnetisation, the $l(l+1)/2$ law is in excellent agreement with experimental data for all temperatures. H. B. Callen and E. Callen improved the isolating model by taking into account quantum corrections to the ground state [7]. They showed that the temperature dependence of the anisotropy constant can be expressed by the modified Bessel functions. According to H. B. Callen and E. Callen, in the classical limit, the anisotropy constant of order l, characterizing atoms in plane i at temperature T, is $\kappa_{l,i}(T)$ and may be written as:

$$\frac{\kappa_{l,i}(T)}{\kappa_{l,i}(0)} = \hat{I}_{l+1/2,i}\left(\hat{I}^{-1}_{3/2,i}\left(m_i(T)\right)\right) = \hat{I}_{l+1/2,i}\left(L^{-1}\left(m_i(T)\right)\right) \qquad \text{(Equation 3.9)}$$

where $\kappa_{l,i}(0)$ is the anisotropy constant at 0 K, L is the Langevin function which is equal to $\hat{I}_{3/2}$ and $\hat{I}_{l+1/2,i}$'s are modified Bessel functions which depend on l and can be expressed in terms of hyperbolic Bessel functions $I_{l+1/2,i}$'s:

$$\hat{I}_{l+1/2,i}(X) = I_{l+1/2,i}(X)/I_{1/2,i}(X) \qquad \text{(Equation 3.10.a)}$$

$$I_{1/2}(X) = \int_{-1}^{1} Y_0^0(m')\exp(Xm')dm' \qquad \text{(Equation 3.10.b)}$$

$$I_{l+1/2}(X) = \int_{-1}^{1} Y_l^0(m')\exp(Xm')dm' \qquad \text{(Equation 3.10.c)}$$

where $Y_l^0(m)$'s are spherical harmonic functions. Figure 3.4 shows $\kappa_l(T)/\kappa_l(0)$ as a function of m derived from equations (3.9) and (3.10), for $l = 2$ and 4.

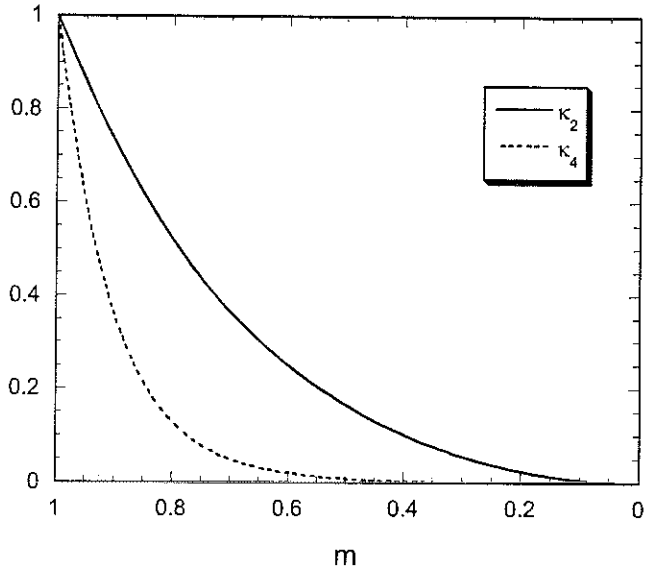

Figure 3.4: Magnetisation dependence of anisotropy constant of order $l = 2$ and 4 in the classical limit.

In our model, it can be expected that the anisotropy value is affected at the interface between (I) and (II), in a similar way to which the moment polarization is affected. To first order, $\frac{\kappa_{l,i}(T)}{\kappa_{l,i}(0)} \approx [m_i(T)]^{l(l+1)/2}$, the $l(l+1)/2$ law. The temperature dependence of $k_l = \kappa_{l,i}(T)/\kappa_{l,i}(0)$ ($l = 2$ and $l = 4$) are plotted in figures 3.5.a and 3.5.b, respectively ($n_{(\text{int})} = (n_{(\text{I})} + n_{(\text{II})})/2$). To first approximation, the ratio of anisotropies in two different planes at temperature T is:

$$\frac{\kappa_{l,i}(T)}{\kappa_{l,i+1}(0)} = \left[\frac{\mu_i(T)}{\mu_{i+1}(T)}\right]^{l(l+1)/2} \qquad \text{(Equation 3.11)}$$

i.e., the relative variation of anisotropy from one plane to the next is much more abrupt than the variation of magnetisation. Thus at $T = T_c^{(\text{I})}$, the 2nd order anisotropy in the fifth plane from the interface within (I) amounts to $0.025\,\kappa_{2,\text{b}}$, where $\kappa_{2,\text{b}}$ is the 0 K bulk 2nd order constant, while the magnetisation is only reduced to 0.2 M_s. At the same temperature, the 4th order anisotropy in the same fifth plane amounts to $0.01\,\kappa_{4,\text{b}}$.

It can thus be expected that an anisotropy value at the interface between (I) and (II), in a similar way to which the moment polarization is affected.

3.3. 3D modelling of coupling between nanograins

A simple extension of the above calculations to 3D is obtained by assuming that the atoms are distributed on successive spherical surfaces (figure 3.1.b). The total sphere radius is N. The outer part, for radii ranging from $I + 1$ to N, consists of the high-T_c material (II), the core is a sphere of radius I and consists of the low-T_c material (I).

The number of atoms contained within the i^{th} spherical surface is $3i^2(d/r_{at})^3$, where d is the distance between the centres of neighbouring shells and r_{at} is the atomic radius. $(d/r_{at}) = \sqrt{2/3}$ was assumed, which corresponds to the d value between atomic planes along the <111> direction of an fcc material. The parameters z_0, z_- and z_+ within a given shell were taken to be proportional to the number of atoms within this shell with the additional conditions that $Z = 12$ whatever the value of i. z_- and z_+ tend to 3 and z_0 tends to 6 as N tends to infinity.

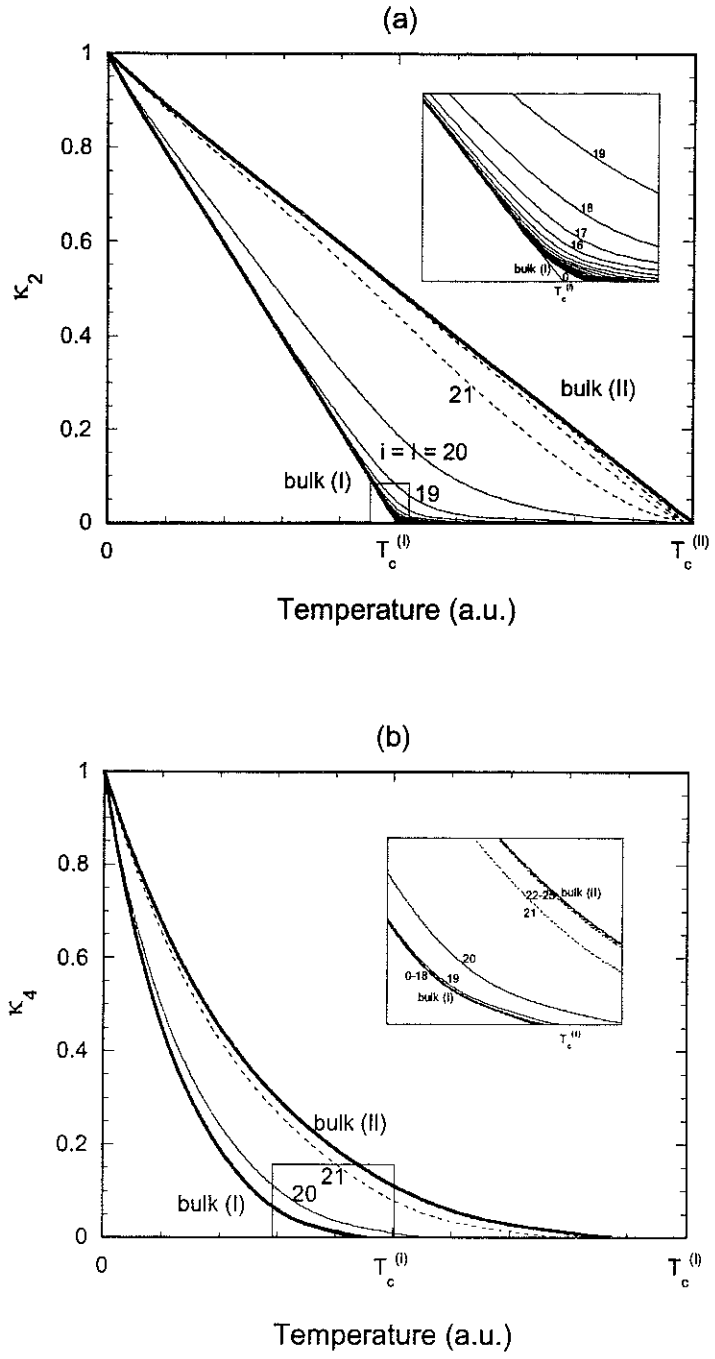

Figure 3.5: Temperature dependence of the reduced anisotropy constant $k_l = \kappa_l(T)/\kappa_l(0)$ in different planes within (I) – solid thin curves and (II) – broken curves compared to the temperature dependence of the reduced anisotropy constant in the bulk – thick solid lines for $n_{(\mathrm{int})} = (n_{(\mathrm{I})} + n_{(\mathrm{II})})/2$ (a) $l = 2$ and (b) $l = 4$. The planes are labeled $i \le 20$ in the low-T_c material. Planes $i = 0 - 18$ and $i = 22 - 25$ are indistinguishable from the bulk profiles.

The same type of calculations as for 1D was performed. Because z_0, z_- and z_+ are now dependent on i, the cyclic boundary conditions no longer apply. A 3D magnetisation profile is compared to the 1D profile for consistent parameter values in Figures 3.2.a and 3.2.b. The results are qualitatively similar. Actually, 1D and 3D calculations differ only in the number of atoms in neighbouring planes. In 3D, the number of atoms per shell increases when moving out from the centre of the sphere. Thus the atoms in the last shell of material (I) have a greater number of neighbours in the outer shell, which belongs to the high-T_c material (II) than in the inner shell, which belongs to low-T_c material (I). It results that the polarization in 3D is enhanced with respect to the polarization in 1D.

3.4. Modelling the coupling between rare earth-transition metal nanograins

High anisotropy ($SmCo_5$, $Nd_2Fe_{14}B$, etc...) or high magnetostriction (RFe_2) magnetic materials are based on rare earth (R) – transition metal (T) compounds. Magnetic ordering is mainly determined by large T-T exchange interactions whereas the anisotropy results from the coupling of the anisotropic R 4*f* shell with the environment.

Modelling the behaviour of nanosystems including such R-T compounds is discussed in this section. Three systems were considered, namely $SmCo_5$/Co, $Nd_2Fe_{14}B$/Fe, and $Pr_2Fe_{14}B$/Fe. The magnetic properties of the considered compounds, relevant to the present discussion (Curie temperature T_c, crystal field parameters $B_{n,m}$) are given in table 3.1. 3D calculations only are reported here.

Within the Fe or Co region, as well as within the R-T region, calculation of the T magnetisation is essentially identical to calculations performed in the above sections. The temperature dependence of the reduced magnetisation $m_i^{\mathrm{T}}(T)$ (T = Fe or Co) is presented in Figure 3.6 for $I = 20$ and $n_{(\mathrm{int})} = (n_{(\mathrm{I})} + n_{(\mathrm{II})})/2$. The results are qualitatively similar to those obtained in the previous sections and presented in Figure 3.3.a. However they are quantitatively different because the Curie temperatures $T_c^{(\mathrm{I})}$ and $T_c^{(\mathrm{II})}$ are not in the ratio of 1:2.

Table 3.1: Magnetic parameters used for modelling the coupling between rare earth – transition metal nanograins.

	$SmCo_5$	$Nd_2Fe_{14}B$	$Pr_2Fe_{14}B$
T_c (K)	997 [8]	592 [9]	565 [10]
n_{RT} (K/μ_B^2)	20 [8]	8.67 [9]	10.51 [10]
B_2^0 (K)	-8.0 [8]	-2.2 [9]	-3.0 [10]
B_4^0 (10^{-2} K)	–8.5 [8]	11.9 [9]	–0.76 [10]
B_6^0 (10^{-4}K)	0 [8]	10 [9]	–80 [10]

The R magnetic state at a given temperature T is defined in principle by R-T and R-R exchange interactions as well as by crystalline electric field (CEF) interactions. Of all these terms however, the R-T interactions are dominant. Neglecting the other terms, the thermal average of $g_J\mu_B J_z$, which defines the magnetisation, is deduced by assuming that the separation between each level of the J multiplet is the same, and equal to $g_J\mu_B B_{ex,i}$ where g_J is the Landé factor for the considered R element, μ_B is the Bohr magneton and $B_{ex,i} = n_{RT}\langle\mu_{T,i}\rangle_T$, where n_{RT} is the molecular field coefficient describing the coupling between the R and T moments (see table 3.1).

The R moment is then given by the Brillouin function $B_J(x_i)$ where the quantum number J characterizes a given element R and x_i is equal to:

$$B_J(x_i) = \frac{2J+1}{2J}\coth\left(\frac{2J+1}{2J}x_i\right) - \frac{1}{2J}\coth\left(\frac{1}{2J}x_i\right) \qquad \text{(Equation 3.12)}$$

$$x_i = \frac{g_J\mu_B JB_{ex,i}}{k_B T}$$

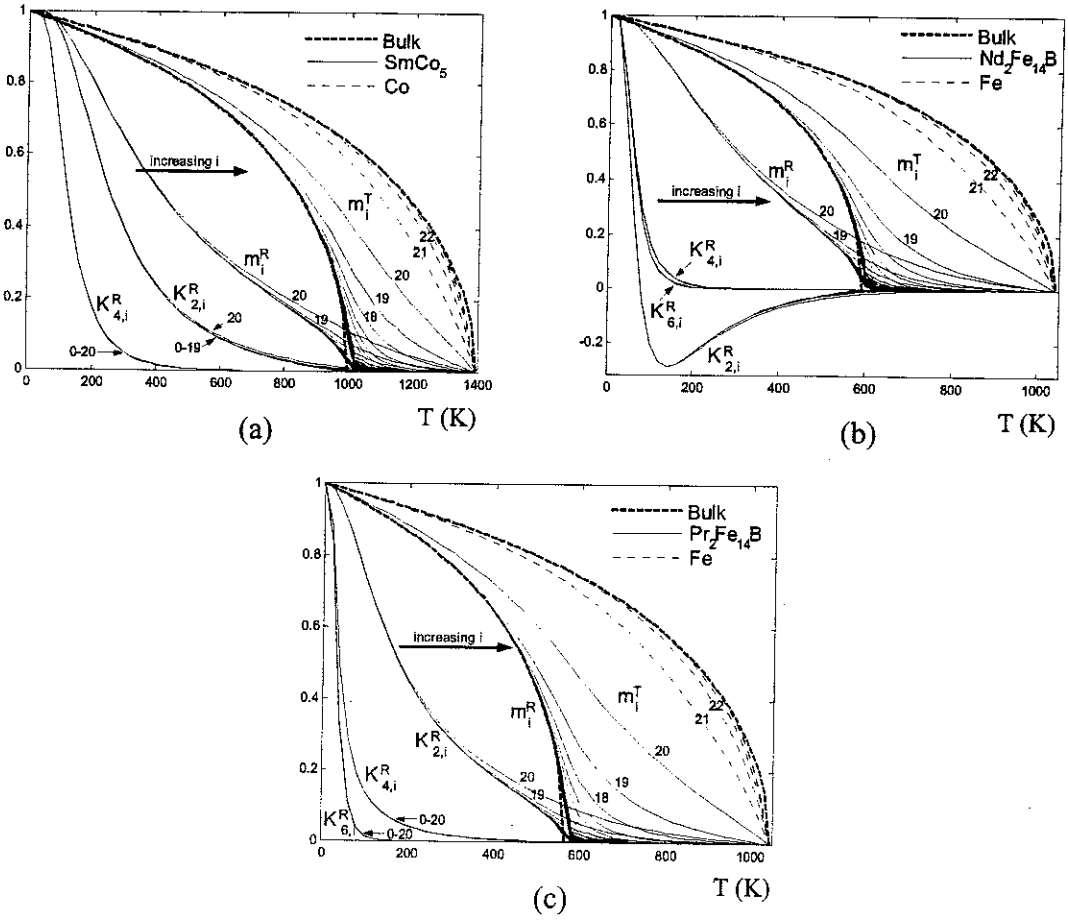

Figure 3.6: Temperature dependence of $m_i^{\mathrm{T}}(T)$ (T = Fe or Co), $m_i^{\mathrm{R}}(T)$ (R = rare earth), and the anisotropy constants $k_{n,i}^{\mathrm{RT}}(T)$ ($I = 20$ and $n_{(\mathrm{int})} = (n_{(\mathrm{I})} + n_{(\mathrm{II})})/2$) (a) $SmCo_5$/Co, $Nd_2Fe_{14}B$/Fe and (c) $Pr_2Fe_{14}B$/Fe. The planes are labeled in the low T_C material (m^{T} and m^{R}) and $i > 20$ in the high T_C material (m^{T} only) (as not all planes are individually marked, an arrow indicating the direction of increasing is included).

The calculated temperature dependence of $m_i^{\mathrm{R}}(T)$ for the 3 systems considered is presented in Figure 3.6. In all cases, $m_i^{\mathrm{R}}(T)$ is higher than the bulk $m_b^{\mathrm{R}}(T)$, R-T exchange interactions being enhanced as a result of the coupling between the R-T compound (low-T_c material (I)) on one side and Fe or Co metal (high-T_c material (II)) on the other side. However the decrease of the R magnetisation with temperature becomes significant in R-T compounds at lower temperature than that of the T magnetisation. Thus, at a given finite temperature, the polarisability of the R magnetisation is less than that of the T magnetisation. This explains

why the effect of the interface exchange coupling in Figure 3.6 is much less spectacular for the R magnetisation than it is for the T magnetisation.

Let us now turn to the evaluation of anisotropy. In the present systems, the Fe or Co anisotropy is negligible with respect to the $SmCo_5$, $Nd_2Fe_{14}B$, or $Pr_2Fe_{14}B$ anisotropy and thus only the rare-earth compound anisotropy was considered. It is the combination of a significant T anisotropy and a dominant R anisotropy. The T anisotropy was taken from literature [10, 11] and R at 0 K. The R anisotropy is related to the $\langle O_{n,m,i} \rangle_T$'s, *i.e.* the thermal averages of the Stevens operators:

$$K_2^R = -\frac{1}{2}\left(3\kappa_2^0 + 10\kappa_4^0 + 21\kappa_6^0\right) \qquad \text{(Equation 3.13.a)}$$

$$K_4^R = \frac{1}{8}\left(35\kappa_4^0 + 189\kappa_6^0\right) \qquad \text{(Equation 3.13.b)}$$

$$K_6^R = -\frac{231}{6}\kappa_6^0 \qquad \text{(Equation 3.13.c)}$$

where $\kappa_n^0 = B_n^0 \langle O_n^0 \rangle_T$. The $\langle O_{n,m,i} \rangle_T$'s were calculated following the same procedure used to evaluate the R magnetisation. The resulting temperature dependence of the reduced anisotropy constants $K_{n,i}^R$ in $SmCo_5$/Co, $Nd_2Fe_{14}B$/Fe, and $Pr_2Fe_{14}B$/Fe nanosystems are shown in Figure 3.6. The same qualitative relationship as observed above between m_i and $K_{n,i}$ (section 3.2.2 and 3.2.3) exists between m_i^R and $K_{n,i}^R$. This, combined with the fact that the R magnetisation polarisability is weaker than the T magnetisation polarisability, explains why the absolute induced anisotropy is almost negligible (Figure 3.6).

3.5. Interface values of magnetisation and anisotropy

We have developed a simple model, based on the mean field approach, to calculate the change in the intrinsic magnetic properties of two different materials, with different Curie temperatures, intimately mixed on the nanometer scale (*i.e.*, nanocomposite systems). As we are concerned with mixed transition metal and rare-earth transition-metal systems (see 3.4), we consider nearest neighbour interactions only, supposing that RKKY interactions are negligible. Though our results are not surprising, indeed the qualitative behaviour observed is

intuitive, our simple model allows an approximation of the length scales over which the modification of intrinsic properties due to exchange interactions is significant in nanocomposite systems. The calculated temperature dependence of the magnetisation in material (I) of the present study (low-T_c material) is characterized by an inflection point occurring at a temperature, which is slightly higher than $T_c^{(I)}$. Such behaviour results from the fact that the moments in (I) are weakly coupled between themselves as well as with the moments in (II). The same behaviour characterizes the temperature dependence of the magnetisation at the R sites in rare-earth iron garnets and R-T compounds, when the exchange interactions at the R sites are reduced. There is much experimental evidence for the influence of exchange coupling on the extrinsic magnetic properties of nanocomposite materials and the consequential influence on intrinsic magnetic properties has been evoked [12]. In a recent study on $Nd_2Fe_{14}B$/Fe nanocomposite materials, Lewis and Panchanathan have reported an increase in the Curie temperature of the hard constituents from approximately 575 K to 590 – 600 K [13]. They have suggested that this increase is due to either exchange coupling of the $Nd_2Fe_{14}B$ grains with the Fe grains, or to internal stresses. However, our calculations show that the modification of the magnetisation of the low-T_c material is significant over just 5 to 10 interatomic distances, which is very much shorter than the grain size of the low-T_c constituent in these systems (25 – 50 nm, *i.e.*, it is more than 100 atomic distances). Moreover, due to the coupling between all moments, it is impossible to define separate Curie temperatures for the different materials in these systems. The actual Curie temperature, at which the magnetisation at all sites vanishes, is close to, but less than, $T_c^{(II)}$ (see figure 3.3).

In conclusion, at finite temperature, the intrinsic magnetic properties of the constituent phases in nanostructured systems differ from bulk properties. This is due to exchange coupling through the interface. As a general rule, the magnetisation is relatively more affected than the anisotropy. At the interface between two simple ferromagnets with Curie temperatures in the ratio 1:2 (this corresponds for instance to $Y_2Fe_{14}B$/Fe metal), an induced magnetisation which amounts to up to 50 % of the 0 K value may be observed at the Curie temperature of the low T_c material. In R-T compounds, the induced magnetisation and anisotropies at the T sites are higher than those at the R sites. The induced interface R magnetisation calculated for known hard magnetic materials ($SmCo_5$, $R_2Fe_{14}B$) never exceeds 10 % of the 0 K value and the R induced anisotropy is less than 1%. The modification of intrinsic magnetic properties should in turn influence magnetisation processes. These effects should be greater in systems where

the domain wall width, which defines the activation volume in which reversal is initiated, is of a few interatomic distances, and thus corresponds to the distance over which intrinsic magnetic properties are affected by coupling. Such domain wall widths are, at room temperature, characteristic of T-rich R-T compounds. At this temperature, exchange energy and anisotropy are not significantly affected by coupling. At higher temperature when the induced magnetisation becomes significant, the anisotropy is very weak. Thus, the change in intrinsic magnetic properties through interface exchange coupling will not dramatically affect magnetisation reversal processes.

Finally, let us point out that we have discussed in this chapter the systems of rare earth – transition compounds whereas the composites, which we tried to prepare were based on the FePt system. At the outset of this thesis, the aim was to prepare R-T composites. However we established that the preparation of such nanocomposites by mechanical deformation was extremely difficult. We thus focused our attention on the FePt system. As we did not succeeded in preparing truly nanocomposites hard-soft systems, we did not apply the above analysis to this particular system.

References

1. Coehoorn, R., D.B. de Mooij, J.P.W.B. Duchateau, and K.H.J. Buschow, J. de Phys., **49** (1988) C8 669.
2. Kneller, E.F. and R. Hawig, *The exchange-spring magnet: a new material principle for permanent magnets.* IEEE Trans. Magn., **27** (1991) 3588.
3. Carrico, A.S. and R.E. Camley, *Size and interface in the phase transitions of antiferromagnetic superlattices.* Sol. State Commun., **82** (1992) 161.
4. Wang, R.W. and D.L. Mills, *Onset of long-range order in superlattices: Mean-field theory.* Phys. Rev. B, **46** (1992) 11681.
5. Akulov, N., Z. Phys., **100** (1936) 197.
6. Zener, C., *Classical Theory of the Temperature Dependence of Magnetic Anisotropy Energy.* Phys. Rev., **96** (1954) 1335.
7. Callen, H.B. and E. Callen, *The present status of the temperature dependence of magnetocrystalline anisotropy, and the l(l+1)/2 power law.* J. Phys. Chem. Solids., **27** (1966) 1271.
8. Givord, D., J. Laforest, J. Schweizer, and F. Tasset, J. Appl. Phys., **50** (1979) 2008.
9. Gavigan, J.P., H.S. Li, J.M.D. Coey, J.M. Cadogan, and D. Givord, J. Phys. F: Met. Phys., **49** (1988) 779.
10. Alameda, J.M., D. Givord, R. Lemaire, and Q. Lu, *Co Energy and Magnetization Anisotropies in RCo_5 Intermetallics Between 4.2 K and 300 K.* J. Appl. Phys., **52** (1981) 2079.
11. Givord, D., H.S. Li, and R. Perrier de la Bâthie, *Magnetic Properties of $Y_2Fe_{14}B$ and $Nd_2Fe_{14}B$ Single Crystals.* Sol. State Commun., **51** (1984) 857.
12. Coehoorn, R., D.B. de Mooij, and C. de Waard, *Meltspun Permanent Magnet Materials Containing Fe_3B as the Main Phase.* J. Magn. Magn. Mater., **80** (1989) 101.
13. Lewis, L.H. and V. Panchanathan. *Extrinsic Curie temperature and spin reorientation changes in $Nd_2Fe_{14}B/\alpha$-Fe nanocomposites.* in *Proceedings of the 15th International Workshop on Rare Earth Magnets and Their Applications.* (1998) Dresden: Werkstoff-Information gesellschaft, Franfurt. 233.

Chapter 4: Magnetisation reversal in Fe-Pt foils

Résumé en Français

Chapitre 4: Renversement d'aimantation dans les feuilles Fe-Pt

L'étude du renversement d'aimantation est celle des mécanismes par lesquels les moments magnétiques changent d'orientation sous l'effet d'un champ appliqué dont une composante est antiparallèle à la direction initiale d'aimantation saturée. La coercitivité est la propriété des matériaux magnétiques dits durs de résister à un tel champ. Le champ coercitif est le champ requis pour renverser l'aimantation.

La présence d'une barrière d'énergie qui sépare l'état initial de l'état final de plus basse énergie est indispensable à la présence de coercitivité. Dans ce chapitre, nous analysons les processus de renversement d'aimantation dans des systèmes pour lesquels la barrière d'énergie coercitive est déterminée par la seule anisotropie magnétocristalline. Nous considérons tout d'abord le renversement dans un système idéal, qui se fait selon le processus de rotation cohérente décrit par Stoner et Wohlfarth. Dans un système réel, le renversement d'aimantation n'a pas lieu par rotation cohérente, mais par une succession de processus : nucléation, propagation et dépiégeage. Nous décrivons les mécanismes possibles et présentons les modèles, respectivement micromagnétique et global, d'analyse de la variation thermique du champ coercitif. Les prédictions de ces modèles sont comparées aux résultats expérimentaux obtenus sur les alliages durs FePt que nous avons produits.

Par ailleurs, nous avons observé que les cycles d'hysteresis, obtenus dans un champ appliqué dans le plan des feuilles (IP) ou perpendiculairement à ce plan (PP), diffèrent et nous analysons ce phénomène. Nous discutons aussi des différences d'autre nature entre cycles IP et PP, observées dans les systèmes $FePt/Fe_3Pt$.

Les analyses du champ coercitifs dans le cadre des modèles micromagnétique et global donnent accès à la valeur de deux paramètres phénoménologiques, α et N_{eff}. Schématiquement, le paramètre α représente la réduction d'anisotropie dans la région critique de renversement d'aimantation et le paramètre N_{eff} représente l'intensité des interactions

(dipolaires) entre grains. Dans les matériaux durs FePt que nous avons produits, nous avons noté que la valeur du paramètre α est significativement plus faible que dans les matériaux durs classiques, de type $Nd_2Fe_{14}B$ ou ferrites. Considérant que la valeur de α représente l'influence des défauts sur la coercitivité et que plus la valeur de α est grande, meilleures sont les propriétés coercitives, ce résultat suggère que des performances supérieures devraient être atteignables en persévérant dans l'optimisation du procédé d'élaboration par déformation mécanique. Cette conclusion est en accord avec l'obtention récente de coercitivité supérieures à 4T dans des échantillons en couche mince, constitués de grains de FePt épitaxiés sur un substrat et isolés entre eux.

Les valeurs de N_{eff} obtenues sont comprises entre -0.27 et -0.42. Dans les autres matériaux magnétiques durs, les valeurs de N_{eff} sont positives en général, et ceci signifie que les interactions s'ajoutent au champ coercitif pour favoriser le retournement d'aimantation. Le comportement observé dans le système FePt pourrait être lié à la microstructure particulière source d'interactions dipolaires de signe opposé au signe habituel. Cependant, nous pensons plutôt qu'il indique que des interactions d'échange résiduelles entre grains sont présentes. La même inerprétation a d'ailleurs été proposée pour décrire la coercitivité de rubans NdFeB hypertrempés.

Le volume d'activation, v, est un autre paramètre caractéristique de la coercitivité. Dans de nombeux matériaux durs, la variation thermique du volume d'activation est approximativement proportionnelle au cube de l'épaisseur de paroi δ^3. Dans le système FePt, v et δ^3 augmentent ensemble avec la température, mais la variation de l'un en fonction de l'autre n'est pas exactement linéaire.

Nous avons observé de façon systématique que le champ coercitif des alliages FePt mesuré dans la configuration IP est supérieur d'environ 10 % au champ mesuré dans la configuration PP. Cette différence pourrait indiquer une différence entre les mécanismes de piégeage pour ces deux configurations. Une autre interprétation, qui nous paraît plus vraisemblable, est que les hétérogénéités magnétiques inhérentes au caractère hétérogène de ces systèmes impliquent que le concept de champs démagnétisants, simplement proportionnels à la valeur moyenne de l'aimantation globale, ne peut s'appliquer. La déviation par rapport au modèle classique est plus manifeste dans la configuration PP, pour laquelle les interactions dipolaires sont par essence bien supérieures.

Les cycles d'hysteresis mesurés dans la configuration IP des systèmes FePt/Fe_3Pt révèlent un retournement d'aimantation en deux étapes qui implique que nous n'avos pas réussi dans ces systèmes à développer le phénomène dit « d'exchange-spring ». Les épaisseurs des couches douces Fe_3Pt sont sans doute encore trop supérieures à celle de l'épaisseur de paroi dans FePt (environ 5 nm). De façon inattendue, nous avons observé que le renversement en deux étapes n'apparaît pas sur les cycles d'hysteresis mesurés dans la configuration PP. Nous avons montré que ce comportement s'interprète en supposant que le processus d'aimantation présente un caractère anisotrope, qui pourrait être dû à une anisotropie de forme des grains ou simplement être associé à la forme en feuille des échantillons. Nous avons dénommé ce processus « dipolar-spring ». Nous avons ainsi pu analyser quantitativement les cycles observés dans les deux configurations IP et PP.

Chapter 4: Magnetisation reversal in Fe-Pt foils

4.1. Introduction to coercivity

Magnetisation reversal of a magnetic system is the process by which the magnetic moments of the system reverse their orientations from an initially saturated state under the influence of a magnetic field, which has a component antiparallel to the initial magnetisation direction. Coercivity is the characteristic feature of hard magnetic materials in which magnetisation reversal does not take place immediately when the applied field is reversed. The *coercive field* H_c is the field needed to reverse the magnetisation. Classically, the coercive field is defined as the field, on the hysteresis cycle, for which the bulk magnetisation vanishes. In a more physically meaningful definition, the coercive field may be defined as the field where the largest number of moments reverses, *i.e.*, the maximum of the irreversible susceptibility $\chi^{irr} = \partial M / \partial H$. In most cases, both definitions of the coercive field are almost equivalent. However, there are cases where significant differences exist [1].

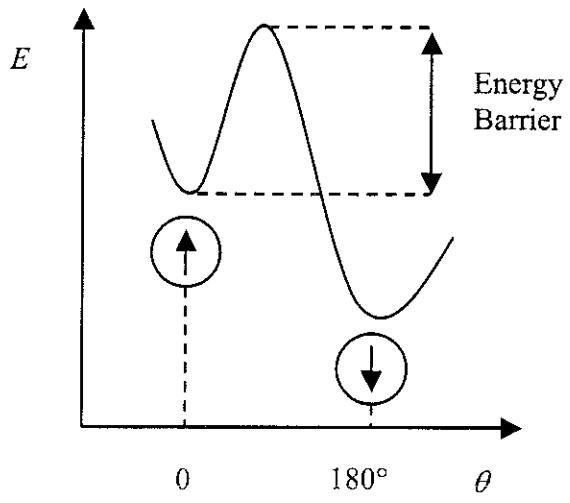

Figure 4. 1: The metastable coercive state (for $\theta = 0$) and the energy barrier for a magnet (θ is defined in figure 4.2).

The *origin of coercivity* is the presence of an energy barrier Δ between the initial and final states of the reversal process (see figure 4.1). The existence of this energy barrier indicates an anisotropy in the magnetic energy which can have two origins: - atomic scale anisotropy which is due to the crystalline electric field, acting on individual orbital magnetic moments (intrinsic properties); - or macroscopic scale anisotropy which originates from the anisotropy of the demagnetising field, acting on the resultant magnetisation (extrinsic properties).

In this chapter, we consider magnetisation reversal processes in systems for which the coercive energy barrier is assumed to be uniquely determined by magneto-crystalline anisotropy. In section 4.2, we describe reversal in an ideal system, following the Stoner-Wohlfarth model of coherent rotation. In real systems, the coercive field value is always much smaller than the Stoner-Wohlfarth ideal coercive field. Due to the presence of defects, magnetisation reversal occurs by nucleation – propagation – depinning, not by coherent rotation [1-6]. The possible mechanisms are schematically described in section 4.3 and simple models to describe the temperature dependence of H_c are discussed in section 4.4.1 (micromagnetic model) and sections 4.4.2 and 4.4.3 (global model). The predictions of these models are then compared to experimental results in FePt alloys produced by rolling/annealing in sections 4.5 and 4.6. Differences between the in plane (IP) and perpendicular-to-plane (PP) hysteresis cycles of the FePt and FePt/Fe_3Pt foils are explained in section 4.7 and 4.8, respectively.

4.2. Stoner-Wohlfarth model

Uniform coherent rotation describes magnetisation reversal in an ideal single-domain particle. It is a process in which all moments remain parallel and rotate in unison. It was analysed by Stoner and Wohlfarth [7]. Let us consider an ellipsoidal single-domain particle with an easy *c*-axis. Assume that θ and ψ are the angles between the *c*-axis and the spontaneous magnetisation M_s and between the *c*-axis and the applied field *H*, respectively (see figure 4.2.a). Neglecting dipolar interactions, two types of energy contribute to the total energy *E*: the anisotropy energy E_A and the Zeeman energy E_H:

$$E_A = K_2 \sin^2(\theta)$$

$$E_H = -\mu_0 M_s H \cos(\psi - \theta)$$

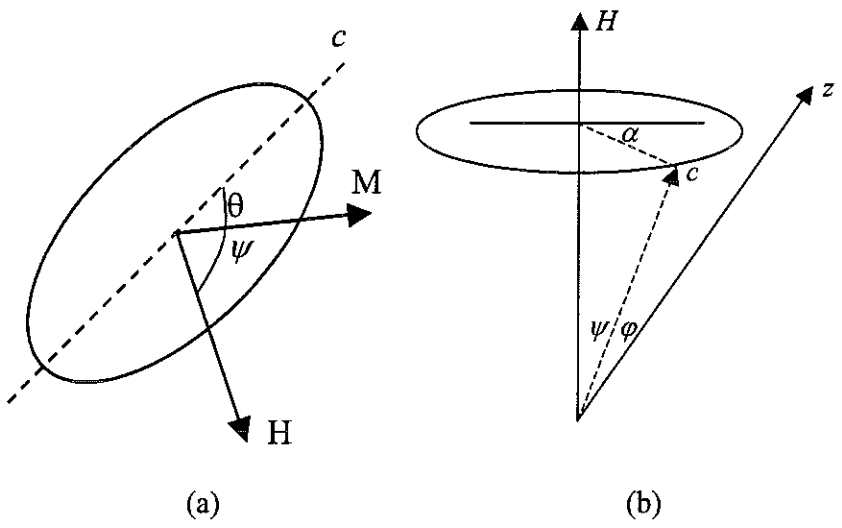

Figure 4. 2: Definition of angles θ, ψ, α, φ.

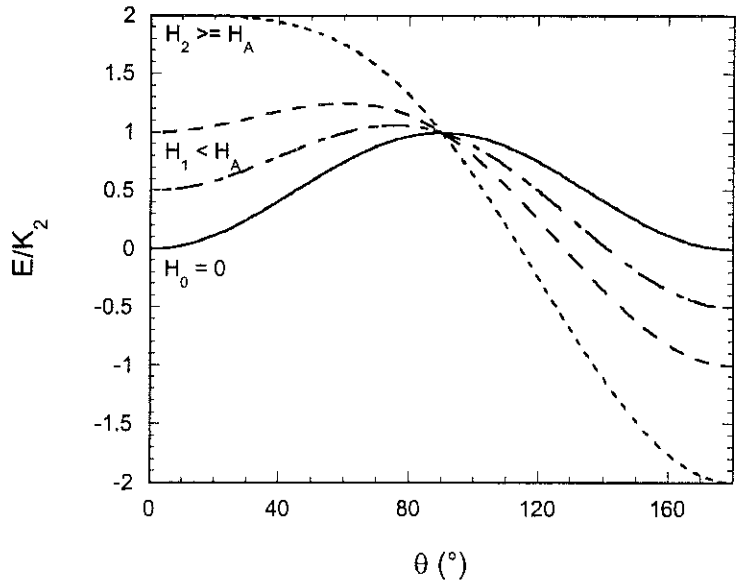

Figure 4. 3: Angular dependence of the total energy for different applied fields H ($H_0 < H_1 < H_2$, H_A is the anisotropy field) ($\psi = 0$) [8].

where K_2 is the *second-order anisotropy constant*. For $\psi = 0$, the total energy profile E is plotted as a function of θ for different applied fields (figure 4.3). As the field increases, the energy barrier Δ decreases and vanishes at the coercive field H_c. H_c is given by:

$$H_c(\psi) = \alpha \frac{2K_2}{\mu_0 M_s} \equiv \alpha H_A \qquad \text{(Equation 4. 1)}$$

with $\alpha = \left(\cos^{2/3}\psi + \sin^{2/3}\psi\right)^{-3/2}$ and the anisotropy field $H_A = 2K_2/\mu_0 M_s$. For $\psi = 0$ (the applied field is antiparallel to the initial magnetisation direction) $H_c = H_A$, *i.e.*, the theoretical coercive field H_c is equal to the anisotropy field H_A.

4.3. Coercivity in real materials

Experiments reveal that the measured coercive field in real systems is always inferior to the anisotropy field, $H_c << H_A$. This coercive field reduction with respect to values expected for coherent rotation, is referred to as "Brown's paradox" [4]. The explanation for Brown's paradox is the presence of structural defects (inhomogeneities). As a result of defects, reversal does not occur by coherent rotation. As proposed by Givord and Rossignol [1], the reversal process may be schematically divided into four steps corresponding to characteristic mechanisms. These mechanisms are the following (see figure 4.4):

- Nucleation: formation of an inverse domain and the emergence of a domain wall, at the defect where the anisotropy barrier is the lowest.

- Passage and expansion: passage of the domain wall from the defect to the principal phase (the domain wall energy increases because the intrinsic magnetic properties vary progressively from the defect region to the main phase) and expansion of the domain wall (the domain wall energy increases because its surface area increases). Passage/expansion into the main phase is a thermally activated process which is initiated in a finite volume known as the activation volume.

- Pinning and depinning: possible pinning and subsequent depinning of the domain wall on defects. Pinning may occur at defects in the main phase. In this case, depinning occurs through a process which is qualitatively similar to passage/expansion.

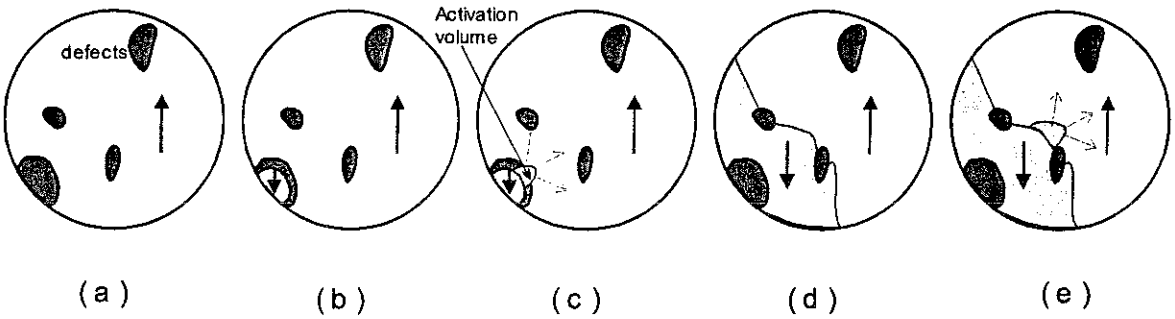

Figure 4. 4: Stages in magnetisation reversal bringing into play a critical volume v (or activation volume): (a) initial saturated state, (b) nucleation, (c) passage and expansion, (d) pinning and (e) depinning (≡ passage + expansion).

4.4. Models of coercivity in real materials

A quantitative description of the processes described in the above section requires in principle solving the micromagnetic equations describing the system. This includes solving complex differential equations. Except in very simple cases, these cannot be solved, neither analytically nor numerically. Approximate models are then used to describe magnetisation reversal. Two of these models will now be described.

4.4.1. Micromagnetic model

In the *micromagnetic model*, schematic descriptions of structural defects are proposed which provide significance to the parameter α. This model aims at determining the external conditions of field and temperature required to produce magnetisation reversal in a critical region of a grain for a given mechanism. Whatever the magnetisation process involved, the energy barrier is proportional to the magnetocrystalline anisotropy energy of the main phase [5, 6, 9-11]. The relation between the coercive field and the anisotropy field is expressed as:

$$H_c = \alpha_M H_A \qquad \text{(Equation 4. 2)}$$

In relation (4.2), the value of the parameter α_M depends, on the one hand, on the characteristic behaviours of the critical defects for coercivity, and, on the other hand, on the exact mechanism determining reversal.

For the analysis of experimental data, dipolar interactions must be taken into account. The equation used to analyse coercivity is then:

$$\frac{H_c}{M_s} = \alpha_M \frac{H_A}{M_s} - N_{eff} \qquad \text{(Equation 4. 3)}$$

In this relation, the first term represents the coercive field reduction ($\alpha_M < 1$) resulting from defects and the second term describes dipolar interactions, with N_{eff} being a phenomenological parameter representing the dipolar field. By plotting H_c / M_s as a function of H_A / M_s, one derives α_M and N_{eff}.

4.4.2. Global model

The *global model* supposes that the critical phenomenon in magnetisation reversal is the formation of a non-uniform magnetic configuration. A domain wall constitutes a non-uniform configuration of minimum energy. Therefore, the energy brought into play is the domain wall energy in the region of the grain concerned. It is additionally assumed that this energy is proportional to that of the domain wall energy inside the hard phase [1, 12-14]. Based on these assumptions, the coercive field is expressed as:

$$H_c = \alpha_G \frac{\gamma_w}{v^{1/3}\mu_0 M_s} - N_{eff} M_s - \frac{\Delta_{act}}{\mu_0 v M_s} \qquad \text{(Equation 4. 4)}$$

where γ_w is the domain wall energy within the main phase, and v is the activation volume. Δ_{act} is the thermally activated energy barrier. Note that thermal activation is usually neglected in the micromagnetic model, whereas strictly speaking it should be considered as well. In equation (4.4), M_s and γ_w are characteristic parameters of the main phase, and v and Δ_{act} are deduced from magnetic viscosity measurements (see section 4.4.3 below). In essentially the same procedure as above, α_G and N_{eff} are then deduced from:

$$\frac{H_0}{M_s} = \alpha_G \frac{\gamma_w}{v^{1/3}\mu_0 M_s^2} - N_{eff} \qquad \text{(Equation 4. 5)}$$

where $H_0 = H_c + 25S_v$ is the coercive field corrected for thermal activation effects.

4.4.3. Thermal activation energy and activation volume

Over a large range of time, the energy barrier Δ_{act} can be expressed as [15, 16]: $\Delta_{act} = k_B T \ln(t/\tau_0)$; where k_B is the Boltzman constant, t is time (second), τ_0 ($\approx 10^{-11}$ s) is the characteristic time for magnetisation reversal in case of no energy barrier. In the range of times accessible to usual experiments (1 s $\leq t \leq 10^4$ s), $\ln(t/\tau_0) \approx 25$, thus:

$$\Delta_{act} \approx 25 k_B T . \qquad \text{(Equation 4. 6)}$$

One may show that the activation volume may be expressed as [14, 16, 17]:

$$v = \frac{k_B T}{\mu_0 S_v M_s} \qquad \text{(Equation 4. 7)}$$

where S_v is the magnetic viscosity coefficient. S_v is equal to:

$$S_v = \frac{S}{\chi^{irr}} = \frac{dM / d\ln(t)}{\chi^{irr}} \qquad \text{(Equation 4. 8)}$$

where χ^{irr} is the irreversible susceptibility (see section 4.6.3) and S is the magnetic viscosity, $S = d(M)/d(\ln(t))$ [14, 17, 18].

4.4.4. Global model in case of second order anisotropy only

In the case where second order anisotropy only is involved, the domain wall energy, γ_w, and the domain wall width, δ_w, are related through [2, 3]:

$$\gamma_w = \frac{4\pi A}{\delta_w} \qquad \text{(Equation 4. 9)}$$

where A is the exchange constant (see in more detail in section 4.6.1).

Additionally, it is usually observed that $v \propto \delta_w^3$, which can be related to the fact that the formation of the activation volume is reminiscent of domain wall formation. Thus in equation (4.9) δ_w may be replaced by $v^{1/3}$ and relation (4.5), using (4.7) becomes:

$$\frac{H_0}{M_s} = \alpha'_G \frac{A}{v_a^{2/3}\mu_0 M_s^2} - N_{eff} \qquad \text{(Equation 4. 10)}$$

In equation (4.10), the activation volume is implicitly introduced through the experimental parameter v. The only parameters representing the main phase are M_s and A. Unlike usual assumption (section 4.4.3), it is not a priori assumed that the activation volume anisotropy is proportional to the main phase anisotropy.

4.5. Determination of the second order anisotropy coefficient

The analyses of coercivity presented in section 4.4.1 and 4.4.2 requires the knowledge of the second order anisotropy or that of domain wall energy γ_w which is itself a function of K_2. In the case of the FePt alloys studied in this thesis, $K_2(T)$ was not known within the entire temperature range of interest [19]. We analysed magnetisation curves on polycrystalline sample to extract $K_2(T)$. Here we describe the process used [20].

Let's consider a system consisting of single-domain uniaxial magnetic particles and assume that the particle easy axes c are distributed around the direction z of main orientation. The angle between c and z is φ (see figure 4.2.b). The distribution of orientation can be written using a Gaussian function:

$$p(\varphi) = \frac{1}{\sigma\sqrt{2*\pi}} \exp\left(-\frac{\varphi^2}{2\sigma^2}\right) \qquad \text{(Equation 4. 11)}$$

where σ represents the full width at half maximum of the function, *i.e.*, it quantifies the crystallographic texture of the system. In a very well textured system, σ is small and in an isotropic system, σ is equal to π (180 °).

The distribution function of particles around an applied field H, $N(\psi,\varphi)$ is given by:

$$N(\psi,\varphi) = \int_{\alpha=0}^{2\pi} \sin(\psi)\, p(\varphi)\, d\alpha \qquad \text{(Equation 4. 12)}$$

where α is the orthogonal angle defined in figure 4.2.b. In two particular cases when the applied field H is parallel to z, the angles φ, ψ and α are linked through $\cos(\varphi) = -\sin(\psi)\sin(\alpha)$, and when H is perpendicular to z, $\cos(\varphi) = \cos(\psi)$.

Under the applied field H, the total energy of the system consists of the anisotropy energy $K_2 \sin^2(\theta)$, the Zeeman energy $-\mu_0 MH\cos(\psi-\theta)$ and the dipolar energy $\frac{1}{2}\mu_0 nM^2$ (n is the demagnetising coefficient of the grain along a particular axis). Assuming that the magnetisation of each particle is oriented in the same hemisphere as defined by the applied field, the total energy and magnetisation are:

$$E_T = K_2 \sin^2(\theta) - \mu_0 M_s H\cos(\psi-\theta) + \frac{1}{2}\mu_0 n M_s^2 \qquad \text{(Equation 4. 13)}$$

$$M_\psi = M_s \cos(\psi-\theta) \qquad \text{(Equation 4. 14)}$$

At equilibrium, $\partial E/\partial\theta = 0$ and θ can be deduced from:

$$\frac{\partial E_T}{\partial\theta} = 0 \Rightarrow \theta = \theta(\psi) \qquad \text{(Equation 4. 15)}$$

From relations (4.11) to (4.15), one derives:

$$M(H) = \frac{\int_0^{\pi/2} M_\psi(H) N(\psi) d\psi}{\int_0^{\pi/2} N(\psi) d\psi} \qquad \text{(Equation 4. 16)}$$

In the particular case where there is no demagnetising field energy involved, it is convenient to express the reduced magnetisation $m = M/M_s$ as a function of the reduced field $h = H/H_A$. The corresponding magnetisation curves are plotted in figure (4.3) for σ = 0°, 15°, 45°, and 180°, and for h along and perpendicular to z, respectively. The parallel and perpendicular magnetisation curves calculated for a given σ value become progressively more similar as σ increases from 0° (full alignment) to 180° (fully random orientation). Note that for σ = 180°, the remanent magnetisation equals to 0.5 M_s as it is well known.

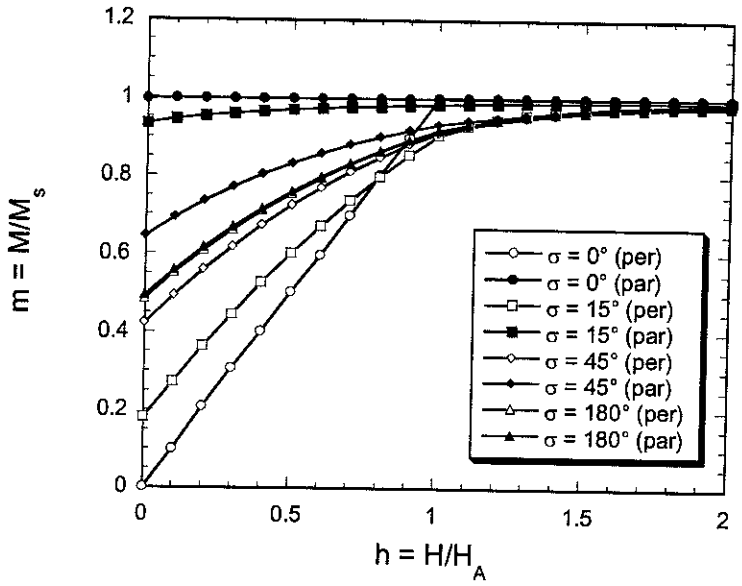

Figure 4.3: Magnetisation curves calculated from equation (4.16) with $\sigma = 0°$, 15°, 45°, and 180° when the applied field is parallel (denoted by "par") and perpendicular (denoted by "per") to the z-axis.

4.6. Coercivity analyses in FePt system

In this section, we firstly deduce $K_2(T)$ from 4 K – 700 K in FePt using the procedure described in section 4.5, then, we discuss coercivity in our FePt samples on the basis of the models described in section 4.4.

4.6.1. Determination of second order anisotropy constant K_2 and of the domain wall energy γ_w in FePt

Magnetisation curves were measured in the rolling plane – IP and perpendicular to this plane – PP (demagnetising correction with $N = 1$) in fields up to 10 T for the temperature range 4 K to 300 K and in fields up to 7 T for the temperature range 300 K to 700 K. These magnetisation curves are shown in figure 4.5.

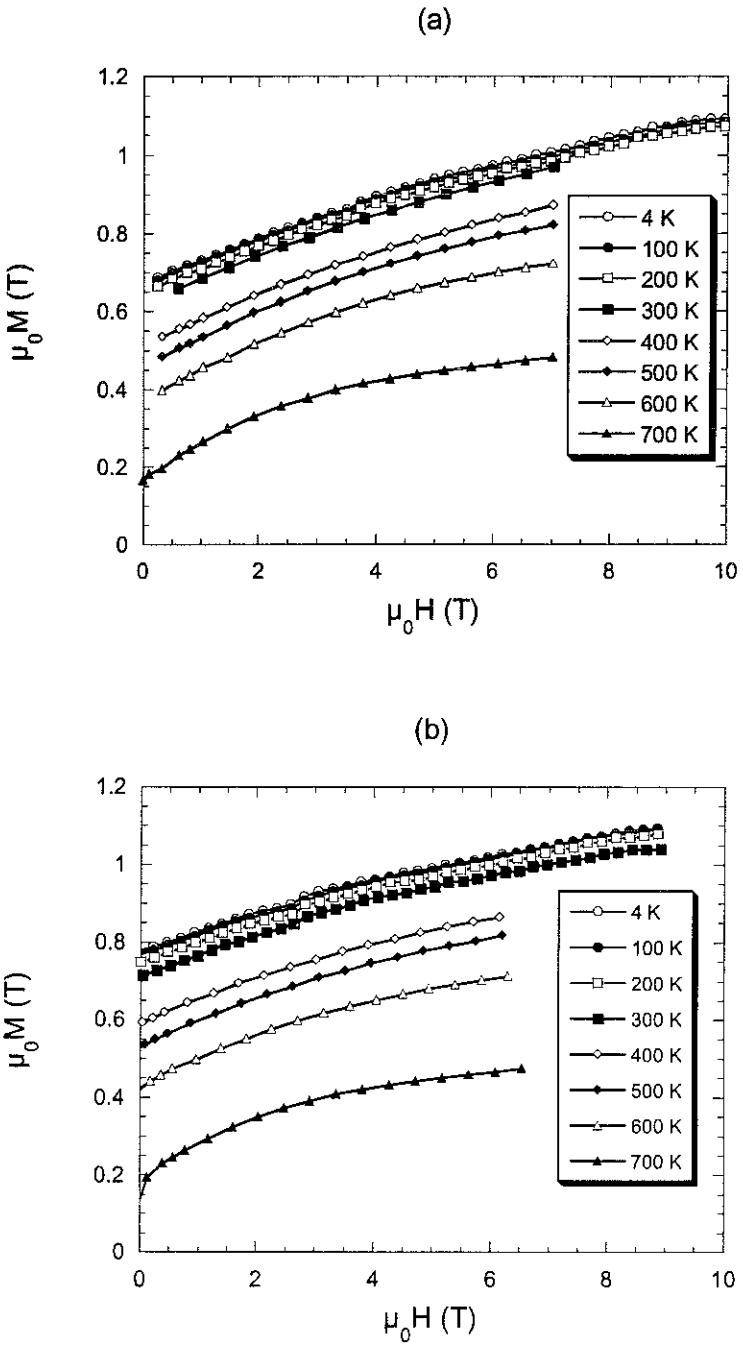

Figure 4. 5: Magnetisation curves at different temperatures of FePt measured (a) in the rolling plane and (b) perpendicular to this plane (demagnetising correction with $N = 1$).

At each temperature, the IP and PP magnetisation variations were fitted simultaneously using equation (4.16). The only free parameters were the second order anisotropy constant K_2 and the temperature independent parameter σ. $\sigma = 77°$ was obtained. This value represents weak PP texture. It is in qualitative agreement with XRD spectra (figure 2.11.a). The fitted magnetisation variations at 300 K are shown in figure 4.6. From $h = 0$ to $h = 0.55$, the agreement between calculated and experimental magnetisation curves is very satisfactory. At larger applied fields the calculated value of the magnetisation tends to be higher than the experimental one. This discrepancy may be tentatively attributed to higher order anisotropy terms neglected in our analysis. A very similar agreement between calculated and experimental magnetisations was obtained at other temperatures. $K_2(T)$ then deduced is plotted in figure 4.7. At 4 K, K_2 reaches 11 MJ/m^3, it decreases monotonously as T increases (at 300 K, K_2 = 7.9 MJ/m^3, in agreement with literature values [21]), and vanishes at 700 K. K_2 decreases faster than M_s as temperature is increased. From K_2, the domain wall energy may be calculated according to $\gamma(T) = 4\sqrt{A(T) \times K_2(T)}$, where it is assumed that second order anisotropy only is involved and where A is the exchange constant. $A(0) = 13.44 \times 10^{-12}$ J/m was deduced from $A(0) = k_B T_c / 2\sqrt{2}\xi$ (ξ is the interatomic distance between iron nearest neighbours) considering that $\xi = a\sqrt{2}/2$ = 2.723 Å, the lattice parameter a = 3.86 Å [22] and T_c = 750 K. $A(T)$ may be assumed to vary as $[M_s(T)/M_s(0)]^2$ [1]. The temperature dependence of the domain wall energy is plotted in figure 4.8.

In a system of local moments and in the classical limit, H. B. Callen and E. Callen [23] have shown that K_2 is expected to be a function of the reduced spontaneous magnetisation, $k_2 = \hat{I}_{5/2}\left(L^{-1}(m)\right)$ (equation 3.5), where $\hat{I}$ is the modified Bessel function, L is the Langevin function, $k_2(T) = K_2(T)/K_2(0)$ and $m(T) = M_s(T)/M_s(0)$. With this assumption, K_2 may be deduced at each temperature from M_s. $K_2(T)$ thus derived follows closely the experimentally deduced value (Figure 4.7). Thus FePt, a system in which the magnetic electrons are itinerant, follows a behaviour characteristic of local moment systems. Band structure calculations in this system [24] have shown that the intra-atomic interactions largely dominate the inter-atomic ones resulting in a quasi-local moment character of these alloys.

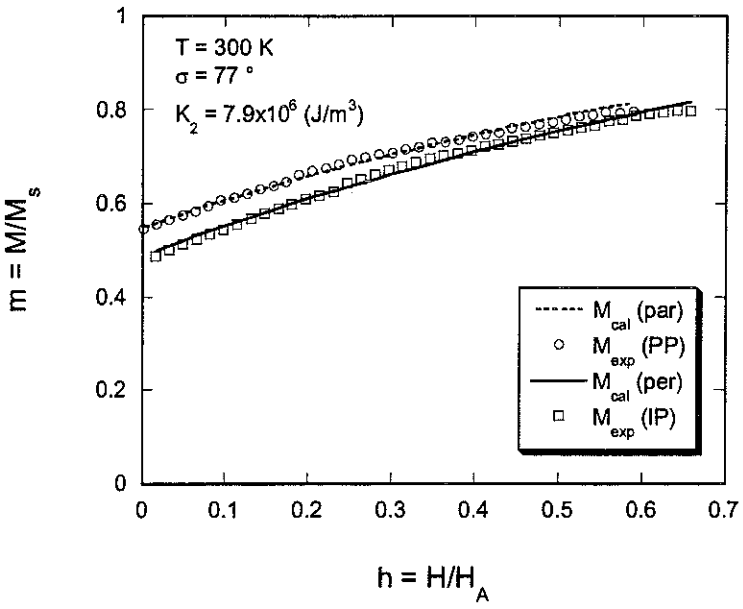

Figure 4. 6: Some representative results calculated for FePt using equation (4.16) with σ = 77°, K_2 = 7.9 MJ/m^3 compared to experiment $M(H)$ at room temperature data.

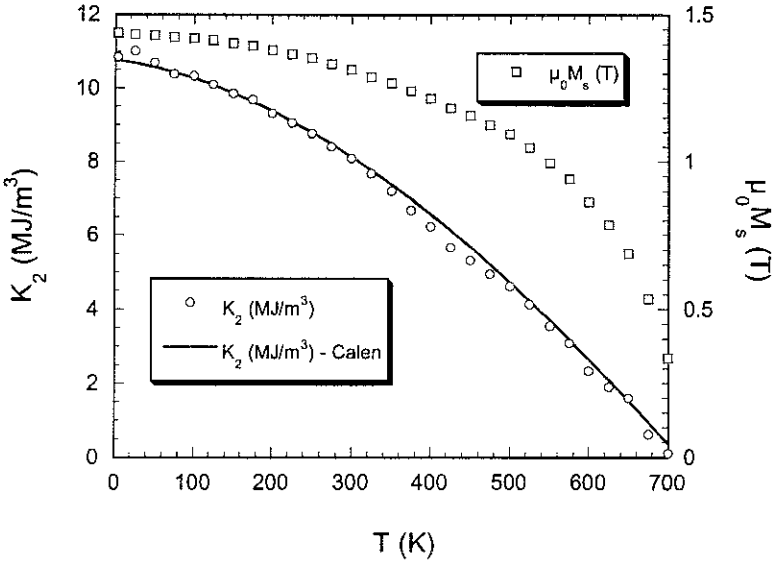

Figure 4. 7: Temperature dependence of the saturation magnetisation M_s (open squares), the second order anisotropy constant K_2 of FePt deduced from simultaneous fitting of the IP and PP magnetisation curves (open circles), and K_2 calculated from the local-moment model (solid line) [23].

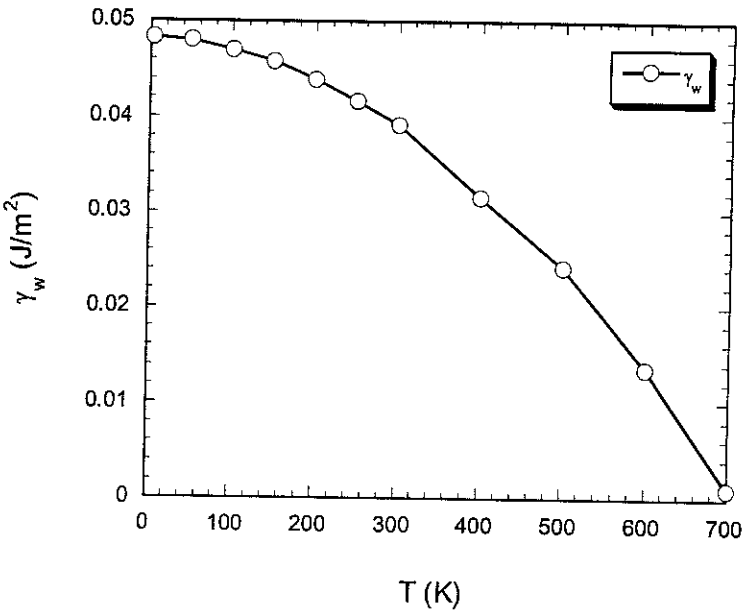

Figure 4. 8: Temperature dependence of the domain wall energy $\gamma_w = 4\sqrt{AK_2}$ of FePt.

4.6.2. Measurement of the temperature dependence of the coercive field

At each temperature the coercive field H_c was deduced as the maximum of χ^{irr} on the IP hysteresis cycle. The temperature dependence of H_c between 4 K and 700 K is shown in figure 4.9.

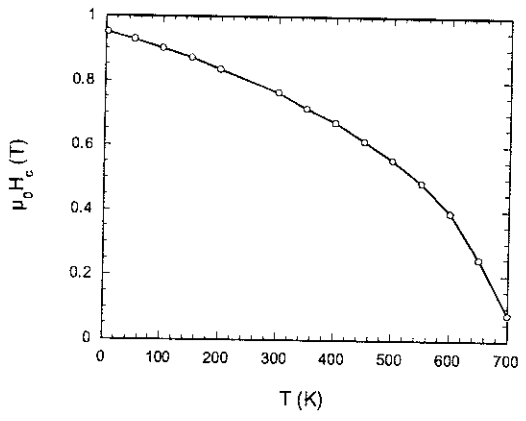

Figure 4. 9: Temperature dependence of the coercive field $\mu_0 H_c$ in $L1_0$ FePt foil.

4.6.3. Viscosity measurements

The analysis of coercivity within the global model requires the determination of the activation volume v (see expressions 4.5 and 4.10). For the FePt alloy prepared by sheath-rolling, viscosity measurements were conducted in the temperature range 4 – 700 K. A representative result at room temperature is shown in figure 4.10. The decay of magnetisation follows an exponential law. From these plots, the magnetic viscosity S and the magnetic viscosity constant S_v were obtained by using equation (4.8).

The irreversible susceptibility χ^{irr} was determined from the total susceptibility χ^{tot} and the reversible susceptibility χ^{rev} by: $\chi^{irr} = \chi^{tot} - \chi^{rev}$. χ^{rev} was derived from the slope of the reversible recoil magnetisation curve: $\chi^{rev} = \partial M^{rev} / \partial H$. For each temperature, five or six reversible recoil curves were taken around the coercive field value by increasing the negative field to zero. The procedure is illustrated in figure 4.11, where the hysteresis cycle and some recoil curves (open circles) are shown. It is worth noting that χ^{rev} (solid squares) is much smaller than χ^{irr} (solid circles).

The field dependence of the irreversible susceptibility χ^{irr} was obtained in the temperature range 4 K – 600 K (figure 4.12).

At each temperature, the magnetic viscosity S was measured for 4 – 5 different field values. The field variation of the viscosity $S(H)$ mimics that of $\chi^{irr}(H)$ (figure 4.13 shows representative results at 400 K). The temperature dependence of the viscosity coefficient $S_v(T)$ and the activation volume $v(T)$ deduced from the usual expression (4.8) are plotted in figure 1.14.

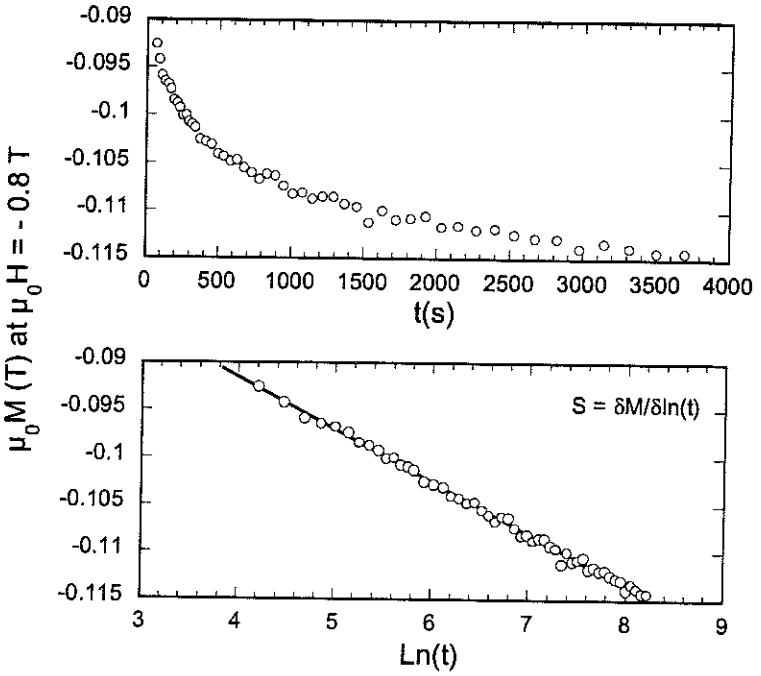

Figure 4. 10: Time decay of the magnetisation of the FePt foil in the presence of a negative constant magnetic field ($\mu_0 H$ = - 0.8 T) at room temperature (a) linear scale and (b) Ln scale.

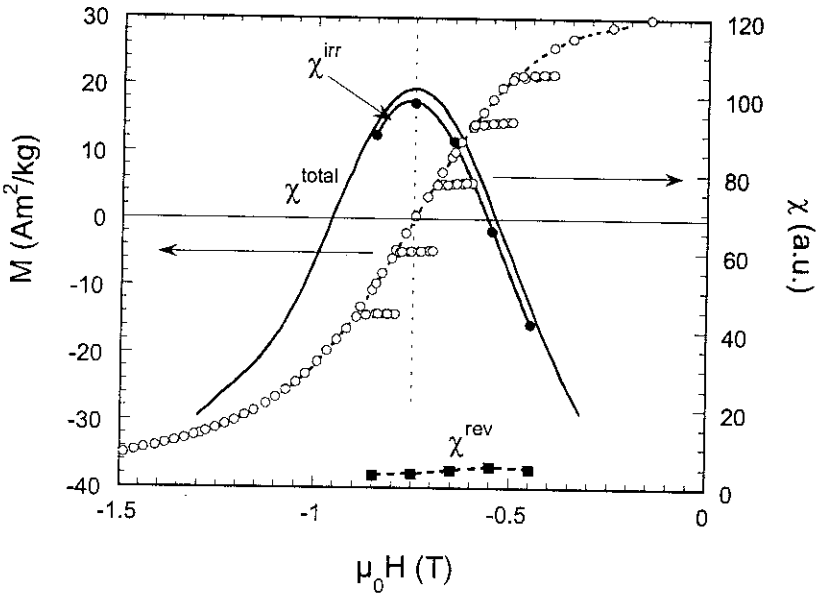

Figure 4. 11: Irreversible susceptibility χ^{irr} is determined from total susceptibility χ^{tot} and reversible susceptibility χ^{rev} by: $\chi^{irr} = \chi^{tot} - \chi^{rev}$; reversible susceptibility is given from recoil curve.

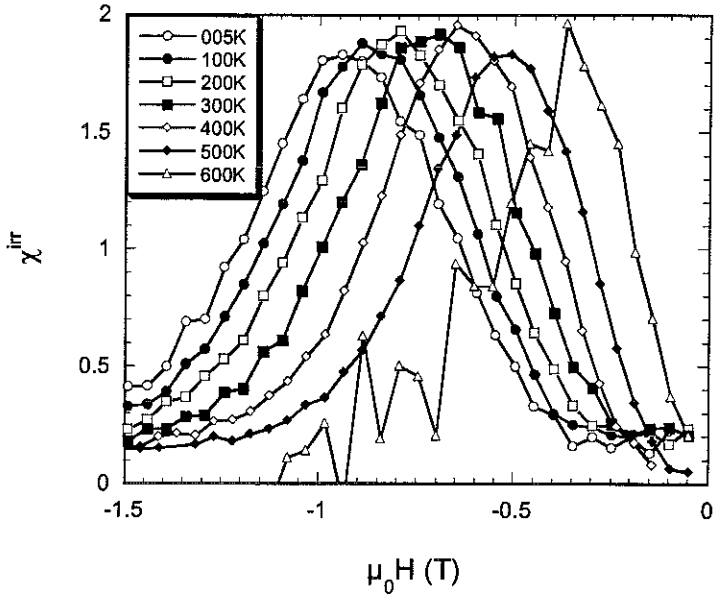

Figure 4. 12: Applied field dependence of the irreversible susceptibility χ^{irr} of the FePt sample at the temperature range 5 K – 600 K.

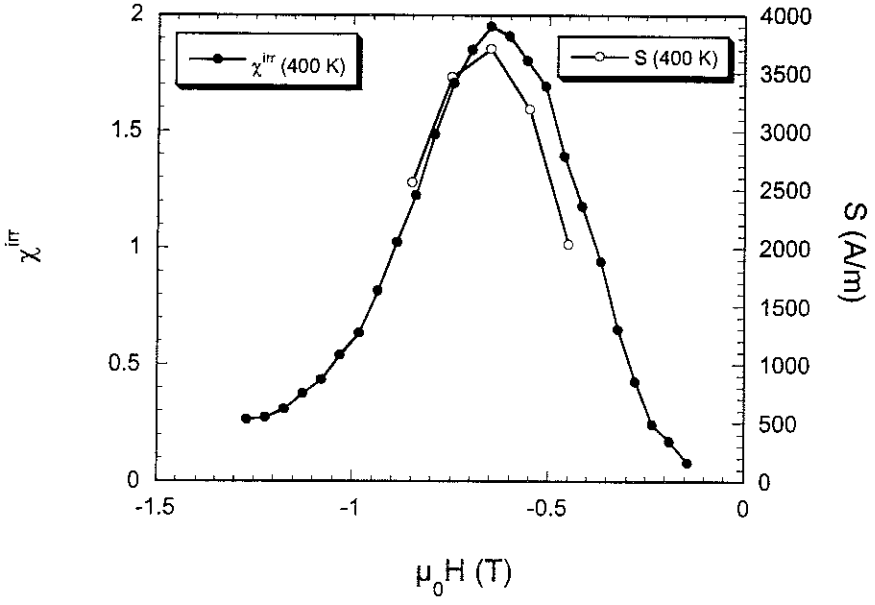

Figure 4. 13: Field dependence of the irreversible susceptibility and viscosity.

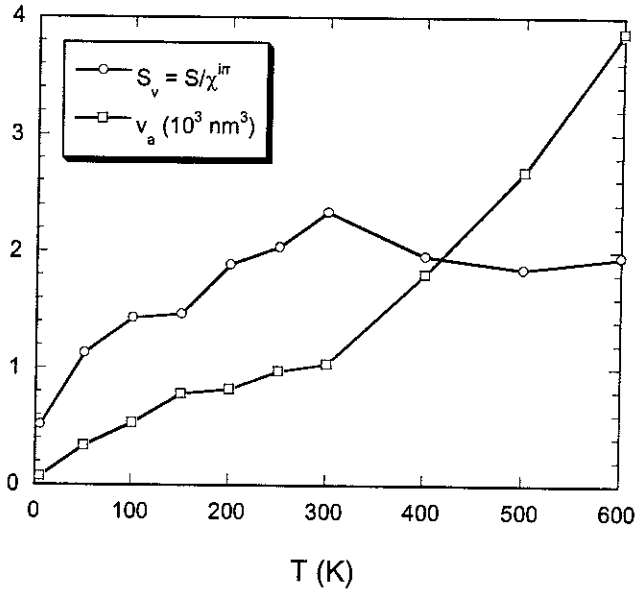

Figure 4. 14: Temperature dependence in the temperature range 5 K – 600 K of the magnetic viscosity S, magnetic viscosity constant S_v, and activation volume v_a, deduced from the after-effect measurements and the recoil curves.

4.6.4. Discussion of $H_c(T)$

The temperature dependence of the anisotropy field H_A is compared to that of H_c in figure 4.15. It is striking that H_c varies less with temperature than the anisotropy field, while the opposite has been observed in other high performance magnets in which coercivity is mainly due to magnetocrystalline anisotropy.

The coercive field $H_c(T)$ in FePt was analysed within the micromagnetic model described in section (4.4.1). H_c / M_s is plotted in figure (4.16.a) as a function of H_A / M_s. An approximate linear variation is obtained from which $\alpha_M = 0.03$ and $N_{eff} = -0.27$ are derived.

To test the applicability of the global model, H_0 / M_s was plotted as a function of $\frac{\gamma}{v^{1/3} \mu_0 {M_s}^2}$ (figure 4.16.b). An approximately linear variation is again obtained. The parameter values obtained are $\alpha_G = 0.06$ and $N_{eff} = -0.38$.

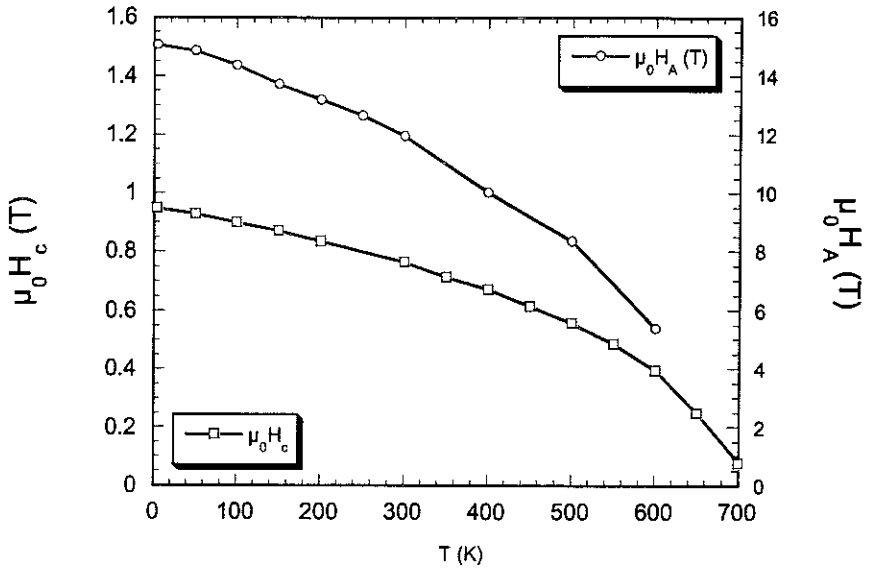

Figure 4. 15: Temperature dependence of the anisotropy field $\mu_0 H_A$ is compared to that of the coercive field $\mu_0 H_c$ in $L1_0$ FePt foil.

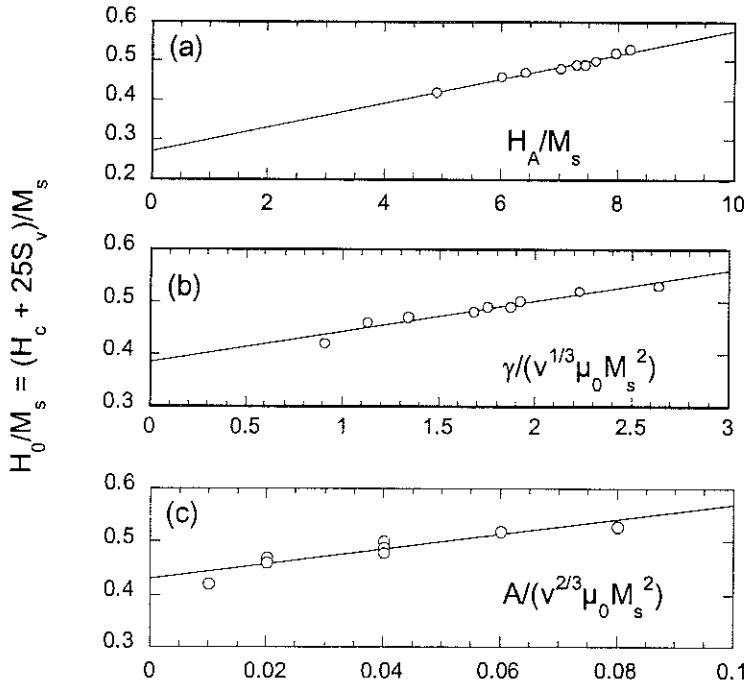

Figure 4. 16: Coercivity analysis within the framework of (a) the micromagnetic (b) the global and (c) the modified global model.

Finally, within the modified global model (expression 4.10), we obtained α'_G = 1.42 and N_{eff} = -0.43.

The value of the parameters α_M, α_G, and α'_G are significantly smaller than those obtained in other optimally processed hard materials, *e. g.*, $Nd_2Fe_{14}B$, Sr-Ferrites, etc... [3, 14]. Considering the fact that α represents the influence of defects on coercivity and that larger α values correspond to better magnetic properties, this result suggests that higher coercive field values could be reached by optimising further the preparation procedure of the FePt foils. This is in agreement with the fact that very large room temperature coercive fields of 4 T were recently reported for a thin film sample consisting of isolated epitaxial nanosized grains of FePt [25].

The N_{eff} values, deduced from the curves in figure 4.16, are between -0.27 and -0.42. In other hard magnetic systems, the parameter N_{eff} is usually positive (see 8.79 for $Nd_2Fe_{14}B$ or 17.09 for Sr-Ferrites) [14], which implies that the dipolar interactions are added to the applied magnetic field to favour magnetisation reversal. On the contrary, in the present case the dipolar interactions contribute to coercive field enhancement. This suggests that a sizeable contribution to the coercive field is due to shape-like anisotropy. The decrease of H_c with temperature is slower than that of K_2 (figure 4.15). In general, the temperature dependence of the coercive field is more rapid in systems where the coercive energy barrier is due to magnetocrystalline anisotropy than in systems where it is due to shape anisotropy. This is directly linked to the fact that $K_2(T)$ varies approximately as $M_s^3(T)$. Thus the corresponding H_A varies as M_s^2 whereas the demagnetising field is expected to vary as M_s. Thus the reduced thermal variation of H_c in FePt is consistent with the fact that a substantial fraction of the coercive field is due to demagnetising field effects (shape anisotropy).

4.6.5. Discussion of the activation volume

We have already mentioned that in several hard magnetic materials $v(T)$ is approximately proportional to $\delta^3(T)$. In figure (4.17), $v(T)$ in FePt is plotted as a function of $\delta^3(T)$. A linear variation is observed, but the corresponding line does not cross the origin of the axes. We have not been able to interpret this behaviour.

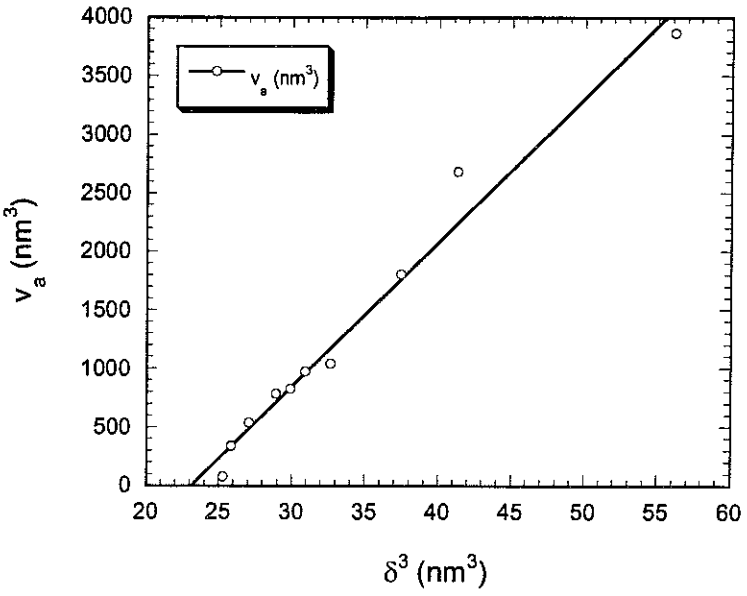

Figure 4. 17: Domain wall thickness (δ) dependence of the activation volume (v) in $L1_0$ FePt foil.

4.7. In-plane versus perpendicular-to-plane hysteresis cycle in $L1_0$ FePt

Hysteresis cycles were also measured in the PP configuration. The PP and IP hysteresis cycles at 300 K are compared in figure 4.18. The PP coercive field, H_c^{PP}, is weaker than the IP coercive field (figure 4.19), H_c^{IP}. $\Delta H_c = H_c^{IP} - H_c^{PP}$ decreases from 0.13 T at 4 K to 0.9 at 300K (figure 4.20).

These differences in coercive field values may be ascribed either to differences in the magnetisation reversal process itself or to differences in dipolar field values. As mentioned in chapter 2, TEM observations (figure 2.13) of our samples suggest that the FePt crystallites are platelets aligned with the foil plane. Assuming that coercivity involves some sort of pinning between cristallites, the pinned surface area is expected to be larger in the IP configuration than it is in the PP ones and consistently the coercive field is expected to be larger. A similar conclusion was drawn by Dempsey *et. al.* in analysing coercivity of $Sm_2Fe_{17}N_{3-\delta}$ irradiated films [26].

Alternatively, the above differences between IP and PP coercive fields may be related to the anisotropic character of dipolar interactions in such heterogeneous magnetic systems. In general, the demagnetising field is expected to vanish with the mean magnetisation, $< M >$ and thus the dipolar field not to depend on the applied field orientation. However, large distributions of local dipolar interactions exist in heterogeneous systems, which implies that the dipolar field does not vanish everywhere within the sample. To first order, the width of the dipolar field distribution is expected to be proportional to the dipolar field strength itself. Thus, in the PP configuration, the dipolar field should deviate more from its mean value, than it does in the IP configuration. Magnetisation reversal is nucleated at some location where the dipolar field combine with the applied field to reduce further the coercive barrier. It is expected to be less in the PP configuration.

Selection between these alternative interpretations may be obtained from $H_c(T)$ curves. In case the coercive field reduction is due to modifications in the reversal process, $H_c(T)$ should decrease less as temperature is increased in the PP configuration than it does in the IP configuration (see relations (4.3), (4.5) and (4.10)). On the opposite, in case the coercive field reduction is due to demagnetising field effects, $H_c(T)$ should decrease less in the IP configuration. As shown in Figure 4.19, the former applies.

Figure 4.18 reveals additionally that, in the applied field range in which magnetization reversal occurs and after usual demagnetising field corrections, dM/dH is larger for PP measurements than it is for IP ones. The dipolar interactions acting on a given grain include contributions from the grain itself and contributions from the environment. Assuming that the moments within each individual grain are aligned along their easy direction, only contributions from the environment may depend on the magnetisation state and thus on the direction of the applied field.

To first order, the dipolar interactions created by the surrounding grains on a given grain of magnetisation M_S may be expressed in terms of the dipolar field :

$$H_{dip}^{\alpha} = -N_b^{\alpha} < M > + N_g^{\alpha} < M > \qquad \text{(Equation 4. 17)}$$

The first term in (4.17) represents the bulk demagnetising field and the second term represents the cavity field, the sign +, respectively -, indicates that the magnetisation is parallel, respectively antiparallel, to $< M >$. N_b^{α} is the bulk demagnetising field coefficient, N_g^{α} is the

grain self-demagnetising field, and $< M >$ is the foil mean magnetisation. The index α refers to the magnetisation orientation: α is // for IP magnetisation, it is $\perp$ for PP magnetisation. Assuming $N_b^{//} = 0$ and $N_b^{\perp} = 1$, $H_{dip}^{//} = N_b^{//} < M >$ and $H_{dip}^{\perp} = (1 - N_b^{\perp}) < M >$ is deduced. The difference in the slopes observed on the hysteresis cycles, after usual bulk demagnetising field corrections indicate that $N_g^{\perp} > N_g^{//}$. This may be related to TEM observations which suggest that the FePt nanograins have anisotropic shape, being elongated in the foil plane.

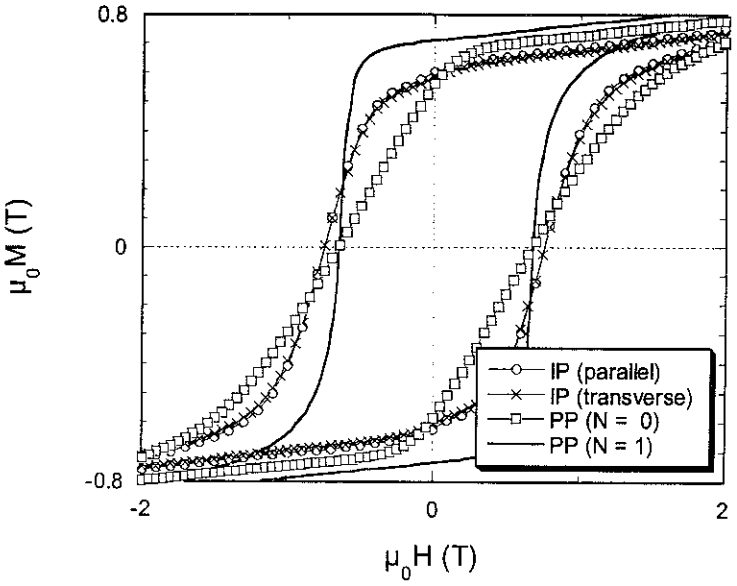

Figure 4. 18: In-plane IP and perpendicular-to-plane PP hysteresis cycles at 300 K of the FePt sample.

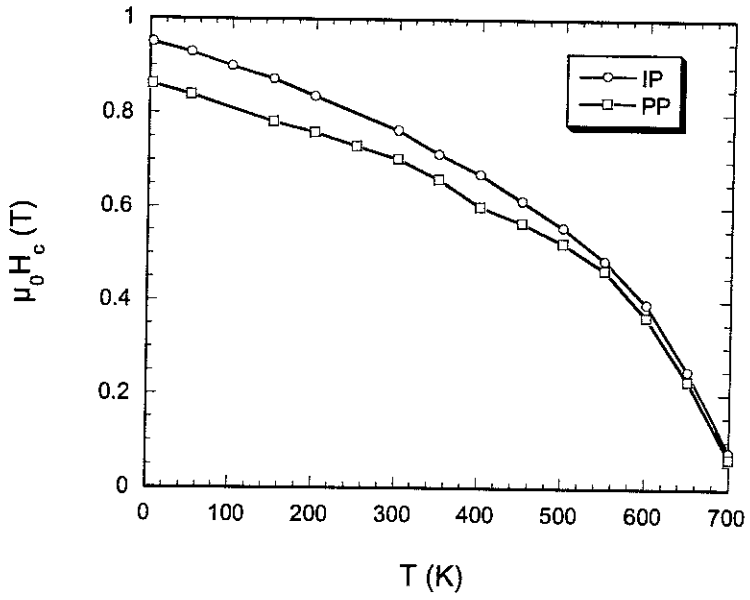

Figure 4. 19: Temperature dependence of the IP and PP coercive field of the hard FePt foil.

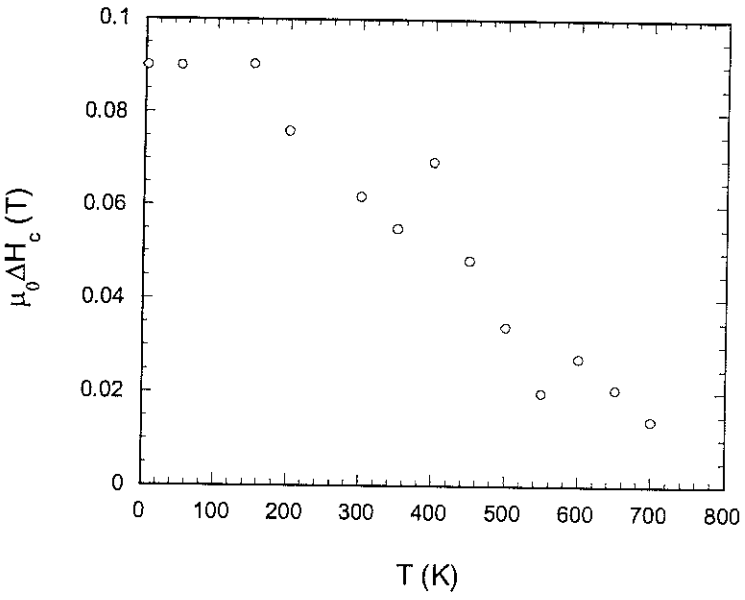

Figure 4. 20: Temperature dependence of the difference between IP coercivities and PP coercivities of the FePt foil.

4.8. Magnetisation reversal in the Fe-rich FePt

4.8.1. Magnetisation reversal in Fe-rich FePt system

In chapter 2, we described the preparation of the Fe-rich FePt sample (FePt/Fe_3Pt nanocomposites) by cyclic rolling of Fe and Pt foils, down to the nanometre range. The respective amount of Fe and Pt was chosen in such a way that, after annealing, 65 % (in volume percent) of the hard FePt $L1_0$ fct phase and 35% of the soft Fe_3Pt $L1_2$ fcc phase were formed. The respective amount of the Fe and Pt in atomic percent is $Fe_{66}Pt_{34}$. Accordingly, the XRD patterns revealed the coexistence of the fct FePt phase and the fcc Fe_3Pt phase (figure 2.10). The hysteresis cycles measured with the field applied respectively in-plane (IP) and perpendicular to the foil plane (PP) are shown in figure 4.20. It is striking that the IP cycle shows two-step reversal whereas the PP cycle does not. A sample was cut in such a way that the demagnetising field coefficients along one direction of the foil plane and perpendicular to the plane were identical, equal to 0.2 according to the calculation [27] (sample dimensions are x×y×z = 0.8×0.25×0.8 mm^3). The hysteresis cycles, measured along x and z are shown in figure 4.21. Although the bulk demagnetising field coefficients are identical along these two measurement directions, the two hysteresis curves remain very different. As shown in the next section, the differences between the two hysteresis curves may be linked to the anisotropy of the dipolar interactions within matter itself related to the specific foil-structure of the rolled sample.

4.8.2. Dipolar interactions in two-phase decoupled magnetic systems

In magnetically heterogeneous composite materials large dipolar interactions may be present. Let us consider an assembly of soft and hard grains and assume that they are exchange decoupled (figure 4.22). The hard phase coercive field is assumed to be much larger than the applied field and the hard phase magnetisation M_{hard} is assumed to be saturated and equal to the spontaneous magnetisation M^s_{hard}. Assuming that the dipolar interactions can be represented by uniform fields, through usual demagnetising field coefficients, the dipolar interactions on soft grains, E_{dip} may be expressed as:

$$E_{dip} = \frac{1}{2}N_g\mu_0 M_{soft}^2 - \frac{1}{2}N_g\mu_0\alpha M_{soft}^2 - N_g\mu_0(1-\alpha)M_{soft}M_{hard} + \frac{1}{2}N_b\mu_0\alpha M_{soft}^2 + N_b\mu_0 M_{soft}(1-\alpha)M_{hard} \quad \text{(Equation 4. 18)}$$

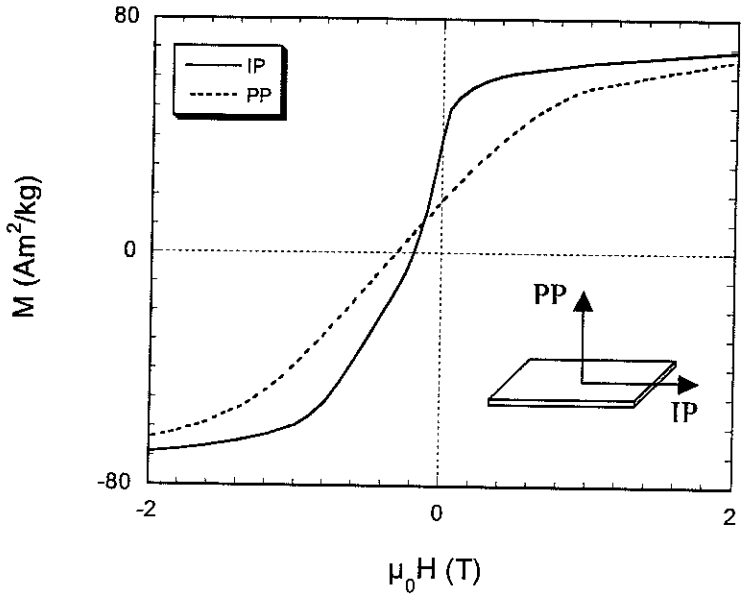

Figure 4. 21: Room temperature IP and PP magnetisation curve of the FePt/Fe_3Pt composite (foil).

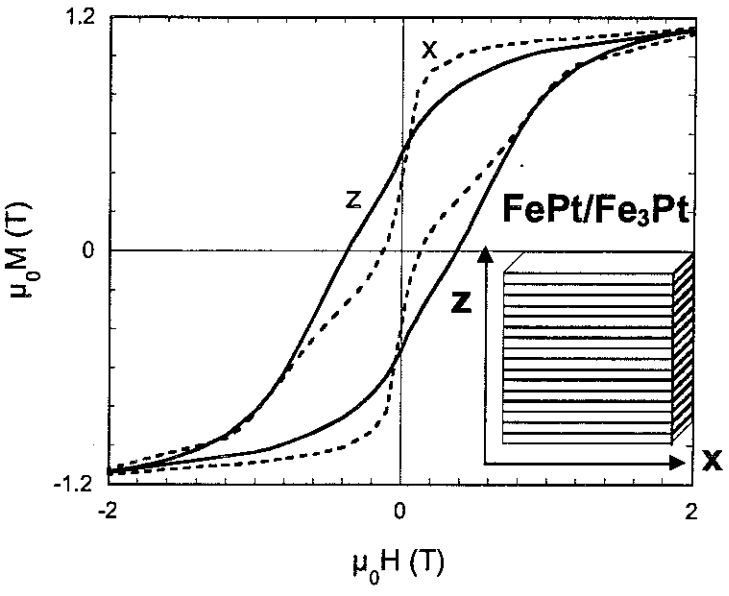

Figure 4. 22: Room temperature magnetisation curve of the FePt/Fe_3Pt composite. The applied field is along the rolling plane (x-axis) and perpendicular to the rolling plane (z-axis). Sample (inset) has the same macroscopic demagnetising factors along the x- and z-axis.

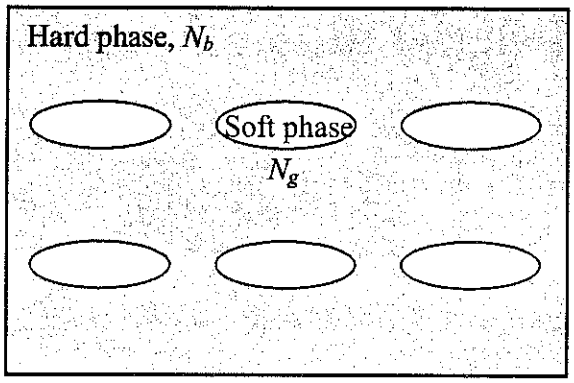

Figure 4. 23: Grains of soft material in a matrix of hard material

In relation (4.18), M_{soft} is the soft phase magnetisation. The first term represents the self-demagnetising field, the two following terms come from the cavity field and the two last terms represent the bulk demagnetising field. All soft grains are assumed to be identical, with individual grain demagnetising field coefficient N_g. N_b is the bulk demagnetising field

coefficient and α represents the fraction of soft phase within the sample. Under H, the Zeeman energy is:

$$E_{Zeeman} = -\mu_0 M_{soft} H$$

And the total energy is:

$$E_T = E_{dip} + E_{Zeeman} \qquad \text{(Equation 4. 19)}$$

Energy minimization with respect to M_{soft} leads to:

$$M_{soft} = \frac{[(N_g - N_b)(1-\alpha)M_{hard} + H]}{\alpha N_b + (1-\alpha)N_g} \qquad \text{(Equation 4. 20)}$$

The resulting total dipolar field acting on the soft grains is:

$$H_{dip} = N_g(1-\alpha)(M^s_{hard} - M_{soft}) - N_b\left((1-\alpha)M^s_{soft} + \alpha M_{soft}\right) \qquad \text{(Equation 4. 21)}$$

To emphasize the influence of dipolar interactions within matter, let us assume that $N_b = 0$. As a direct result of heterogeneity, the susceptibility is not infinite during soft phase reversal. The soft phase spontaneous magnetisation M^s_{soft}, being larger than M^s_{hard}, reversal starts at positive applied field value $H = N_g(1-\alpha)(M^s_{soft} - M^s_{hard})$. In zero applied field, $M_{soft} = M^s_{hard}$ minimizes the density of magnetic poles within matter, *i.e.*, there is no remanence enhancement. In negative applied field, the dipolar field created by the hard magnetic grains dominates over the dipolar field of soft grains and opposes to magnetisation reversal. Reversal is completed at $|H| = N_g(1-\alpha)(M^s_{soft} + M^s_{hard})$. The magnetisation variation is fully reversible, thus justifying the expression "dipolar spring". Figure 4.23 shows the total magnetisation curves with N_g = 0, 1/3, and 1 (N_b = 0). In these calculations, we assumed that the hard and soft magnetisations are 1.4 and 1.8 T, volume fraction of the soft phase α = 0.35.

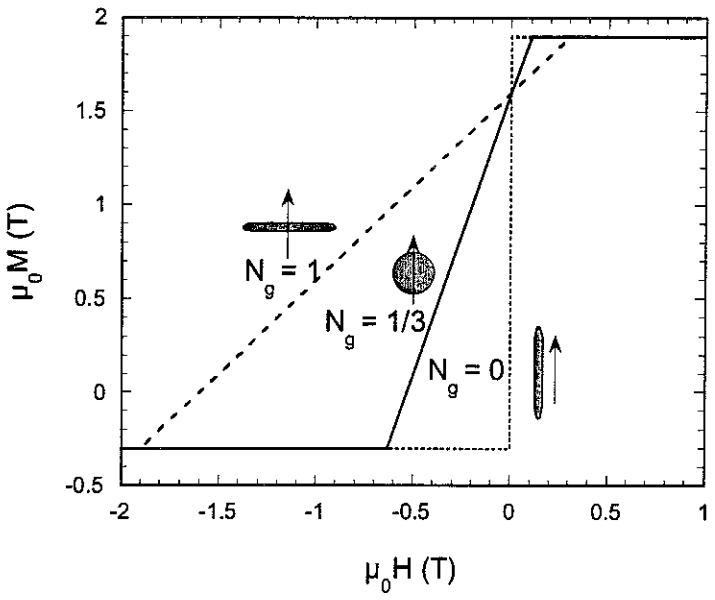

Figure 4. 24: Reversal of the soft phase with the demagnetising field coefficient N_g = 0, 1/3, 1 (N_b = 0). When $N_g \neq 0$, the reversal starts at a positive applied field and finishes at a negative field, which are depend on value of N_b.

4.8.3. Dipolar-spring concept applied to FePt/Fe_3Pt

To quantitatively model reversal in Fe-rich FePt samples, we assumed (i) that magnetisation reversal of the hard phase was identical to the one observed in equiatomic FePt and (ii) that soft-phase magnetisation reversal in the absence of dipolar interactions could be represented by the simple phenomenological function (figure 4.24). The IP and PP magnetisation variations were then fitted by assuming that the soft-phase magnetisation variation follows expression (4.20). The calculated curves are compared in figure 4.25 to the experimental ones. The agreement is excellent. Free parameters in this analysis were the soft phase fraction α and the demagnetising field coefficient N_b and N_g. α = 0.35 was obtained in exact agreement with the value corresponding to the sample stoichiometry ($Fe_{66}Pt_{34}$). N_b = 0.16 compares to 0.2 deduced from the sample dimensions [27]. N_g = 0.9 corresponds to very flat Fe_3Pt crystallites, indicating that the layer shape of the initial foils is preserved in the alloy obtained by annealing.

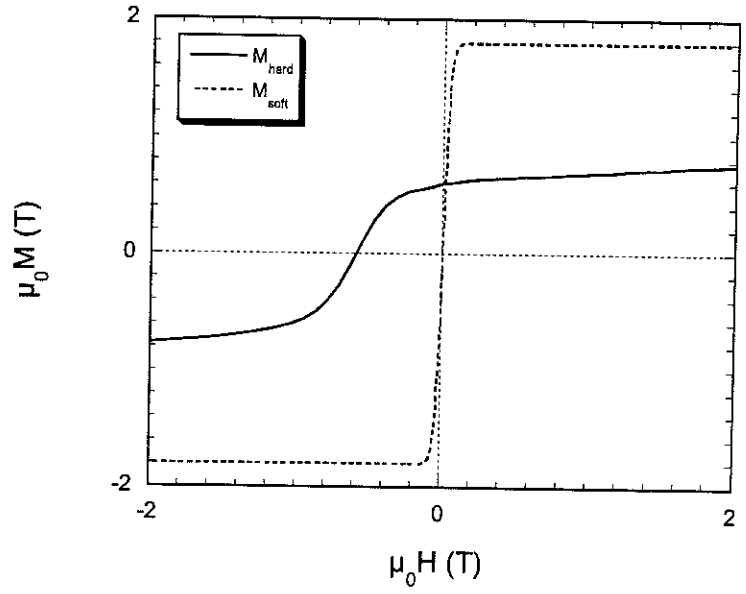

Figure 4. 25: Magnetic reversals of the soft and hard phase are used for calculation. Soft-phase curve reversal is represented by a simple function, typical of soft-phase material. Hard phase curve is identical to the one observed in equiatomic FePt.

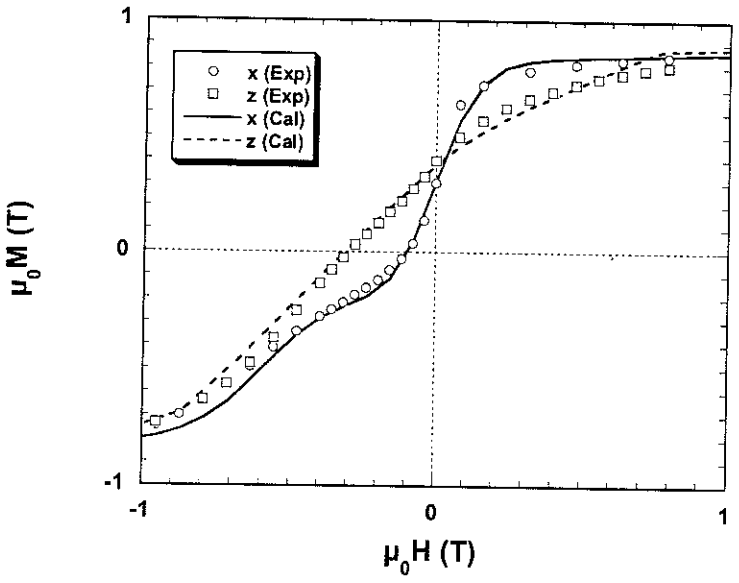

Figure 4. 26: Comparison between experimental data (open circles and open squares) of magnetisation reversals of the FePt/Fe_3Pt composite and values calculated from expression 4.20.

References

1. Givord, D. and M.F. Rossignol, *Coercivity*, in *Rare-earth ion permanent magnets*, J.M.D. Coey, Editor. (1996), Clarendon Press: Oxford. p. 218.
2. Barthem, V.T.M.S., D. Givord, M.F. Rossignol, and P. Tenaud, *An approach to coercivity relating coercive field and activation volume.* Physica B, **319** (2002) 127.
3. Givord, D., M. Rossignol, and V.T.M.S. Barthem, *The physics of coercivity.* J. Magn. Magn. Mater., **258-259** (2003) 1.
4. Brown Jr, W.F., *Virtues and Weaknesses of the Domain Concept.* Rev. Mod. Phys., **17** (1945) 15.
5. Abraham, C. and A. Aharoni, *Linear Decrease in the Magnetocrystalline Anisotropy.* Phys. Rev., **120** (1960) 1576.
6. Aharoni, A., *Reduction in Coercive Force Caused by a Certain Type of Imperfection.* Phys. Rev., **119** (1960) 127.
7. Stoner, E.C. and E.P. Wohlfarth, *A Mechanism of Magnetic Hysteresis in Heterogeneous Alloys.* Phil. Trans. Roy. Soc., **240A** (1948) 599.
8. du Trémolet de Lacheisserie, E., *Magnétisme*, **1**. (2000), Presses Universitaires de Grenoble: Greonoble. p. 203.
9. Kronmuller, H., Phys. Stat. Sol., **144** (1987) 385.
10. Kronmuller, H., K.D. Durst, and G. Martinek, *Angular Dependence of the Coercive Field in Sintered $Fe_{77}Nd_{15}B_8$ Magnets.* J. Magn. Magn. Mater., **69** (1987) 149.
11. Kronmuller, H., K.D. Durst, S. Hock, and G. Martinek, *Micromagnetic analysis of the magnetic hardening mechanisms in RE-Fe-B magnets.* J. de Phys., **C8** (1988) 623.
12. Givord, D., A. Lienard, P. Tenaud, and T. Viadieu, *Magnetic viscosity in Nd-Fe-B sintered magnets.* J. Magn. Magn. Mater., **67** (1987) L281.
13. Givord, D., M.F. Rossignol, V. Villas-Boas, F. Cebollada, and J.M. Gonzalez. *Time dependent effects in magnetization processes.* in *Proceedings of the 9th International Workshop on Magnetic Anisotropy in Rare Earth - Transition Metal Alloys.* (1998) Sao Paulo, Brazil: World Scientific (Singapore). 21.
14. Givord, D., P. Tenaud, and T. Viadieu, *Coercivity mechanism in ferrite and rare earth transition metal sintered magnets ($SmCo_5$, Nd-Fe-B).* IEEE Trans. Magn., **24** (1988) 1921.
15. Street, R. and J.C. Wooley, Proc. Phys. Soc. (London), **62A** (1949) 562.
16. Gaunt, P., Phil. Mag., **34** (1976) 775.
17. Wohlfarth, E.P., *The coefficient of magnetic viscosity.* J. Phys. F: Met. Phys., **14** (1984) L155.
18. Gaunt, P., *Magnetic viscosity and thermal activation energy.* J. Appl. Phys., **59** (1986) 4129.
19. Yermakov, A.Y. and V.V. Maykov, *Temperature dependence of magnetic crystallographic anisotropy and spontaneous magnetisation of single crystal of FePd and CoPt alloys.* Phys. Met. Metall., **69** (1990) 198.

20. Tenaud, P., *Analyse experimentale des mechanismes de coercitivite dans les aimants Nd-Fe-B frittes*, Thesis in *Physique* (1988), Université de Joseph Fourier - Grenoble 1: Grenoble. p. 159.

21. Sun, S., C.B. Murray, D. Weller, L. Folks, and A. Moser, *Monodisperse FePt nanoparticles and ferromagnetic FePt nanocrystal superlattices.* Science, **287** (2000) 1989.

22. Villars, P. and L.D. Calvet, *Pearson's Handbook of Crystallographic Data for Intermetallic Phases.* (1985), Metals Park, OH: American Society for Metals.

23. Callen, H.B. and E. Callen, *The present status of the temperature dependence of magnetocrystalline anisotropy, and the l(l+1)/2 power law.* J. Phys. Chem. Solids., **27** (1966) 1271.

24. Podgórny, M., *Electronic structure of the ordered phases of Pt-Fe alloys.* Phys. Rev. B, **43** (1991) 11300–11318.

25. Shima, T., K. Takanashi, Y.K. Takahashi, and K. Hono, *Preparation and magnetic properties of highly coercive FePt films.* Appl. Phys. Lett., **81** (2002) 1050.

26. Dempsey, N.M., X.L. Rao, J.M.D. Coey, J.P. Nozières, M. Ghidini, and B. Gervais, *Coercive $Sm_2Fe_{17}N_3$: A model pinning system created by heavy ion irradiation.* J. Appl. Phys., **83** (1998) 6902.

27. Chen, D.-X., E. Pardo, and A. Sanchez, *Demagnetising factors of rectangular prisms and ellipsoids.* IEEE Trans. Magn., **38** (2002) 1742.

Chapter 5: Magnetostrictive $SmFe_2$ prepared by hydrostatic extrusion

Résumé en français

Chapitre 5 : Couches magnétostrictives $SmFe_2$ préparées par extrusion hydrostatique

La magnétostriction représente le changement de dimensions d'un matériau associé à ses propriétés magnétiques.

Les systèmes de forte anisotropie magnétocristalline sont caractérisés par la forme asphérique du nuage représentatif de la distribution des électrons magnétiques. Cette distribution anisotrope est couplée à la distribution, également anisotrope, des électrons de l'environnement, source du champ cristallin. Supposant le système rigide, la variation de l'énergie de couplage avec l'orientation des moments représente alors l'anisotropie d'origine magnétocristalline. Pour chaque orientation des moments, une déformation de la matière permet de minimiser un peu plus l'énergie de champ cristallin. La déformation n'est pas isotrope puisque le couplage ne l'est pas. La différence de déformation entre deux directions est la magnétostriction dite de Joule.

Les composés RFe_2, où R est un atome de terres rares, peuvent présenter des magnétostrictions dites géantes qui sont associées au caractère fortement anisotrope de la distribution des électrons magnétiques des éléments de terres rares. Parmi ces systèmes, le composé $SmFe_2$ présente la plus importante des magnétostrictions négatives (raccourcissement selon la direction d'aimantation).

Dans le cadre de cette thèse, nous avons abordé la préparation de feuilles magnétostrictive de $SmFe_2$ par co-déformation de feuilles de Sm et Fe, suivie d'un recuit approprié entraînant la co-diffusion des éléments constitutifs et la réaction de formation de la phase cubique $SmFe_2$.

Ce travail faisait suite à un travail préliminaire de A. Giguère. Par extrusion hydrostatique, celui-ci avait préparé des assemblages dans lesquels les épaisseurs individuelles des feuilles étaient de 85 µm et 60 µm respectivement. Il avait montré que la phase désirée se formait par recuit. Il avait mesuré des magnétostrictions de – 860 ppm à température ambiante.

Grâce à un traitement de recuit initial des feuilles, nous avons pu réduire par extrusion les épaisseurs des feuilles jusqu'à des valeurs de l'ordre de 20-30 μm (Sm) et 5-10 μm (Fe). A la suite d'un recuit à 600 °C pendant 5 heures, l'échantillon était pratiquement monophasé. La formation de la phase de Laves cubique par traitement thermique à une température aussi basse est en soi un résultat original. Les mesures magnétiques ont permis de révéler une certaine texture des échantillons, mais celle-ci n'a pu être pleinement comprise. La magnétostriction mesurée présente un caractère nettement anisotrope. Sa valeur la plus grande est mesurée selon une direction perpendiculaire à la direction d'extrusion, elle vaut -1280 ppm à température ambiante.

Le composé intermétallique $SmFe_2$ est extrêmement fragile mécaniquement et il ne peut être usiné. La préparation de feuilles selon la voie que nous avons utilisée peut permettre d'obtenir des objets qui à la suite d'opérations simples de coupes auraient les formes requises pour les mises en œuvre désirées.

Chapter 5: Magnetostrictive $SmFe_2$ prepared by hydrostatic extrusion

5.1. Introduction

5.1.1. What is magnetostriction?

Magnetostriction is the changing of a material's physical dimensions associated to its magnetism. Volume magnetostriction at an atomic level results from the fact that the exchange interactions are sensitive to the interatomic distances. Joule magnetostriction corresponds to a distortion of the material linked to the direction of its magnetisation.

5.1.2. Magnetostrictive materials

Magnetostrictive effects were first discovered in nikel [1]. Following this, other transition metals such as cobalt, iron and alloys of these materials were found to also show significant magnetostrictive effects with strains of about 50 ppm (1 ppm = 10^{-6}).

Subsequently, the rare earth metals were shown to possess extraordinary magnetostrictive properties in the early 1960's by Legvold *et. al.* [2] and Clark *et. al.* [3]. Magnetostriction is as high as about 10^4 ppm at low temperatures for single crystal Dy. However the ordering temperature of the rare earth elements is below room temperature so that application of this is limited. E. Callen pointed out that there was a great promise in study of the magnetostrictive properties of rare earth – transition metal intermetallics, where the strong magnetism of the transition metals could increase the rare earth magnetic order at high temperatures [4]. N. C. Koon *et. al.* [5] and A. E. Clark and H. S. Belson [6] independently reported giant room temperature magnetostrictive strains of the order of 10^3 ppm in RFe_2 Laves phase compounds, which have a $MgCu_2$-type cubic lattice of space group Fd3m (C15 Laves phase). For applications, one needed to reduce the magnetic anisotropy of these alloys to improve the low field magnetostrictive properties. U. Atzmony and co-workers reported spin reorientation in $Ho_xTb_{1-x}Fe_2$ and other ternary alloys [7]. That work opened a route to reduce magnetic anisotropy by replacing a portion of Tb with other rare earth elements. The resulting alloy

$Tb_{1-x}Dy_xFe_2$ (commercially known as Terfenol-D) is at present the most widely used magnetostrictive material. Terfenol is capable of strains as high as 1500 ppm and, since the 1980's, has been a commercially available material for various applications [8-10]. In the rest of this chapter, we focus on the magnetostriction of the rare earth – transition compounds.

Table 5.1: The saturation magnetostriction of iron and some of its compounds.

Material	Crystal axis	Saturation magnetostriction ($\times 10^{-6}$)	References
Fe	100	+(11-20)	[11]
Fe	111	-(13-20)	[11]
Fe	Polycrystal	-8	[11]
$SmFe_2$	Polycrystal	- 1560	[12]
$TbFe_2$	Polycrystal	2520	[12]
$Tb_{0.5}Dy_{0.5}Fe_2$	Polycrystal	1100	

5.1.3. Mechanism of magnetostriction in Rare Earth – Transition compounds

The mechanism of magnetostriction in Rare Earth – Transition compounds is schematised in figure 5.1. The environment assumed to be initially cubic is shown in (5.1.a). The easy magnetisation direction of the rare earth atoms is assumed to be along the cube diagonal (5.1.b and 5.1.c). The anisotropic 4f electron cloud interacts with the positive charges in the environment resulting in the distortion shown in (5.1.b), which details the case of the quadrupole moment $\alpha_J > 0$, *i.e.* the magnetisation is along the long direction of the electron cloud (*e.g.* Sm). In this case, the cubic structure contracts along the magnetisation direction and the magnetostriction is said to be negative. Figure (5.1.c) details the case of $\alpha_J < 0$ (*e.g.* Tb), the magnetostriction is positive.

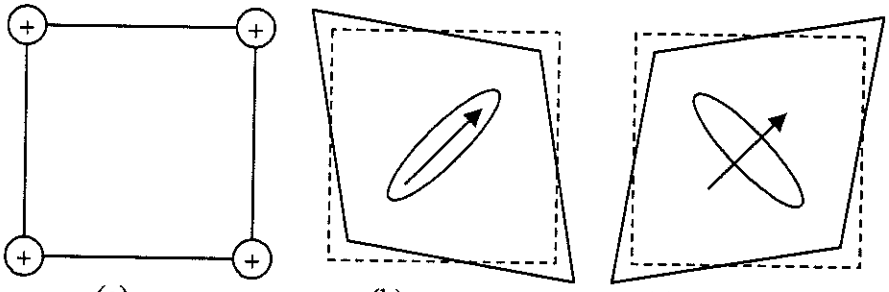

Figure 5.1: Schematic illustration to explain Joule magnetostriction in rare earth containing compounds (a) The initial cubic charge environment (b) Distortion resulting from the Joule magnetostriction when $\alpha_J > 0$ and (c) $\alpha_J < 0$.

5.1.4. Magnetostriction coefficients

In single crystalline cubic materials, magnetostriction is presented by coefficient of magnetostriction λ_i, which can be phenomenologically written as [13]:

$$\frac{\delta l}{l} = \frac{2}{3}\lambda_{100}\left(\alpha_1^2\beta_1^2 + \alpha_2^2\beta_2^2 + \alpha_3^2\beta_3^2 - \frac{1}{3}\right) + 3\lambda_{111}\left(\alpha_2\alpha_3\beta_2\beta_3 + \alpha_3\alpha_1\beta_3\beta_1 + \alpha_1\alpha_2\beta_1\beta_2\right) + \ldots$$

(Equation 5. 1)

where λ_{100}, λ_{111} are the magnetostriction coefficient along <100> and <111> direction; α denote the direction cosines of the magnetisation with respect to the crystal axes; β the direction cosines of the measurement direction with respect to the crystal axes. The saturation magnetostriction is defined as:

$$\lambda_s = (2/5)\lambda_{100} + (3/5)\lambda_{111} \qquad \text{(Equation 5. 2)}$$

In isotropic material ($\lambda_{100} = \lambda_{111}$), it is denoted that $\lambda_{//}$ and $\lambda_{\perp}$ are the change in length of specimen a field applied parallel and perpendicular to the measurement direction. Saturation magnetostriction of isotropic polycrystals is then defined as:

$$\lambda_s = 2/3(\lambda_{//} - \lambda_{\perp}) \qquad \text{(Equation 5. 3)}$$

5.1.5. Magnetic properties of $SmFe_2$

Among RFe_2 compounds, $SmFe_2$ has highest measured value of negative magnetostriction. Figure 5.2 shows the iron-samarium phase diagram [14]. The diagram reveals an eutectic point at 720 °C for the composition 72.5 atomic % Sm. Below 720 °C, the equilibrium state consists of $SmFe_2$ and α-Sm. Thus, it is possible to produce $SmFe_2$ through diffusion. $SmFe_2$ has a cubic lattice constant of a = 0.7415 nm [15]. Studies on single crystalline specimens have shown that $SmFe_2$ has a ferrimagnetism and the magnetisation at room temperature and Curie temperature are 60 Am^2/kg and 670 K, respectively [16]. At room temperature, magnetic moment of this compound is along the <111> crystallographic direction, and there is a spin reorientation at about 200 K, where magnetic moments rotate to <110> direction [17-19]. Saturation magnetostriction of -1560 ppm at 300 K for polycrystalline $SmFe_2$ was reported [20].

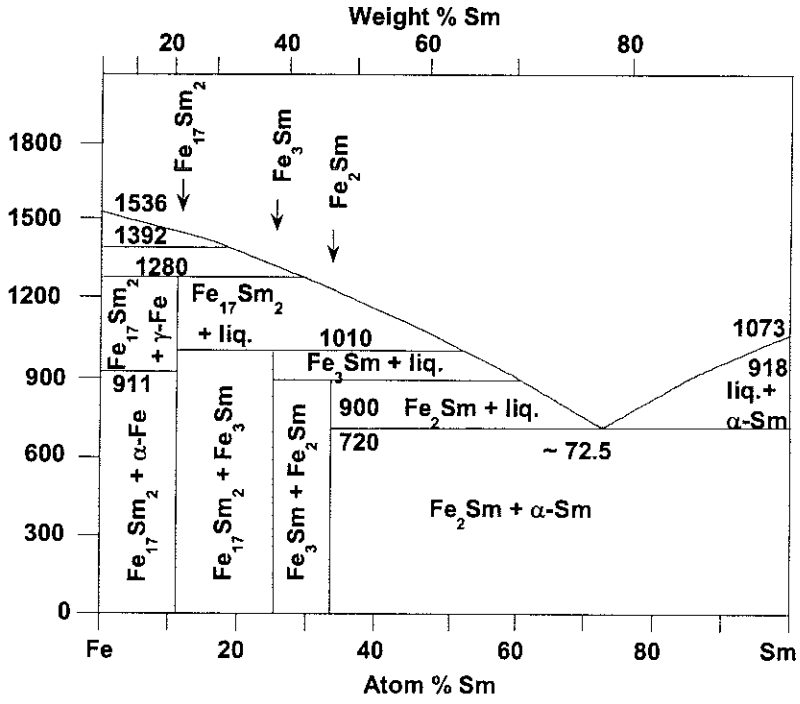

Figure 5.2: Iron-Samarium phase diagram [14].

From the torque curve of a single crystal of $SmFe_2$, the second and fourth anisotropy constants at room temperature, K_2 and K_4, were respectively determined to be -5.3×10^5 and 1.9×10^5 J/m^3 [21]. The room temperature λ_{111}, was highest and value reached – 2010 ppm, whereas, λ_{100} was – 130 ppm. The saturation magnetisation, λ_s was – 1258 ppm which is less than that obtained from polycrystalline specimens [8].

Polycrystalline $SmFe_2$ has been prepared by standard bulk processing techniques [18-20], where Sm and Fe metals are mixed by melting and then annealed in the temperature range 700 °C – 850 °C. In the melt spinning method, the molten metal was quenched onto a rotating copper roll and then compacted and heated at 700 °C/ 600 seconds to obtain $SmFe_2$ phase [22]. Single crystals were produced by the self-flux method, in which molten mixture of Sm and Fe was very slowly solidified (0.4 °C/1 hour) [21]. Our work aimed to prepare $SmFe_2$ by co-deformation of Sm and Fe foils followed by a diffusion controlled growth of the intermetallic phase by suitable annealing. The process is described in the following section.

5.2. Preparation of $SmFe_2$ by extrusion

5.2.1. Preliminary work at laboratory Louis Néel

$SmFe_2$ was firstly prepared by hydrostatic extrusion in the work of A. Giguère thesis [23, 24]. Preparation of $SmFe_2$ by extrusion is an overlap between this thesis and Giguère's thesis. In Giguère's thesis, the starting foils of Sm (250 μm) and Fe (150 μm) were reduced by a factor of about 3 after one extrusion cycle. The hydrostatic extrusion process is described in section 1.3.1. The Table 5.2 presents some parameters of Sm, Fe and $SmFe_2$ alloy. Further deformation was impossible because sample became very brittle. Layer thickness of Sm and Fe after extrusion was about 85 and 60 μm, respectively.

Giguère focused on the diffusion process of Sm/Fe during annealing. It was studied by XRD, SEM and magnetisation characterization. It was revealed that when annealed at 525 °C for 5 hours, a zone 30 μm thick of $SmFe_2$ phase was formed through diffusion process. Magnetisation measurements along different axes of sample produced by annealing Sm/Fe at 550 °C/ 12 hours hinted at <111>

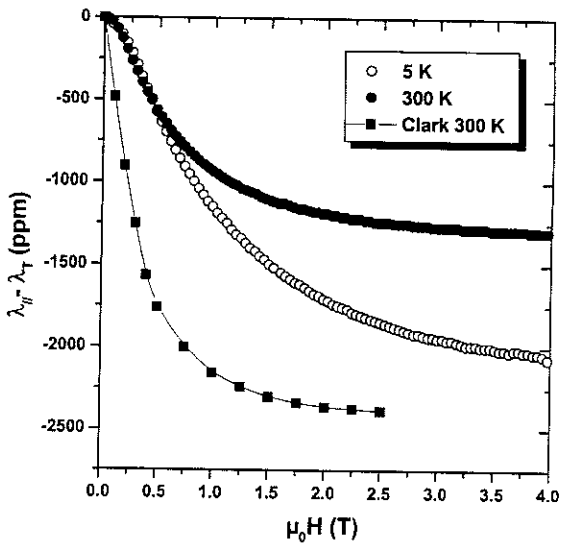

Figure 5.3: $\lambda_{//} - \lambda_{\perp}$ of $SmFe_2$ produced by annealing 1 extrusion cycle Sm/Fe multilayer at 550 °C/ 12 hours at low and room temperature compared with the polycrystalline sample [22].

texture along the extrusion direction in this sample. The saturation magnetostriction constant λ_s, measured along extrusion direction, was –860 and –1300 ppm at 300 K and 5 K, respectively. These values are much lower than that of the polycrystalline $SmFe_2$ [8] (figure 5.3).

In this thesis, we improve the extrusion process to get Sm/Fe multilayers with smaller layer thicknesses. Firstly, we reduced the annealing temperature for stress relief after each extrusion (400 °C), and then we conducted three extrusion cycles. Details of the extrusion process are presented in the following section.

Table 5. 1: Some physical properties of Sm, Fe, $SmFe_2$ alloy and some experimental conditions.

	Sm	Fe	$SmFe_2$
Crystallographic structure, lattice parameter (nm)	Rhombohedral, a = b = 0.362, c = 0.262	Face-centred cubic, a = 0.287	Laves phase, a = 0.742
Atomic weight	150.36	55.85	262.06
Density (g/cm^3)	7.35	7.87	
Melting point (°C)	1072	1538	
Purity (%)	99.9	99.5	
Starting thickness (μm)	250	150	
Initial annealing	400 °C/1 hour	700 °C/ hour	

5.2.2. Work realised during this thesis

The extrusion process that was used to produce Sm/Fe was described in section 1.3.1. Starting commercial samarium (250 μm) and iron (150 μm) foils with purity of 99.9 and 99.5 % were annealed at 400 °C and 700 °C for 1 hour, respectively (see table 5.1). The width and length of the foils were 7 and 25 mm, respectively. The relative thickness of the Sm and Fe foils (250:150) corresponds to an atomic ratio 36.5:63.5, which is slightly off stoichiometry with respect to $SmFe_2$ (33.3:66.7).

Ten bilayers of Sm/Fe wrapped in an iron foil (thickness = 50 μm) (this iron wrap was used to protect the sample during chemical attack) were stacked and loaded into an Al billet, then extruded through three successively smaller dies. There was a heat treatment for stress relief at 400 °C/1 hour under vacuum of about $10^{-4} - 10^{-5}$ mbar between two consecutive extrusions. This temperature is high enough for stress relief but low enough to prevent significant diffusion. After three extrusions (one extrusion cycle), the Al billet was eliminated by chemical attach with NaOH. Sample, then, was cut into pieces for submitting to the next extrusion cycle.

Up to three cycles were conducted for Sm/Fe multilayer. The fact that, this sample could be deformed more than previous sample of A. Giguère can be attributed to lower annealing temperature in this sample (400 °C) than in previous one (450 °C).

5.3. Structure analysis

Up to three extrusion cycles were carried out (C1, C2 and C3), reducing the foil thickness of Sm and Fe to some tens of μm (Fig. 5.4.a-c). Further extrusions were not possible as the samples became brittle. The limitation of deformation multilayer Sm/Fe (in comparison with the deformation of Fe/Cu or Fe/Ag down to nanometre scale [25, 26]) and the fact that interface Sm/Fe is more jagged than that in the Fe/Ag can be ascribed to the rhombohedral crystalline structure of Sm and a certain amount of $SmFe_2$ formed at the interface during annealing.

After 3 extrusion cycles, thickness of Sm and Fe was about 20-30 μm and 5-10 μm, respectively. The initial form was well preserved down to 2 cycles (C2) but it degraded when 3 cycles (C3) were applied (see Figure 5.4). Thus, annealing to form $SmFe_2$ was carried out on C2.

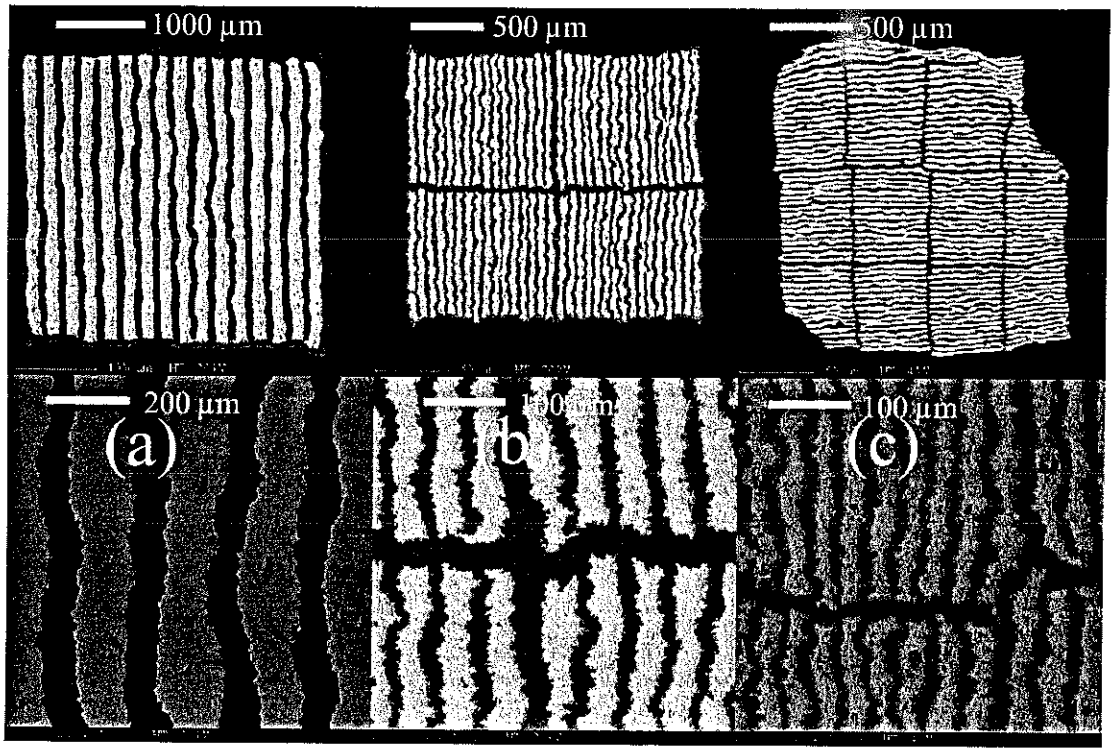

Figure 5.4: SEM images of the Sm/Fe multilayer after (a) one (C1), (b) two (C2), and (c) three extrusion cycles (C3).

5.3.1. SEM imaging

Extruded samples (C2) were annealed for diffusion. The formation of $SmFe_2$ with annealing at 600 °C/5 hours was followed by SEM observations. Figure 5.5 shows SEM images of this sample, they indicate that the diffusion between the Sm and Fe layers almost finished at that annealing condition. This fact is in agreement with the results obtained from diffusion study of Giguère. At the composition around 63 % Fe, which is the composition of our specimen, stoichiometric compositions $SmFe_3$, Sm_2Fe_{17} are not expected to be present but $SmFe_2$, (see the Sm-Fe phase diagram in figure 5.2).

There was some Sm left in the sample, which results from a slightly Sm rich content compared to the stoichiometric $SmFe_2$ composition. The remained iron in this figure comes from the protective Fe wrap.

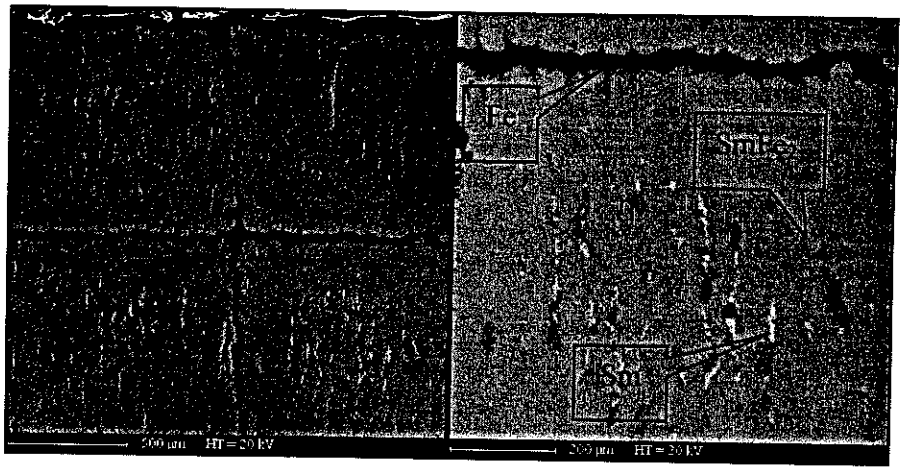

Figure 5.5: SEM images of C2 annealed at 600 °C for 5 hours.

5.3.2. X-ray diffraction patterns

XRD analysis of a powder sample obtained by crushing an extruded and annealed sample (C2 annealed at 600 °C/5 hours), is given in figure 5.6. All strong reflections are characteristic of the $SmFe_2$ phase. There is no significant reflection from Sm or Fe. Amount of remained Sm is too small to be detected by the XRD measurement. This also indicates that the formation of $SmFe_2$ was almost complete after this heat treatment. Formation of the phase at such a low temperature ($SmFe_2$ is normally processed at temperatures above 700°C) is advantageous as the evaporation of Sm is limited.

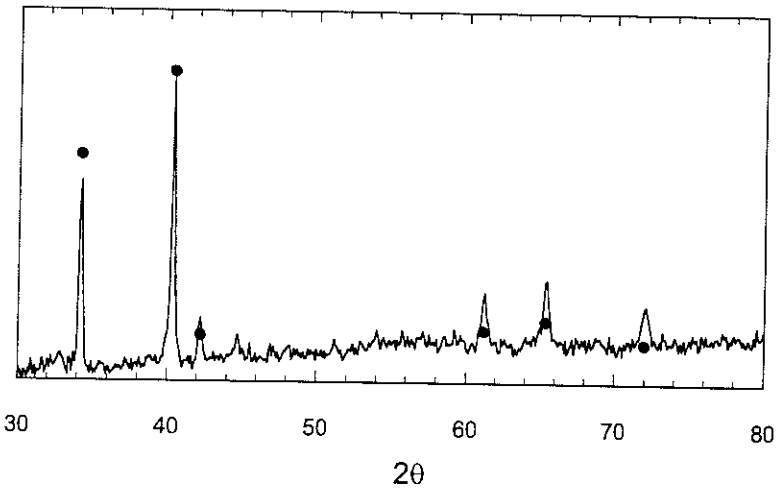

Figure 5.6: XRD patterns of a powder sample obtained by crushing the annealed sample (C2 annealed at 600 °C/5 hours, solid line) and pdf file of $SmFe_2$ (solid points)

5.4. Magnetic properties

5.4.1. Temperature dependence of magnetisation

Temperature dependence of magnetisation of C2 annealed at 600 °C for 5 hours at temperature range 4 – 300 K with applied field parallel to the extrusion axis is plotted in figure 5.7. The curve exhibits a change in magnetisation at around 200 K, which corresponds to the known spin reorientation transition in this material.

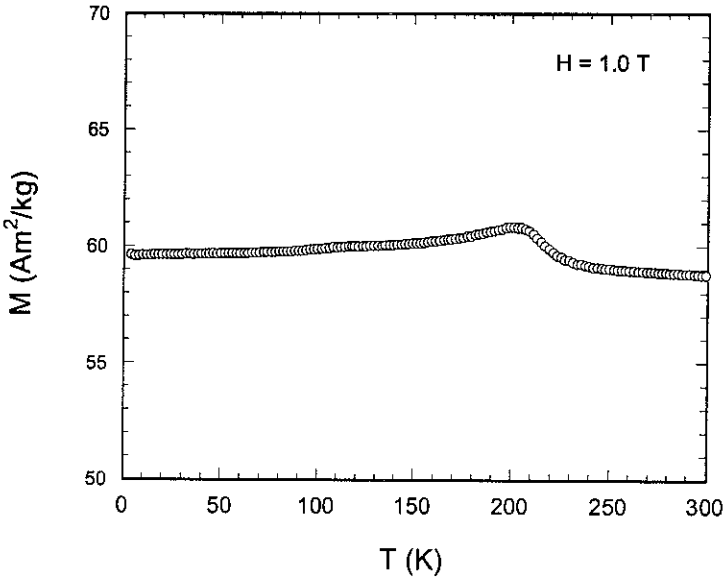

Figure 5.7: Temperature dependence of the magnetisation measured along the extrusion direction under the applied field 1 T. The abnormality at 200 K can be attributed to the known spin reorientation in this system.

5.4.2. Magnetisation vs. applied field

a vs. applied field $M(H)$ of the sample was measured along three orthogonal directions at 4 K and 300 K (figure 5.8: *a*-axis is the extrusion direction, *b*- and *c*-axis are transverse directions). Saturation magnetisation is 60 Am^2/kg at room temperature which is very close to the value of the single crystal $SmFe_2$ [16]. The sample is cubic in shape and thus has equal demagnetising coefficients along three measuring directions. Magnetisation is highest along the *c*-axis at low temperature but along the *a*-axis at room temperature. Knowing that the magnetic easy axis rotates from the <110> axis at low temperature to the <111> axis at room

temperature, the observed results suggest that the <111> axis of the $SmFe_2$ grains tend to align along the extrusion direction.

Measurements suggest that the sample is somewhat textured. At 4 K, the *c*-axis is the easy axis, whereas at 300 K, *a*-axis is the easy axis. From figure 5.8, the difference in $M(H)$ curves with H along three axes suggests that the <111> axes tend to align along the extrusion direction.

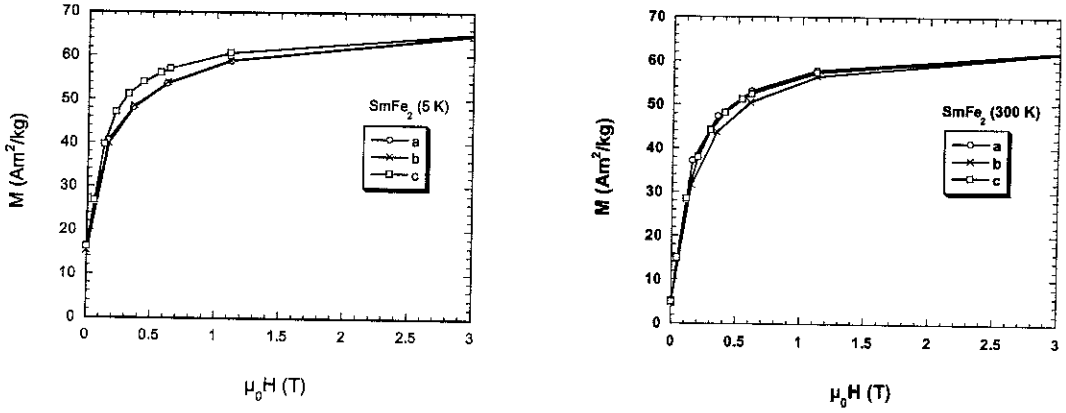

Figure 5.8: Magnetisation of the $SmFe_2$ produced by annealing C2 at 450 °C/5 hours at (a) 5 K and (b) 300 K.

5.4.3. Magnetostriction

Saturation magnetostriction λ_s along the *a*, *b*, *c*-axes of C2 compared with literature data for a polycrystalline sample is plotted in figure 5.9. At room temperature saturation magnetostriction measured along the *a*-axis λ_s (a) is –1280 ppm, significantly higher than that measured along the *b*-, and *c*-axes, which are –950 and –900 ppm, respectively. At 4 K, we still have $\lambda_s(a) > \lambda_s(b) > \lambda_s(c)$, with values of –1950, –1550, –1400 ppm. The significantly higher value of λ_s along the extrusion direction is a further evidence for partial <111> texture along this direction since magnetostriction should be greatest along this crystallographic axis. The value of magnetostriction of this sample is higher than that reported by Giguère and comparable to that of the single crystalline samples. However it is still less than the maximum value reported for a polycrystalline sample [8]. This may be tentatively attributed to the presence of secondary phases (Sm, Fe) in our samples.

The field required to saturate magnetisation is about 2 T at room temperature and increased to about 3 T at low temperature, which is due to the higher anisotropy field at low temperatures than at high temperatures.

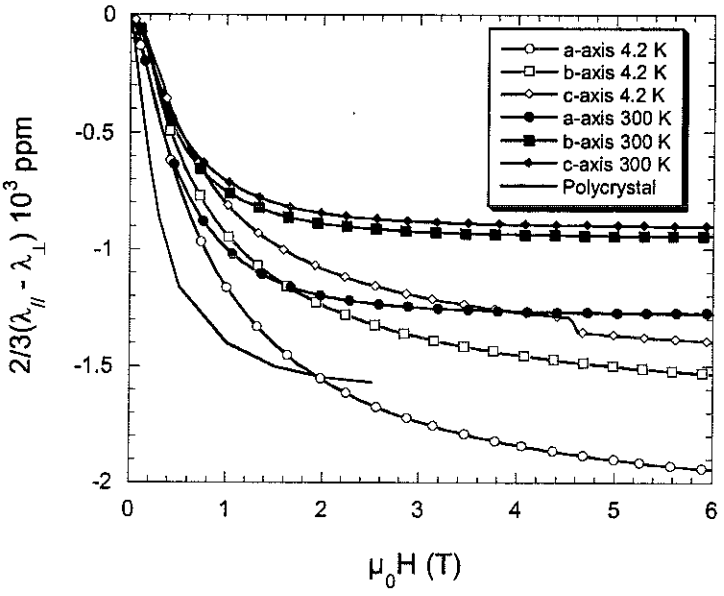

Figure 5.9: Saturation magnetostriction measured at 4 K and 300 K along three orthogonal directions a, *b*, *c* of Sm/Fe composite annealed (600 °C/5 hours) after 2 extrusion cycles. Literature values obtained for a polycrystalline sample are also shown [7].

5.5. Conclusions and perspectives

We produced Sm/Fe multilayers with layer thickness of some tens of microns by hydrostatic extrusion. Further extrusion was difficult because 1) Sm is rhombohedral and thus difficult to extrude and 2) $SmFe_2$ is formed along the layer interfaces during the stress relief heat treatment rendering the sample brittle (a chain is only as strong as its weakest link).

X-ray diffraction and SEM image of multilayer Sm/Fe after annealing (600 °C/5 hours) show that the diffusion to form $SmFe_2$ is practically complete.

Magnetisation and magnetostriction measurements indicate partial <111> texture along the extrusion direction. Saturation magnetostriction values along the extrusion direction reach – 1280 ppm.

The intermetallic phase $SmFe_2$ is very brittle and thus difficult to machine. This fact is the reason to motivate us to prepare $SmFe_2$ by co-extrusion of Sm and Fe foils followed by a diffusion controlled growth of the intermetallic phase by suitable annealing. The final sample shape may be attained by machining and/or forming the sample prior to annealing to form the intermetallic phase.

References

1. du Trémolet de Lacheisserie, E., *Magnetostriction, Theory and Applications of Magnetoelasticity*. (1993), Boca Raton: CRC Press.
2. Legvold, S., J. Alstad, and J. Rhyne, *Giant Magnetostriction in Dysprosium and Holmium Single Crystals*. Phys. Rev. Lett., **10** (1963) 509.
3. Clark, A.E., B.F. DeSavage, and R. Bozorth, *Anomalous Thermal Expansion and Magnetostriction of Single-Crystal Dysprosium*. Phys. Rev., **138** (1965) A216.
4. Callen, E. in *Proceedings of Metallic Magnetoacounstic Materials Workshop*. (1969) Boston, MA. 75.
5. Koon, N.C., A. Schindler, and F. Carter, Phys. Lett. A, **37** (1971) 413.
6. Clark, A.E. and H.S. Belson, *Giant Room-Temperature Magnetostrictions in $TbFe_2$ and $DyFe_2$*. Phys. Rev. B, **5** (1972) 3642.
7. Atzmony, U., M.P. Dariel, E.R. Bauminger, D. Lebenbaum, I. Nowik, and S. Ofer, *Magnetic Anisotropy and Spin Rotations in $Ho_xTb_{1-x}Fe_2$ Cubic Laves Compounds*. Phys. Rev. Lett., **28** (1972) 244.
8. Clark, A.E., *Magnetostrictive Rare-Earth - Fe_2 coumpounds*, in *Ferromagnetic Materials*, E.P. Wohlfarth, Editor **1**. (1980), North-Holland Publishing Company. p. 531.
9. Koon, N.C., C.M. Williams, and B.N. Das, *Giant magnetostriction materials*. J. Magn. Magn. Mater., **100** (1991) 173.
10. Szymczak, H., *From Almost Zero Magnetostriction to Giant Magnetostrictive Effects: Recent Results*. J. Magn. Magn. Mater., **200** (1999) 425.
11. Chen, C.W., *Magnetism and Metalurgy of Soft Magnetic Materials*. (1977), Amsterdam: Norht-Holland Publishing.
12. Clark, A.E. in *Proceedings of the International Conference on Magnetism (ICM-73)*. (1974) Moscow. 335.
13. Chikazumi, S., *Physics of Ferromagnetism*. (1997), Clarendon Press: Oxford. p. 343.
14. Kubaschewski, O., *Fe-Sm; Iron-Samarium*, in *Iron-binary phase diagrams*. (1982), Springer-Verlag. p. 104.
15. Cannon, J.F., D.L. Robertson, and H.T. Hall, *Synthesis of Lanthanide-Iron laves phases at high pressures and temperatures*. Mat. Res. Bull., **7** (1972) 5.
16. Samata, H., N. Fujiwara, Y. Nagata, T. Uchida, and M.D. Lan, *Crystal Growth and Magnetic Properties of $SmFe_2$*. Jpn. J. Appl. Phys., **37** (1998) 5544.
17. Atzmony, U., M.P. Dariel, E.R. Bauminger, D. Lebenbaum, I. Nowik, and S. Ofer, *Spin-Orientation Diagrams and Magnetic Anisotropy of Rare-Earth-Iron Ternary Cubic Laves Compounds*. Phys. Rev. B, **7** (1973) 4220.
18. Atzmony, U., M.P. Dariel, E.R. Bauminger, D. Lebenbaum, I. Nowik, and S. Ofer. *Spin Reorientation in $SmFe_2$*. in *Proceedings of the tenth Rare-Earth Conference*. (1973) Arizona. 605.

19. van Diepen, A.M., H.W. de Wijn, and K.H.J. Buschow, *Temperature Dependence of the Crystal-Field-Induced Anisotropy in $SmFe_2$.* Phys. Rev. B, **8** (1973) 1125.

20. Rosen, M., H. Klimker, U. Atzmony, and M.P. Dariel, *Magnetoelasticity in $SmFe_2$.* Phys. Rev. B, **9** (1974) 254.

21. Samata, H., N. Fujiwara, Y. Nagata, T. Uchida, and M.D. Lan, *Magnetic anisotropy and magnetostriction of $SmFe_2$ crystal.* Journal of Magnetism and Magnetic Materials, **195** (1999) 376.

22. Batt, A.J., R.A. Buckley, and H.A. Davies, *Giant magnetostriction behaviour of melt-spun ribbon and pressed compacts of $Sm(Fe_{1-x}Co_x)$ alloys.* Sensors and Actuators, **81** (2000) 170.

23. Giguère, A., *Préparation et étude des propriétés magnétiques et de transport de nanomatériaux obtenus par extrusion hydrostatique et laminage*, Thesis in *Physics* (2002), Université Joseph Fourier - Grenoble 1: Grenoble.

24. Giguère, A., N.H. Hai, N. Dempsey, and D. Givord, *Preparation of microstructured and nanostructured magnetic materials by mechanical deformation.* J. Magn. Magn. Mater., **242-245** (2001) 581.

25. Wacquant, F., *Elaboration et étude des propriétés de réseaux de fils magnétiques submicroniques, obtenus par multi-extrusions*, Thesis in *Physics* (2000), Université Joseph Fourier - Grenoble 1: Grenoble.

26. Wacquant, F., S. Denolly, A. Giguère, J.P. Nozières, D. Givord, and V. Mazauric, *Magnetic properties of nanometric Fe wires obtained by multiple extrusions.* IEEE Trans. Magn., **35** (1999) 3484.

Conclusions en Français

Nous nous sommes consacrés dans ce travail à la préparation de nanomatériaux magnétiques par déformation mécanique à froid.

Suivant la voie développée à l'origine au Laboratoire Louis Néel, nous avons d'abord utilisé la déformation par extrusion hydrostatique pour produire le système magnétostrictif $SmFe_2$. L'application d'un traitement thermique à basses températures (600 °C) nous a permis d'obtenir la phase $SmFe_2$. L'obtention d'une texture significative dans le matériau final constitue un résultat important. Une magnétostriction à saturation de –1280 ppm a été atteinte à température ambiante. Cette valeur est supérieure à celle obtenue dans les travaux antérieurs, décrits dans le manuscrit de thèse de A. Giguère; elle approche la valeur caractéristique des matériaux massifs polycristallins.

Le développement d'une nouvelle méthode de déformation, utilisant le laminage sous gaine, a constitué une contribution originale. Dans cette approche, une série de cycles de déformation est appliquée à un empilement alterné de feuilles métalliques, mais aucun traitement intermédiaire de recuit n'est appliqué. Les dimensions du matériau macro-composite initial sont réduites jusqu'aux échelles micrométrique ou nanométrique. Un traitement thermique final est appliqué pour former la phase désirée.

Nous avons réussi à préparer des nanocomposites Fe/Pt par laminage sous gaine, tels que les épaisseurs des couches constitutives individuelles soient de l'ordre de quelques nanomètres. Ces nanocomposites ont été recuits à 400 °C – 500 °C afin de former les phases désirées, en particulier les composés intermétalliques FePt, Fe_3Pt et $FePt_3$. Quatre compositions ont été choisies: FePt, FePt/Ag, FePt/Fe_3Pt and FePt/$FePt_3$. Des champs coercitifs de 0,7-0,8 T ont été obtenus dans les systèmes monophasés FePt. L'ajout d'argent nous a permis d'augmenter la coercitivité jusqu'à 0,9 T pour 7% d'Ag en volume et 1,1 T pour 35 % d'Ag. Nous pensons

que le rôle de l'argent est de limiter la croissance des grains. L'introduction d'argent permet aussi d'améliorer les propriétés mécaniques des macrocomposites, et ainsi de reculer les limites ultimes des déformations appliquées. Nous n'avons pas réussi à obtenir des comportements de type exchange-spring dans le système $FePt/Fe_3Pt$ ni de décalage d'échange (exchange-bias) dans $FePt/FePt_3$. Nous avons attribué ces insuccès au fait que la taille des grains constitutifs reste trop importante.

Nous avons analysé la coercitivité des systèmes monophasés FePt dans le cadre des modèles micromagnétique et global. Ces analyses requièrent la connaissance préalable des constantes d'anisotropie magnétocristalline. La valeur de la constante du second ordre $K_1(T)$ dans FePt a été extraite de l'analyse des mesures d'aimantation dans tout le domaine de température concerné. Le paramètre phénoménologique N_{eff}, qui représente les interactions agissant sur le noyau critique a été trouvé négatif, ce qui est inhabituel dans les matériaux magnétiques durs. Ce résultat pourrait signifier que la microstructure du système FePt est telle que les interactions dipolaires n'ont pas le signe habituel. Il pourrait aussi indiquer la présence d'interactions d'échange résiduelles entre les grains, superposées aux interactions dipolaires. Pour le système monophasé FePt, les différences entre les courbes d' aimantation obtenues en champ magnétique appliqué dans le plan de laminage (IP) et perpendiculairement au plan de laminage (PP) ont été interprétées en considérant l'existence d'une anisotropie dans le processus d'aimantation. De plus, les courbes d'aimantation IP et PP des nanocomposites $FePt/Fe_3Pt$ ont été discutées dans le cadre du concept dit de « dipolar-spring ».

Le couplage à travers une interface dans les nanocomposites magnétiques constitués de deux phases magnétiques différentes, a été analysé. Les propriétés magnétiques intrinsèques de tels systèmes ont été évaluées dans une approche de type champ moyen, en utilisant une méthode auto-consistante. Les propriétés magnétiques prédites pour de tels matériaux diffèrent de celles de matériaux non couplés, sur quelques plans atomiques. Le modèle a été étendu aux systèmes dans lesquels des couches à base de composés terres rares – métal de transition sont couplés à des couches de fer ou cobalt.

Conclusions in English

This work has concentrated on the study of the magnetic properties of nanomaterials prepared by cold mechanical deformation.

Following the route developed earlier in the Laboratoire Louis Néel, hydrostatic deformation was used initially to produce magnetostrictive $SmFe_2$. By applying a low-temperature heat treatment (600 °C), we were able to produce the $SmFe_2$ phase. An important feature was the obtention of significant texture in the final alloy. A room temperature saturation magnetostriction of –1280 ppm was reached. This value is higher than that obtained earlier in the framework of the thesis of A. Giguère. It approaches the value obtained in polycrystalline $SmFe_2$.

An original contribution was to develop a new deformation route, based on *sheath-rolling*, allowing successive deformations to be applied without any intermediate stress-relief heat treatment. In this procedure, an alternate stacking of metallic foils is formed. The macrocomposite obtained is inserted into a sheath and cyclically deformed in order to reduce the foil dimensions down to the micrometer or nanometre scale. A final heat treatment is applied to form the desired intermetallic phases.

Using sheath-rolling, we have successfully obtained Fe/Pt nanocomposites with individual thickness of the order of some nanometres. These Fe/Pt nanocomposites were annealed at 400 °C – 500 °C in order to form the desired phases, in particular the intermetallic compounds FePt, Fe_3Pt and $FePt_3$. Four compositions were chosen, allowing the following association of phases to be obtained: FePt, FePt/Ag, FePt/Fe_3Pt and FePt/$FePt_3$. Room temperature coercive fields of around 0.7 – 0.8 T were obtained in the single-phase FePt samples. Adding Ag increased the coercive field value to around 0.9 T for 7 vol % Ag and 1.1 T for 35 vol % Ag. The Ag improved the mechanical properties of the macrocomposites, alloying them to be

deformed more than the Ag-free samples. It is expected that the presence of Ag served to limit grain growth in the FePt phase. We were not successful in preparing exchange-spring FePt/Fe_3Pt and exchange-bias FePt/$FePt_3$ materials and this was attributed to the fact that the individual dimensions of the grains were not small enough.

Coercivity in the single-phase FePt samples was analysed within the framework of the micromagnetic and global models. . This analysis required knowledge of the second order anisotropy constant, K_1, of FePt. K_1 values were extracted from an analysis of the M(H) curves in the full temperature range studied. The phenomenological parameter N_{eff}, which represents interactions acting on the critical nucleus, was found to be negative, which is not the usual case for hard magnetic materials. This may suggest that dipolar interactions do not have the usual sign in these specific microstructures. Alternatively, residual exchange interactions may be superimposed on dipolar interactions. The differences between the magnetisation curves, whether the applied field is parallel (IP) or perpendicular (PP) to the rolling plane of the single phase FePt, were explained by considering anisotropy in the magnetisation reversal process.. The IP and PP magnetisation curves of FePt/Fe_3Pt nanocomposites were interpreted within the "dipolar spring" concept.

The coupling across interfaces in a magnetic nanocomposite consisting of two different magnetic phases was analysed. The intrinsic magnetic properties of such a system were calculated within a mean field approach using a self-consistent method. The intrinsic magnetic properties were found to be significantly affected over a few interatomic distances. The model developed was extended to systems in which rare earth – transition compounds are coupled to Fe or Co.

Annexe A: Experimental details

Heat treatment

All samples after final extrusion/rolling cycle were sealed in a quartz tube with inner and outer diameter of 4 – 6 mm under vacuum 10^{-5} mbar, and annealed in a muffle at temperature in the range 300 °C – 700 °C for time 2 minutes – 48 hours and quenched into water.

X-ray diffraction

X-ray diffraction measurements were made with Cu $K\alpha$ radiation, $\lambda_{K\alpha}$ = 1.54056 Å by Philips PW 1729. For $SmFe_2$ sample, XRD measurements were conducted on the $SmFe_2$ powder produced by crushing annealed multilayers. For all Fe-Pt samples, the X-ray beam is reflected from planes parallel to the rolling plane (figure A.1).

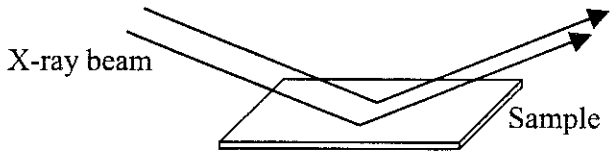

Figure A. 1: Schematic illustration of the XRD measurement.

SEM and TEM

The SEM images were taken with a LEO 1530 electron microscope equipped with a field emission gun and operated at 20 kV. The TEM images were taken with a 3010 FX Jeol electron microscope operated at 300 kV.

Magnetic measurements

Magnetic measurements were performed on either a vibration sample magnetometer (VSM) or an extraction magnetometer. By the VSM, the applied field can reach maximum of 8 T in the temperature range 4 K – 300 K. By the extraction magnetometer, the maximal applied field is 10 T at low temperatures (4 K – 300 K) and 7 T at high temperatures (300 K – 700 K). For the hard FePt specimens, the values of coercive field are usually about 10 % higher when measured by the VSM than those measured by the extraction magnetometer. This may be ascribed to either higher sweep rate in former or incorrect calibration. Magnetisation measurements that we reported in this thesis were conducted by the extraction magnetometer.

Annexe B: Quantification of order using X-ray diffraction

Chapter 2 describes the crystalline structure of the Fe-Pt alloys. Existence of the superstructure and the long-range degree of order S (expression 2.1) can be revealed from the X-ray diffraction (XRD) patterns. Reflections, which are independent of the degree of order, are called fundamental reflections, while reflections, which vanish as the order vanishes, are called superstructure or superlattice reflections. Table B.1 gives values of the indices h, k, l of atomic planes corresponding to the fundamental and superstructure lines, for the $L1_0$ and $L1_2$ crystal structure [1]. Table B.2 gives the values of the powder diffraction (PDF) intensities of the Fe_3Pt, FePt and $FePt_3$. The PDF intensities of the FePt, $FePt_3$ were taken from the PDF file 43-1359, 29-0716, respectively. The PDF intensities of the Fe_3Pt were calculated from lattice parameters of the structure with $a = 3.74$ Å [2].

Table B.1: Values of the indices h, k, l of atomic planes corresponding to the fundamental and superlattice lines, for the $L1_0$ and $L1_2$ crystal structures.

Structure type	Fundamental lines	Superlattice lines
$L1_0$ lattice	The numbers h, k, l are either all even or all odd	Numbers h and k are even, and l is odd; or h and k are odd and l is even
$L1_2$ lattice	The numbers h, k, l are either all even or all odd	Numbers h, k, l are not all even nor all odd

Table B.2: Power diffraction intensities (PDF) (Cu $K\alpha$ radiation) of the Fe_3Pt, FePt and $FePt_3$. The underlined index represents for the superstructure reflections.

Fe_3Pt

2θ	Intensity	hkl
23.847	–	100
34.018	–	110
41.986	–	111
48.872	–	200
55.098	–	210
60.882	–	211
71.612	–	220
76.71	–	221
76.71	–	300
81.702	–	310
86.632	–	311
91.536	–	222
96.452	–	320

FePt

2θ	Intensity	hkl
23.966	30	001
32.839	28	110
41.049	100	111
47.123	33	200
49.041	17	002
53.546	19	201
60.283	14	112
68.881	11	220
70.357	25	202
73.995	10	221
78.457	9	130
83.393	40	311
86.232	20	113
88.997	19	222
95.212	9	203
98.211	21	312

$FePt_3$

2θ	Intensity	hkl
	–	100
40.605	60	111
46.942	100	200
53.077	20	210
58.681	10	211
68.766	70	220
82.781	100	311
87.491	50	222
92.09	10	320
96.683	20	321

Table B.3: Parameters used to estimate the long-range order parameter S of the FePt alloy according to expressions (B.1) – (B.3) [3].

Peak	2θ	LP	M_{Fe}	f_{Fe}	Δ_{Fe}	M_{Pt}	f_{Pt}	Δ_{Pt}
$(001)_s$	23.966	2.26	0.005	21.01	3.4	0.005	64.43	8
$(002)_f$	49.041	0.94	0.019	16.93	3.3	0.018	55.12	7

The order parameter S, determined by arrangement of atoms over the entire crystal, in the FePt sample can be deduced by comparing the relative integrated intensities of the superstructure peak – A_s (001) and the fundamental peak – A_f (002). The integrated intensity can be described in terms of a constant K, multiplicity m, Lorentz-polarization factor (LP), and structure factor F and its complex conjugate F^* [3]:

$$A = Km(\mathrm{LP})FF^*; \qquad \text{(Equation B. 1)}$$

If the sample is textured the integrated intensity must be corrected by the Full Width at Half Maximum of the rocking curve FWHM:

$$A = (\mathrm{FWHM})Km(\mathrm{LP})FF^*;$$

In our case, the sample is nearly isotropic, so that we consider the FWHM of the (001) and (002) peaks to be identical.

For superstructure peaks:

$$(FF^*)_s = 4S^2[(f_{Pt}e^{-M_{Pt}} - f_{Fe}e^{-M_{Fe}})^2 + (\Delta_{Pt}e^{-M_{Pt}} - \Delta_{Fe}e^{-M_{Fe}})^2]; \qquad \text{(Equation B. 2)}$$

For fundamental peaks:

$$(FF^*)_f = 16[(x_{Fe}f_{Fe}e^{-M_{Fe}} + x_{Pt}f_{Pt}e^{-M_{Pt}})^2 + (x_{Fe}\Delta_{Fe}e^{-M_{Pt}} + x_{Pt}\Delta_{Pt}e^{-M_{Fe}})^2]; \qquad \text{(Equation B. 3)}$$

e^{-M} is the Debye-Waller correction, and f and Δ are the real and imaginary parts of the atomic scattering factor, respectively (values of (001) and (002) peaks of the FePt alloy are given in table B.3).

Qualification of order for the FePt foil produced by annealing the Fe/Pt multilayer at 450 °C for 15 minutes:

The XRD measurements of all samples in this thesis were conducted with the Cu $K\alpha$ radiation, λ = 1.54056 Å. Here we present an example of quantification of order of the FePt foil. Figure B.1 shows the XRD patterns of (a) superlattice (001) and (b) fundamental (002) peaks of the FePt sample after annealing at 450 °C/ 15 minutes. The data were fitted to the Gaussian function from which integration intensities can be obtained. The integration

intensities of the (001) and (002) peaks are A_s = 1661 and A_f = 2084 in this case. Comparing A_s and A_f one has:

$$\frac{A_s}{A_f} = \frac{Km(LP)(FF^*)\big|_{(001)}}{Km(LP)(FF^*)\big|_{(002)}}$$

where known parameters in the right hand side are given in table B.3. From this, the order parameter S = 0.94 is deduced. Similarly, S obtained for the FePt samples after annealing at 450°C for 5 minutes and 48 hours are 0.86 and 0.98, respectively.

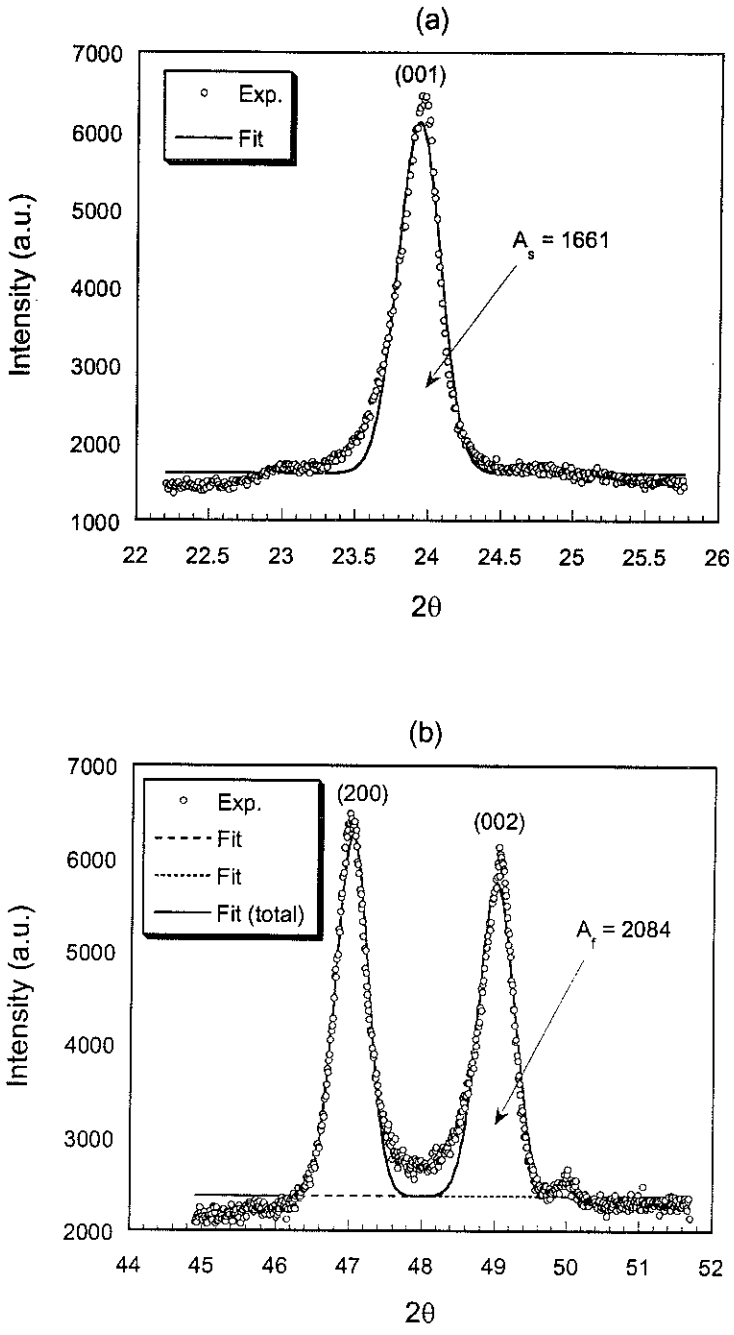

Figure B.1: (a) The superlattice (001) and (b) the fundamental (002) peaks of the FePt foil, produced by annealing the Fe/Pt multilayer at 450 °C for 15 minutes (circles). The lines represent for the fitted values to the Gaussian function from which the integration intensities (A_s and A_f) can be deduced.

Reference

1. Krivoglaz, M.A. and A. Smirnov, *The theory of order-disorder in alloys*. (1964), London: Macdonald.

2. Landolt, H.H., *Landolt-Boernstein, New Series*. Vol. 19a. (1986), Berlin: Springer-Verlag.

3. Warren, B.E., *X-ray diffraction*. 1 ed. (1969), Massachusetts: Addison-Wesley Publishing Company.

Annexe C: Modelling the exchange coupling in the nanocomposite systems

Chapter 2 modelled a nanocomposite system with exchange interactions across interfaces by self-consistent method using MATLAB 5.3.

Magnetisation calculation

Diagram of the program is schematised in figure C.1. We assume that the system consists of two different materials with different intrinsic properties (Curie temperature T_c, exchange constant n, number of nearest neighbour z). The schematic diagram of the model nanocomposite is presented in figure 3.1.

Initially, the reduced magnetisation $m = M(T)/M(0)$ was arbitrarily chosen to be 1, *i.e.* all moments were assumed to be equal and saturated. When we have values of magnetisation, combining with parameters representing for intrinsic properties of each phase at a certain temperature, the molecular field B_i can be deduced by expressions (3.3). From these values of magnetisation can be recalculated by using expression (3.4). The procedure was repeated until the difference of the reduced magnetisation of two consecutive calculations is less than 10^{-8}, then we obtain final m. The temperature dependence of magnetisation is shown in figure 3.3. The second and fourth anisotropy constant, at a given temperature can be calculated from expression (3.9) and their temperature dependence are plotted in figure 3.5.

Figure C.1: Diagram of the modelling program used in chapter 3.

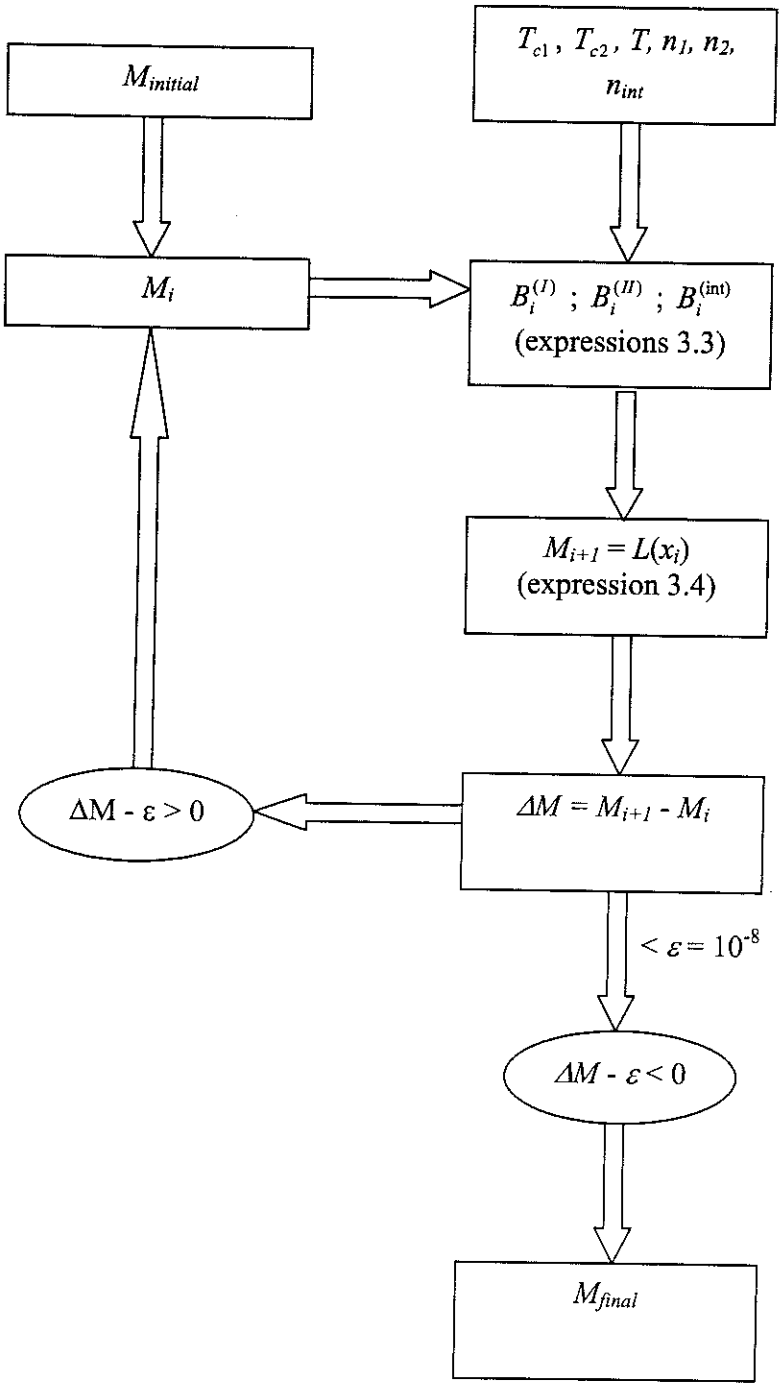

Résumé

Dans le cadre de ce travail de thèse, on a préparé des nanomatériaux par déformation mécanique à froid et étudié leurs propriétés magnétiques. La méthode d'élaboration principale utilisée met en jeu la déformation à froid de plaques de métaux miscibles d'épaisseur sub-millimétrique jusqu'à l'échelle du nanomètre puis l'application de traitements thermiques de diffusion/réaction entre les éléments constitutifs. En particulier, la technique originale de «sheath-rolling» sans recuit intermédiaire d'adoucissement a été développée puis appliquée à la préparation de matériaux nanostructurés.

Deux séries d'échantillons ont été étudiées: Sm/Fe et Fe/Pt. Les multicouches de Sm/Fe ont été préparées par la technique d'extrusion hydrostatique, jusqu'à l'échelle micrométrique. La phase $SmFe_2$ magnétostrictive a été obtenue par traitement thermique final à 600 °C. Une magnétostriction à saturation de -1280 ppm a été mesurée. Des multicouches texturées de Fe/Pt, dont l'épaisseur par couche est de l'ordre de 10 nm, ont été préparées par la technique de «sheath-rolling». Les phases intermétalliques recherchées ont été formées par recuit de diffusion/réaction à 400°C-500°C. Des champs coercitifs $\mu_0 H_c$ de 0.7 T - 0.8 T à température ambiante ont été obtenus dans les échantillons monophasés de type FePt $L1_0$. L'ajout d'Ag a permis d'accroître ces valeurs jusqu'à 0.9 T pour 7 % Ag en vol. et 1.1 T pour 35 % Ag en vol.. L'analyse des mécanismes de coercitivité a révélé que les valeurs élevées des champs coercitifs résultent en partie d'une contribution des interactions dipolaires. Les différences entre les courbes d'aimantation dans le plan et hors-plan pour FePt et $FePt/Fe_3Pt$ ont été expliquées en considérant le caractère anisotrope des mécanismes de coercitivité et des interactions dipolaires. Le nouveau concept dit de «dipolar-spring» a été présenté. En outre, les propriétés magnétiques intrinsèques de systèmes modèles nanocomposites ont été calculées dans une approche de type champ moyen.

Mot clés:

Déformation mécanique
Laminage sous gaine
Extrusion
Matériaux nanostructurés massifs
Aimants permanents
Multicouches massives
FePt
$SmFe_2$

Abstract

In the framework of this thesis, nanomagnetic materials have been prepared by mechanical deformation and their magnetic properties have been studied. The main method of sample preparation used involves the mechanical deformation of sub-millimetre foils of miscible metals down to the nanometre scale, followed by the application of a final diffusion/reaction heat treatment to form the desired phases. In particular, the original "sheath-rolling" technique, without intermediate stress-relief heat treatment, has been developed and applied to the preparation of nanostructured materials.

Two series of samples have been studied: Sm/Fe and Fe/Pt. Sm/Fe multilayers were prepared by the hydrostatic extrusion technique down to the micrometer scale. The formation of the $SmFe_2$ phase followed heat treatment at 600 °C. A saturation magnetostriction of 1280 ppm was reached. Textured Fe/Pt multilayers with layer individual thickness of the order of 10 nm were prepared by the sheath-rolling technique. The formation of the desired intermetallic phases was obtained through diffusion/reaction annealing at 400°C-500 °C. Room temperature coercive field values, $\mu_0 H_c$ = 0.7 T - 0.8 T were obtained in the single-phase $L1_0$ FePt samples. Ag addition allowed the coercive field values to be increased up to 0.9 T for 7 vol % Ag and 1.1 T for 35 vol % Ag. The analysis of coercivity mechanisms revealed that the high coercive field values obtained may be related in part to a contribution of the dipolar interactions. The differences between the in-plane and perpendicular-to-plane magnetisation curves of the FePt and $FePt/Fe_3Pt$ systems were explained by considering the anisotropic character of the coercivity mechanisms and of the dipolar interactions. The new "dipolar-spring" concept has been introduced. Beside this, the intrinsic magnetic properties of model magnetic nanocomposite systems have been calculated within a mean field approach.

Keywords

Mechanical Deformation
Sheath-rolling
Extrusion
Bulk nanostructured materials
Permanent magnets
Bulk multilayers
FePt
$SmFe_2$

Tóm tắt

Luận án này trình bày việc chế tạo vật liệu từ nano bằng phương pháp biến dạng cơ học và nghiên cứu tính chất từ của vật liệu thu được. Trong phương pháp biến dạng cơ học, mẫu ban đầu gồm các tấm kim loại (ít nhất gồm hai kim loại có tính chất có thể hoà tan với nhau) có độ dày cỡ vài trăm micro mét được xếp chồng lên nhau và được biến dạng xuống đến kích thước cỡ nano mét. Mẫu khối tạo thành là các màng đa lớp có độ dày vài chục nano mét. Sau đó mẫu được xử lí nhiệt để khuyếch tán xảy ra và tạo pha mong muốn. Trong luận án này, lần đầu tiên chúng tôi đưa ra kĩ thuật "cán nguội trong vỏ thép" mà không dùng các biện pháp xử lí nhiệt trung gian và ứng dụng kĩ thuật này để chế tạo vật liệu từ có cấu trúc nano.

Luận án đề cập đến hai họ mẫu: Sm/Fe và Fe/Pt. Mẫu Sm/Fe được chế tạo bằng kĩ thuật đùn thuỷ tĩnh từ kích thước mini mét xuống kích thước micro mét. Sau đó, mẫu được ủ nhiệt tại nhiệt độ 600°C để tạo pha liên kim loại $SmFe_2$. Mẫu $SmFe_2$ có từ giảo bão hoà khá lớn, cỡ - 1280 ppm. Mẫu Fe/Pt được chế tạo bằng kĩ thuật "cán nguội trong vỏ thép" đến kích thước khoảng 10 nm. Cấu trúc của mẫu có phương ưu tiên rất rõ nét. Khuyếch tán và tạo pha liên kim loại FePt cấu trúc $L1_0$ xảy ra khi ủ nhiệt tại 400°C – 500°C. Pha FePt có lực kháng từ $\mu_0 H_c$ = 0.7 T - 0.8 T tại nhiệt độ phòng, đây là giá trị cao nhất của lực kháng từ của FePt ở dạng khối. Giá trị này được nâng lên khi có thêm Ag (0.9 T khi thể tích của Ag là 7% và 1.1 T khi thể tích của Ag là 3.5%). Phân tích cơ chế của lực kháng từ cho thấy giá trị cao của lực kháng từ của các mẫu FePt có thể liên quan đến tương tác lưỡng cực. Lần đầu tiên luận án đưa ra khái niệm "đàn hồi lưỡng cực" mô tả đặc điểm dị hướng của lực kháng từ và của tương tác lưỡng cực để giải thích sự khác nhau giữa đường cong từ trễ khi từ trường ngoài song song và vuông góc với mặt phẳng mẫu của mẫu FePt và mẫu $FePt/Fe_3Pt$, khái niệm này có thể được mở rộng để giải thích các hệ dị hướng khác. Luận án cũng trình bày các tính toán tính chất từ bằng phương pháp trường trung bình cho mô hình hệ nanocomposite.

Từ khoá

Biến dạng cơ học
Kĩ thuật cán nguội
Kĩ thuật đùn
Vật liệu từ cấu trúc nano dạng khối
Nam châm vĩnh cửu
Màng đa lớp dạng khối
FePt
$SmFe_2$